Estimating Arctic sea ice melt pond fraction and assessing ice type separability during advanced melt

by

Sasha Nasonova
BSc. University of Victoria, 2015

A Thesis Submitted in Partial Fulfillment
of the Requirements for the Degree of

MASTER OF SCIENCE

in the Department of Geography

Supervisory Committee

Estimating Arctic sea ice melt pond fraction and assessing ice type separability during advanced melt

by

Sasha Nasonova
BSc. University of Victoria, 2015

Supervisory Committee

Dr. Randy Scharien, Supervisor
(Department of Geography)

Dr. Dennis Jelinski, Department Member
(Department of Geography)

Abstract

Arctic sea ice is rapidly declining in extent, thickness, volume and age, with the majority of the decline in extent observed at the end of the melt season. *Advanced melt* is a thermodynamic regime and is characterized by the formation of melt ponds on the sea ice surface, which have a lower surface albedo (0.2-0.4) than the surrounding ice (0.5-0.7) allowing more shortwave radiation to enter the system. The loss of multiyear ice (MYI) may have a profound impact on the energy balance of the system because melt ponds on first-year ice (FYI) comprise up to 70% of the ice surface during *advanced melt*, compared to 40% on MYI. Despite the importance of *advanced melt* to the ocean-sea ice-atmosphere system, *advanced melt* and the extent to which winter conditions influence it remain poorly understood due to the highly dynamic nature of melt pond formation and evolution, and a lack of reliable observations during this time. In order to establish quantitative links between winter and subsequent *advanced melt* conditions, and assess the effects of scale and choice of aggregation features on the relationships, three data aggregation approaches at varied spatial scales were used to compare high resolution satellite GeoEye-1 optical images of melt pond covered sea ice to winter airborne laser scanner surface roughness and electromagnetic induction sea ice thickness measurements. The findings indicate that winter sea ice thickness has a strong association with melt pond fraction (f_p) for FYI and MYI. FYI winter surface roughness is correlated with f_p, whereas for MYI no association with f_p was found. Satellite-borne synthetic aperture radar (SAR) data are heavily relied upon for sea ice observation; however, during *advanced melt* the reliability of observations is reduced. In preparation for the upcoming launch of the RADARSAT Constellation Mission (RCM), the Kolmogorov-Smirnov (KS) statistical test was used to assess the ability of simulated RCM parameters and grey level co-occurrence matrix (GLCM) derived texture features to discriminate between major ice types during winter and *advanced melt*, with a focus on *advanced melt*. RCM parameters with highest discrimination ability in conjunction with optimal GLCM texture features were used as input parameters for Support Vector Machine (SVM) supervised classifications. The results indicate that steep incidence angle RCM parameters show promise for distinguishing between FYI and MYI during *advanced melt* with an overall classification accuracy of 77.06%. The addition of GLCM texture parameters improved accuracy to 85.91%. This thesis provides valuable contributions to the growing body of literature on f_p parameterization and SAR ice type discrimination during *advanced melt*.

Table of Contents

Supervisory Committee ii

Abstract iii

Table of Contents iv

List of Tables vi

List of Figures viii

List of Acronyms and Symbols xiii

Acknowledgments xv

Chapter 1 Introduction 1

1.1 Research Context 1

1.2 Research Objectives 4

1.3 Thesis Structure 4

1.4 References 5

Chapter 2 Linking Regional Winter Sea Ice Thickness and Surface Roughness to Spring Melt Pond Fraction on Landfast Arctic Sea Ice 9

2.1 Abstract 9

2.2 Introduction 10

2.3 Materials and Methods 13

2.3.1 Study Area 13

2.3.2 Data and Preprocessing 16

2.3.3 Object Based, Hybrid and Grid-Cell Image Analysis 18

2.4 Results 21

2.4.1 Victoria Strait Thickness, Roughness and f_p Distributions in 2015 21

2.4.2 Relationship between Thickness and f_p 22

2.4.3 Relationship between Roughness and f_p 25

2.4.4 Relationship between Smoothed Surface Roughness and f_p 28

2.4.5 Relationship between Thickness and Roughness 31

2.5 Discussion 32

2.6 Conclusions 35
2.7 Acknowledgments 37
2.8 Author Contributions 37
2.9 References 37

Chapter 3 Optimal compact polarimetric parameters and texture features for discriminating major sea ice types during winter and advanced melt 42

3.1 Introduction 43
3.2 Study Area and Data 46
3.3 Methods 48
    3.3.1 RCM Parameter Simulation 48
    3.3.2 Ice Type Separability and Classification 49
3.4 Results and Discussion 52
    3.4.1 Ice Type Separability 52
        3.4.1.1 Winter 52
        3.4.1.2 Advanced Melt 56
    3.4.2 Ice Type Classification 59
        3.4.2.1 Winter 59
        3.4.2.2 Advanced Melt 66
3.5 Conclusions 74
3.6 Acknowledgements 75
3.7 Appendix 77
3.8 References 78

Chapter 4 Summary and Conclusions 82

4.1 Summary of Key Findings 82
4.2 Opportunities for Future Work 84
4.3 Author Contributions 86
4.4 References 86

List of Tables

Table 2.1 Description of the datasets. 15

Table 2.2 Spearman correlation coefficients (r_s) between metrics of winter sea ice thickness and spring f_p for FYI and MYI at fine, medium (med) and coarse spatial scales (object and hybrid) as well as 120 and 240 m grid-cells. Bolded values are statistically significant ($p < 0.05$). 24

Table 2.3 Spearman correlation coefficients (r_s) between metrics of winter sea ice roughness and spring f_p for FYI and MYI at fine, medium (med) and coarse spatial scales (object and hybrid) as well as 120 and 240 m grid-cells. Bolded values are statistically significant ($p < 0.05$). 27

Table 2.4 Spearman correlation coefficients (r_s) between metrics of smoothed winter sea ice roughness and f_p for FYI and MYI at fine, medium (med) and coarse spatial scales. The data were aggregated using the hybrid object aggregation approach. Bolded values are statistically significant ($p < 0.05$). 30

Table 2.5 Spearman correlation coefficients (r_s) between metrics of winter sea ice roughness and thickness for FYI and MYI at fine, medium (med) and coarse spatial scales (object) as well as 120 and 240 m grid-cells. Bolded values are statistically significant ($p < 0.05$). 31

Table 3.1 Quad-polarimetric RADARSAT-2 scenes used in this study. 48

Table 3.2 Descriptions of GLCM texture features. 50

Table 3.3 Training and validation data used for supervised SVM classifications of *winter* and *advanced melt* RCM scenes. The total number of pixels, and the number of polygons in brackets, is shown. There was no DFYI in Winter S2 and Advanced Melt S1. 52

Table 3.4 Winter S1 and Winter S2 KS distances (0 to 1) for major ice type combinations. Bolded values correspond with statistically significant separability ($p<0.01$). Cell shading visually emphasizes discrimination ability of each RCM parameter, with high separability corresponding to light shading and low separability to dark shading. The top three most separable CP parameters which were used in the subsequent GLCM calculation are denoted with an asterisk (*). 54

Table 3.5 Winter S1 and Winter S2 average (and standard deviation) KS distances representing separability between sea ice types using RCM and GLCM texture features. RCM refers to the average separability of the top three CP parameters. Each GLCM value is the average separability of the feature, calculated for the top three parameters. All values are statistically significant ($p<0.01$). 56

Table 3.6 Advanced Melt S1 and Advanced Melt S2 KS distances (0 to 1) for major ice types. Bolded values are statistically significant (p<0.01). Cell shading visually emphasizes separability, with high separability values corresponding to light shading and low separability to dark shading. The top three most separable CP parameters which were used in the subsequent GLCM calculation are denoted with an asterisk (*). 57

Table 3.7 Advanced Melt S1 and Advanced Melt S2 average (and standard deviation) KS distances representing separability between sea ice types using CP and GLCM texture features. RCM refers to the average separability of the top three CP parameters. Each GLCM value is the average separability of the feature, calculated for the top three parameters. All values are statistically significant (p<0.01). 59

Table 3.8 Winter classification accuracies by ice type, average overall accuracies and Kappa coefficients. Each scene was classified using CP parameters alone and using CP parameters with corresponding GLCM Mean and GLCM Variance texture features as input variables. 60

Table 3.9 Classification accuracies by ice type, average overall accuracies and Kappa coefficients. Each scene was classified using CP parameters alone and using CP parameters with corresponding GLCM Mean and GLCM Variance texture features as input variables. 66

Appendix 4.1 Simulated RCM compact polarimetric parameters, associated equations and units (Adapted from Geldsetzer et al, 2015)…………………………………………………………...77

List of Figures

Figure 2.1 Schematic of our melt pond formation hypothesis derived primarily from *in situ* studies of sea ice evolution. Top panel shows a cross-section of pre-melt conditions of thin/smooth (left) and thick/rough (right) sea ice prior to melt. Bottom panel shows a cross-section during spring conditions. Left panel shows smooth/level ice dominated by extensive melt ponds. Right panel shows lower melt pond coverage due to high surface topography. Blue and grey bar in the center illustrates a bird's-eye view of melt pond extent. 13

Figure 2.2 Map of study area located in the CAA depicting the locations of RADARSAT-2 (RS-2) image acquisitions shown in purple and gray for FYI-dominated (FYID) and MYI-dominated (MYID) areas respectively. Corresponding GeoEye-1 optical image coverages for FYID are shown in green and MYID zone are shown in red. The track of airborne winter snow plus sea ice thickness and surface roughness point measurements is shown in black. The location of *in situ* snow depth measurements is shown by a red star in the outset map. 14

Figure 2.3 FYID (left) and MYID (right) ice zones. The first image in each panel is a winter RS-2 SAR image of the overlain by winter snow plus sea ice thickness measurements. The second image depicts the co-located spring GeoEye-1 optical scene of melt pond covered sea ice overlain by surface roughness measurements. Bottom panels show zoomed in data within the extents of the red polygons directly above each panel. 16

Figure 2.4 Methods flow chart of RS-2 and GeoEye-1 image processing, segmentation, data aggregation, and correlation and regression analyses. The calibrated, speckle filtered and georeferenced RS-2 SAR image was segmented into image objects, with the objects used for further OBIA data aggregation. The objects were also reduced in across-track width to 120 m to create hybrid objects. 18

Figure 2.5 Example comparison of object (left), hybrid (middle) and grid-cell (right) data aggregation approaches. The left panel shows an example of a MYI object (outlined in red), which represents a homogeneous ice zone overlaid on the f_p product. The f_p product shows melt pond pixels in blue, and ice pixels in white. The gray line represents the track of thickness and roughness data, which intersects the object. Similarly, the middle panel shows a hybrid object (outlined in red) and the right panel shows 120 × 120 m grid-cells centered on the thickness/roughness track. The hybrid objects were created to account for the footprints of the thickness and roughness sensors. 20

Figure 2.6 Winter sea ice surface roughness (top left), smoothed surface roughness (top right), winter sea ice thickness (bottom left) and spring f_p (bottom right) distributions. FYI is shown in blue and MYI in red. Mean (μ) and standard deviations (σ) are given by ice type. f_p distributions were calculated using hybrid-object aggregation at the medium scale. 22

Figure 2.7 Scatter plots of f_p as a function of mean thickness at the medium scale using object (left), hybrid object (middle) and 240 m grid-cell (right) aggregation approaches. Spearman correlation coefficients (r_s) and corresponding p-values are shown for pooled FYI and MYI data. 23

Figure 2.8 A rational function OLS model of f_p as a function of mean thickness. The data were aggregated using the hybrid-based approach at the medium scale. A rational function has been fitted to the data (solid blue line), with a 95% confidence interval (dashed blue line). 25

Figure 2.9 Scatter plots of f_p as a function of standard deviation of roughness at the medium scale using object (left), hybrid object (middle) and 240 m grid-cell (right) aggregation approaches. Spearman correlation coefficients (r_s) and corresponding p-values are shown for pooled FYI and MYI data. 26

Figure 2.10 Linear OLS model of f_p as a function of standard deviation of roughness. The data was aggregated using the hybrid-based approach at the medium scale. A linear function has been fitted to the data (solid blue line), with a 95% confidence interval (dashed blue line). 28

Figure 2.11 Scatter plots of f_p as a function of smoothed minimum surface roughness at the medium scale using object (left), hybrid object (middle) and 240 m grid-cell (right) aggregation approaches. Spearman correlation coefficients (r_s) and corresponding p-values are shown for pooled FYI and MYI data. 29

Figure 2.12 Scatter plots of maximum roughness as a function of maximum thickness at the medium scale using object (left) and 240 m grid-cell (right) aggregation approaches. Spearman correlation coefficients (r_s) and corresponding p-values are shown for pooled FYI and MYI data. 32

Figure 2.13 2016 snow depth distributions on FYI (blue) and MYI (red) near Eureka in the CAA. Mean (μ) and standard deviations (σ) are given by ice type. 1792 measurements snow depth measurements were collected on FYI and 1810 measurements on MYI. 34

Figure 3.1 Map showing study area location in Victoria Strait and M'Clintock Channel near Cambridge Bay, NU, in the CAA. 2 *advanced melt* (Advanced Melt S1 and Advanced Melt S2) and 2 *winter* (Winter S1 and Winter S2) RADARSAT-2 scenes were acquired, as well as auxillary data including high resolution GeoEye-1 optical imagery of melt pond covered sea ice from 2015 and aerial photography of melt pond covered sea ice in 2016. 47

Figure 3.2 Flow chart showing statistical ice type separability and classification analyses of RADARSAT Constellation Mission (RCM) parameters. 49

Figure 3.3 Histograms of CP parameters that exhibited the highest KS separability for Winter S1 (top) and Winter S2 (bottom). FYI distributions are shown in green, DFYI in blue and MYI in brown. 55

Figure 3.4 Histograms of CP and linear parameters that exhibited the highest KS separability for Advanced Melt S1 (top) and Advanced Melt S2 (bottom). FYI distributions are shown in green, DFYI in blue and MYI in brown. 58

Figure 3.5 Winter S1 (FQ15) classification results. (a) CIS ice chart depicting dominant sea ice stage of development (no distinction is made between FYI and DFYI in charts). The black polygon shows the location of Winter S1 RADARSAT-2 image acquisition (b) Freeman-Durden decomposition RGB composite of the RADARSAT-2 image used to simulate the CP parameters. Red corresponds to dominant double bounce scattering, green to volume scattering and, blue to surface scattering. (c) RCM RH backscatter. (d) SVM classification output using 3 most separable CP parameters as input variables. (e) Classified image using CP parameters as well as GLM and GLV texture parameters as input variables. 61

Figure 3.6 Winter S1 (FQ15) Freeman-Durden decomposition of the RADARSAT-2 scene used to simulate the RCM parameters is shown in (a). Classification input variables are σ^0_{RR}, shown in (b), H_i, shown in (c) and S_0, shown in (d). 63

Figure 3.7 Winter S2 (FQ21) classification results. (a) CIS ice chart depicting dominant sea ice stage of development. The black polygon is showing the location of Winter S1 RADARSAT-2 acquisition (b) Freeman-Durden decomposition RGB composite of quad-pol RADARSAT-2 image used to simulate the RCM parameters. Red corresponds to dominant double bounce scattering, green to volume scattering and, blue to surface scattering. (c) RCM RH backscatter. (d) SVM classification output using 3 most separable RCM parameters as input variables. (e) Classified image using RCM parameters with highest ice type separability and GLCM Mean and GLCM Variance texture parameters as input variables. 64

Figure 3.8 Winter S2 Freeman-Durden decomposition of the RADARSAT-2 scene used to simulate the RCM parameters is shown in (a). Classification input variables are H_i shown in (b), S_0 shown in (c) and, $CPSeaIce_{Depol}$ shown in (d). 65

Figure 3.9 Advanced Melt S1 (FQ4) classification results. (a) CIS ice chart depicting dominant sea ice stage of development. The black polygon shows the location of Advanced Melt S1 acquisition (b) Freeman-Durden decomposition RGB composite of quad-pol RADARSAT-2 image used to simulate the RCM parameters. Red corresponds to dominant double bounce scattering, green to volume scattering and, blue to surface scattering. (c) RCM RH backscatter. (d) SVM classification output using 3 most separable RCM parameters as input variables. (e) Classified image using RCM parameters with highest ice type separability and GLCM Mean and GLCM Variance texture parameters as input variables. 67

Figure 3.10 6 by 6 km panels of σ^0_{HH} depicting signature reversal in original Advanced Melt S1 RADARSAT-2 imagery. A mixture of FYI and MYI in the winter is shown in (a) and subsequent advanced melt conditions in (b). 68

Figure 3.11 Advanced Melt S1 (FQ4) co-located panels coincident with the high resolution GeoEye-1 optical image. (a) GeoEye-1 optical imagery acquired on June 25, 2015, (b) Collocated winter RADARSAT-2 image, σ^0_{HH}, (c) σ^0_{HH} of the Advanced Melt S1 RADARSAT-2 image used to simulate the RCM parameters, (d) σ^0_{RR}, (e) S_2 and, (f) $m\chi v$. The red arrows point to high intensity areas associated with FYI. 69

Figure 3.12 Advanced Melt S2 (SQ21) classification results. (a) CIS ice chart depicting dominant sea ice stage of development. The black polygons shows the location of Advanced Melt S2 acquisition (b) Freeman-Durden decomposition RGB composite of quad-pol RADARSAT-2 image used to simulate the RCM parameters. Red corresponds to dominant double bounce scattering, green to volume scattering and, blue to surface scattering. (c) RCM RH backscatter. (d) SVM classification output using 3 most separable RCM parameters as input variables. (e) Classified image using RCM parameters with highest ice type separability and GLCM Mean and GLCM Variance texture parameters as input variables. 71

Figure 3.13 6 by 6 km σ^0_{HH} (dB) panels depicting signature merging in original Advanced Melt S2 RADARSAT-2 imagery. A mixture of FYI and MYI in the winter is shown in (a) and subsequent advanced melt conditions in (b). 72

Figure 3.14 σ^0_{HH} backscatter of a collocated RADARSAT-2 winter scene is shown in (a) Advanced Melt S2 RCM classification input variables were H_i (shown in b), S_0 (shown in c) and $CPSeaIce_{Depol}$ (shown in d). The dots in (a) correspond to Figure 3.15, with the northernmost point corresponding to the photo in Figure 3.15a, progressing to the southernmost point, with the corresponding photo in Figure 3.15d. 73

Figure 3.15 Imagery from aerial photography survey acquired over the area covered by Advanced Melt S2. The survey was conducted on June 21st, 2016, two days prior to the acquisition of Advanced Melt S2. The locations of the photos coincide with the point locations in Figure 3.15a, with the photo in panel (a) corresponding to the northernmost point in Figure 3.15a, and progressing to (d) corresponding to the southernmost point. 73

Figure 3.16 Comparison of overall classification accuracies by incidence angle and season. FQ15 and FQ21 correspond to Winter S1 and Winter S2, respectively. Similarly, FQ4 and SQ21 correspond to Advanced Melt S1 and Advanced Melt S2, respectively. 74

List of Acronyms and Symbols

CAA – Canadian Arctic Archipelago

CDF – Cumulative Distribution Function

CIS – Canadian Ice Service

CP – Compact Polarimetry

CryoVex – CryoSAT Validation Experiment

CSA – Canadian Space Agency

CUPs – Current-use Pesticides

DFYI – Deformed First-year Ice

EM – Electromagnetic

EO – Earth Observation

ETM+ – Enhanced Thematic Mapper Plus

FQ – Fine resolution Quad-polarization beam

f_p – Melt Pond Fraction

FYI – First-year Ice

FYID – First-year Ice Dominated

GLCM – Grey Level Co-occurrence Matrix

ICE-CAMPS – Ice Covered Ecosystem – CAMbridge Bay Process Studies

KS – Kolmogorov-Smirnov

MEOPAR – Marine Environmental Observation Prediction and Response Network

MERIS - Medium Resolution Imaging Spectrometer

MODIS – Moderate Resolution Imaging Spectroradiometer

MR50 – Medium Resolution 50m Mode

MYI – Multiyear Ice

MYID – Multiyear Ice Dominated

NSERC – National Sciences and Engineering Research Council

NSTP – Northern Scientific Training Program

OBIA – Object Based Image Analysis

OCPs – Organochlorine Pesticides

OiB – Operation IceBridge

OLS – Ordinary Least Squares

OSA – Ocean - Sea Ice - Atmosphere

RCM – RADARSAT Constellation Mission

r_s – Spearman’s Correlation Coefficient

RS-2 – RADARSAT-2

SAR – Synthetic Aperture Radar

SQ – Standard resolution Quad-polarization beam

SVM – Support Vector Machine

ULS – Upward Looking Sonar

Acknowledgments

I would like to thank all the people that have made this work possible and a wonderful learning experience. I would first like to thank my supervisor Randy Scharien for his unwavering support, guidance and countless edits. Thank you for believing in me and always encouraging me to be better. I would like to thank my committee member, Dennis Jelinski for asking the tough questions and encouraging me to think outside the box. I would also like to thank my *de facto* committee consisting of Stephen Howell, Christian Haas and Torsten Geldsetzer. Thank you very much for the data, edits, suggestions and encouragement.

The ICE lab has become like a second home to me and I would like to thank all the “ICEcles” for your ideas, proofreading, stimulating conversation and emotional support. I would also like to thank everyone in Department of Geography, especially Olaf Neimann, Jessica Fitterer, Kinga Menu and Johannes Feddema for their advice and inspiration. I have learned a lot from each of you.

Finally, I would like to thank the Marine Environmental Observation Prediction and Response (MEOPAR) Network for making this research possible and providing me with valuable learning opportunities.

Chapter 1 Introduction

1.1 Research Context

The Arctic sea ice system, in the winter period preceding melt, is generally composed of a combination of seasonal, or first-year ice (FYI) which melts every summer, and multiyear ice (MYI) which survives one or more melt seasons. It has been well established that the Arctic sea ice cover has been decreasing in extent, thickness and volume in recent decades [1–3]. These changes have been accompanied by longer melt seasons and a transition from a mainly MYI pack to a thinner FYI dominated system [4]. Sea ice decline has been attributed to increasing regional [5] and global air temperatures [6], increasing sea ice export from the central Arctic during the positive phase of the Arctic Dipole anomaly [7], increased wind speeds in the central Arctic, and the transition to a weaker FYI dominated ice cover which contributes to increased sea ice drift speeds [8], increased summer ocean temperatures [9], and increased solar heating due to regional decreases in albedo [10]. A positive feedback mechanism linked to melt pond coverage during the melt season has been proposed [11].

During the *advanced melt* period, the sea ice cover is dominated by melt ponds which have a lower albedo (0.2 – 0.4) than the surrounding ice (0.5 – 0.7) [12]. With the transition to a smoother FYI ice cover, melt pond extent is expected to increase leading to higher energy absorption and accelerated sea ice decay [11]. Arctic sea ice is a unique ecosystem which hosts a variety of organisms, from primary producers, to sea birds and polar bears, with the effects of sea ice decline felt at every trophic level. Observed decrease in ice thickness in conjunction with increased melt pond coverage have been linked to enhanced light transmittance and primary productivity [13]. Seabird species such as ivory gulls (*Pagophilla eburnean*) and spectacled eiders (*Somateria fischeri*) have experienced dramatic declines associated with decreasing seasonal ice cover, with ivory gull populations declining by as much as 80% [14]. Deteriorating sea ice conditions are causing polar bears (*Ursus maritimus*) to spend more time on land, shift denning northward and engage in more long-distance swimming which puts cubs at risk [15].

In recent decades, advancements in remote sensing technologies have allowed for large influxes of data, informing better understanding of key geophysical sea ice properties. The passive microwave record which extends back to 1979 shows a consistent and accelerating decline in Arctic sea ice extent. Passive microwave sensors are also used to estimate sea ice age distributions by taking advantage of the salinity differences between FYI and MYI, or by utilizing motion tracking algorithms [8]. Historically, sea ice thickness measurements have been obtained using upward looking sonar (ULS) aboard submarines or drifting buoys [4]. These observations are valuable but are spatially and temporally sparse. NASA's Operation IceBridge is an airborne laser altimeter mission which provides tracks of sea ice thickness measurements. Sea thickness measurements are needed at larger spatial scales, thus satellite based estimates are an active area of research. ICESat satellite laser altimeter thickness data is available from 2003-2008. The satellite was decommissioned in August, 2010 with a follow-up ICESat-2 mission scheduled for launch in 2018. Aboard CryoSat-2 is a Ku-band radar altimeter which measures ice freeboard to infer thickness. Although the Ku-band radar altimeter aboard CryoSAT-2 is a state of the art sensor, uncertainties associated with radar penetration, salinity, assumed sea ice density, variations in sea surface roughness and snow loading remain [2,16,17]. Furthermore, sea ice thickness measurements are not obtained during the melt season due to the presence of melt ponds [18]. The Copernicus observation programme lead by the European Space Agency (ESA) is currently providing an unprecedented amount of freely available Earth Observation (EO) data. Upon completion, "the Sentinels" will be composed of six missions aimed at providing data for land management, the marine environment, atmosphere, emergency response, security and climate change. Currently, Sentinel-1A and -1B, Sentinel-2A and -2B, as well Sentinel-3A are operational and provide open access data. The Sentinel-1 satellites are equipped with C-band synthetic aperture radar (SAR), whereas aboard the Sentinel-2 satellites are multispectral imagers (MSI) covering 13 spectral bands with a swath width of 290 km and a high spatial of resolution of 10 m. The two Sentinel-3 satellites will carry Ocean and Land Colour Instruments (OLCI), as well as Sea and Land Surface Temperature Radiometers (SLSTR), a Ku- and C-band SAR altimeters and a microwave radiometer.

SAR has been recognized as an invaluable tool for sea ice monitoring due to its all-weather capability, global coverage and near daily acquisition ability over a study area [19]. SAR is an active microwave sensing system which transmits and receives combinations of horizontally and vertically polarized microwave energy at varied frequencies. Microwave energy, like other forms of electromagnetic (EM) radiation, consists of orthogonally oriented electric and magnetic fields. Polarization of an EM wave refers to the orientation of the electric field. If the electric field is oriented perpendicular to the Earth's surface, then the EM wave is vertically (V) polarized. Whereas, if the electric field is oriented parallel to the Earth's surface the EM wave is said to be horizontally (H) polarized [20]. A single polarization SAR transmits and receives in the same polarizations, giving HH or VV imagery. Whereas, dual polarization systems transmit in a given polarization and receive in both horizontal and vertical orientations (HH and HV or VV and VH). Fully polarimetric SAR can transmit and receive in all four polarization combinations (HH, VV, HV, VH). The most commonly used frequencies and wavelengths for sea ice observation are L-band (1 – 2 GHz, 15 – 30 cm), C-band (4 – 8 GHz, 3.75 – 7.5 cm), X-band (8 – 12 GHz, 2.4 – 3.75 cm) and Ku-band (12.5-18 GHz, 1.7 – 2.4 cm) [19]. While most SAR systems transmit and receive in linear orientations, it is possible to transmit and receive in circular orientations. Compact polarimetric (CP) SAR transmits a circularly polarized wave and receives in vertical and horizontal orientations [21]. Compact polarimetry is of particular interest for EO applications because it can provide comparable polarimetric capabilities of fully polarimetric SAR over large areas. In general, SAR data can be effectively used in conjunction with other remote sensing or *in situ* datasets to investigate geophysical properties of the sea ice cover.

C-band SAR typically has a wavelength of 5.6 cm, which allows the incident energy to interact with both the surface and the volume, with penetration depth highly dependent on the moisture content and salinity of the ice [22]. During dry, winter conditions, the snow cover is transparent to the microwave signal and the dominant scattering mechanisms are surface, volume and double bounce [23]. Surface scattering occurs due to the interaction of the incident microwave energy with the ice surface and depends on the micro-and macro-scale surface roughness of the material. Micro-scale roughness variations of less than the radar wavelength are considered principle drivers for SAR backscatter [24]. However, macro-scale roughness associated with deformation features and tilted ice blocks also strongly impacts backscatter [25]. Typically, smooth FYI is dominated by specular reflection, where the majority of incident energy scatters away from the sensor. As surface roughness increases, for example for deformed FYI or MYI, scattering will occur in all directions, including towards the sensor [22]. As a result, smooth FYI appears dark in SAR imagery, whereas FYI deformation features such as ridges, as well as MYI appear bright. MYI is also dominated by volume scattering due to the presence of air bubbles within the desalinated upper layers [26]. MYI undergoes desalination processes during melt, where the brine that was present in the ice matrix becomes expelled onto the ice surface and into the ocean below through vertical drainage channels. One of important features of volume scattering is depolarization. Depolarization is the process of shifting the polarization orientation of the incident EM wave. Volume scattering is minimal in FYI due to its high salinity which reduces the penetration depth. FYI salinities range between 5 and 8 parts per thousand (ppt), whereas 0.1 to 3 ppt are typical salinities for MYI at 1 to 2 m depths [27]. Finally, double bounce scattering occurs when a corner like surface is present on the ice surface. A strong backscatter intensity will be observed if the corner is facing the SAR sensor, and no response will be observed if it facing away from the radar. Double bounce scattering is not as common in sea ice as in urban landscapes which are dominated by buildings, or forests where the base of tree trunks can act as corner reflectors [22]. Generally, dominant C-band SAR scattering mechanism during winter are relatively well understood compared to the melt season where dominant scattering mechanisms remain an active area of research.

1.2 Research Objectives

The goal of this thesis is to test the following hypotheses: (1) Melt pond fraction can be predicted from winter sea ice thickness and surface roughness, (2) Compact polarimetric SAR enables discrimination of major sea ice types during advanced melting conditions. This thesis contributes to the growing body of literature on melt pond fraction parameterization in sea ice forecast models and, the use of RCM parameters for sea ice observation during *advanced melt*.

1.3 Thesis Structure

This thesis is organized into two individual papers that address the research hypotheses. The first paper (Chapter 2) titled “Linking Regional Winter Sea Ice Thickness and Surface Roughness to Spring Melt Pond Fraction on Landfast Arctic Sea Ice” addresses the first hypothesis by establishing quantitative relationships between spring melt pond fraction and winter sea ice thickness and surface roughness using GeoEye-1 high resolution optical imagery and electromagnetic sounding measurements of sea ice thickness, and laser scanner estimates of surface roughness. The manuscript was published on December 26, 2017 in the academic journal of Remote Sensing. Chapter 3 corresponds to the second paper, “Optimal Compact Polarimetric Parameters and Texture Features for Discriminating Major Sea Ice Types during the Winter and Advanced Melt”. The manuscript addresses the second hypothesis by assessing the utility of simulated RCM parameters for major ice type discrimination during the melt season. The second paper has been formatted for publication in the academic journal Canadian Journal of Remote Sensing. Chapter 4 provides a summary of research findings, recommendations for future work and co-author acknowledgments.

1.4 References

1. Meier, W. N. Actic sea ice in tranformation: A review of recent observed changes and impacts on biology. *Rev. Geophys.* **2015**, *53*, 1–33, doi:10.1002/2013RG000431.

2. Laxon, S. W.; Giles, K. a.; Ridout, A. L.; Wingham, D. J.; Willatt, R.; Cullen, R.; Kwok, R.; Schweiger, A.; Zhang, J.; Haas, C.; Hendricks, S.; Krishfield, R.; Kurtz, N.; Farrell, S. L.; Davidson, M. CryoSat-2 estimates of Arctic sea ice thickness and volume. *Geophys. Res. Lett.* **2013**, *40*, 732–737, doi:10.1002/grl.50193.

3. Stroeve, J. C.; Kattsov, V.; Barrett, A. P.; Serreze, M.; Pavlova, T.; Holland, M. M.; Meier, W. N. Trends in Arctic sea ice extent from CMIP5, CMIP3 and observations. *Geophys. Res. Lett.* **2012**, *39*, 1–7, doi:10.1029/2012GL052676.

4. Kwok, R.; Rothrock, D. A. Decline in Arctic sea ice thickness from submarine and ICESat records: 1958-2008. *Geophys. Res. Lett.* **2009**, *36*, 1–5, doi:10.1029/2009GL039035.

5. Overland, J. E. Meteorology of the Beaufort Sea. *J. Geophys. Res. Ocean.* **2009**, *114*, 1–10, doi:10.1029/2008JC004861.

6. Bekryaev, R. V.; Polyakov, I. V.; Alexeev, V. A. Role of polar amplification in long-term surface air temperature variations and modern arctic warming. *J. Clim.* **2010**, *23*, 3888–3906, doi:10.1175/2010JCLI3297.1.

7. Wang, J.; Zhang, J.; Watanabe, E.; Ikeda, M.; Mizobata, K.; Walsh, J. E.; Bai, X.; Wu, B. Is the dipole anomaly a major driver to record lows in Arctic summer sea ice extent?

Geophys. Res. Lett. **2009**, *36*, 1–5, doi:10.1029/2008GL036706.

8. Spreen, G.; Kwok, R.; Menemenlis, D. Trends in Arctic sea ice drift and role of wind forcing : 1992 – 2009. *Geophys. Res. Lett.* **2011**, *38*, 1–6, doi:10.1029/2011GL048970.

9. Steele, M.; Ermold, W.; Zhang, J. Arctic Ocean surface warming trends over the past 100 years. *Geophys. Res. Lett.* **2008**, *35*, 1–6, doi:10.1029/2007GL031651.

10. Perovich, D. K.; Richeter-Menge, J. A.; Jones, K. F.; Light, B. Sunlight, water, and ice: Extreme Arctic sea ice melt during the summer of 2007. *Geophys. Res. Lett.* **2008**, *35*, 2–5, doi:10.1029/2008GL034007.

11. Schröder, D.; Feltham, D. L.; Flocco, D.; Tsamados, M. September Arctic sea-ice minimum predicted by spring melt-pond fraction. *Nat. Clim. Chang.* **2014**, *4*, 353–357, doi:10.1038/nclimate2203.

12. Hanesiak, J. M.; Barber, D. G.; De Abreu, R. a.; Yackel, J. J. Local and regional albedo observations of arctic first-year sea ice during melt ponding. *J. Geophys. Res.* **2001**, *106*, 1005, doi:10.1029/1999JC000068.

13. Arrigo, K. R.; Perovich, D. K.; Pickart, R. S.; Brown, Z. W.; van Dijken, G. L.; Lowry, K. E.; Mills, M. M.; Palmer, M. A.; Balch, W. M.; Bahr, F.; Bates, N. R.; Benitez-Nelson, C.; Bowler, B.; Brownlee, E.; Ehn, J. K.; Frey, K.; Garley, R.; Laney, S. R.; Lubelczyk, L.; Mathis, J.; Matsuoka, A.; Mitchell, B. G.; Moore, G. W. K.; Ortega-Retuerta, E.; Pal, S.; Polashenski, C. M.; Reynolds, R. A.; Schieber, B.; Sosik, H. M.; Stephens, M.; Swift, J. H. Massive Phytoplankton Blooms Under Arctic Sea Ice. *Science.* **2012**, *336*, 1408–1408, doi:10.1126/science.1215065.

14. Gaston, A. J.; Mallory, M. L.; Gilchrist, H. G. Populations and trends of Canadian Arctic seabirds. *Polar Biol.* **2012**, *35*, 1221–1232, doi:10.1007/s00300-012-1168-5.

15. Pagano, A. M.; Durner, G. M.; Amstrup, S. C.; Simac, K. S.; York, G. S. Long-distance swimming by polar bears (*Ursus maritimus*) of the southern Beaufort Sea during years of extensive open water. *Can. J. Zool.* **2012**, *90*, 663–676, doi:10.1139/z2012-033.

16. Beaven, S.; Lockhart, G.; Gogineni, S.; Hosseinmostafa, A.; Jezek, K.; Gow, A.; Perovich, D. K.; Fung, A.; Tjuatja, S. Laboratory measurements of radar backscatter from bare and snow-covered saline ice sheets. *Int. J. Remote Sens.* **1995**, *16*, 851–876, doi:10.1080/01431169508954448.

17. Ricker, R.; Hendricks, S.; Perovich, D. K.; Helm, V.; Gerdes, R. Impact of snow accumulation on CryoSat-2 range retrievals over Arctic sea ice: An observational approach with buoy data. *Geophys. Res. Lett.* **2015**, *42*, 4447–4455, doi:10.1002/2015GL064081.

18. Tilling, R. L.; Ridout, A.; Shepherd, A.; Wingham, D. J. Increased Arctic sea ice volume after anomalously low melting in 2013. *Nat. Geosci.* **2015**, *8*, 643–646, doi:10.1038/ngeo2489.

19. Dierking, W. Sea Ice Monitoring by Synthetic Aperture Radar. *Oceanography* **2011**, *24,* 162–173, doi:10.5670/oceanog.2011.65.

20. Ager, T. An introduction to Synthetic Aperture Radar Imaging. *Oceanography* **2013**, *26*, 162–173, doi:10.5670/oceanog.2011.65.

21. Raney, R. K.; Freeman, A. Hybrid-polarity sar architecture. *Eur. Sp. Agency, (Special Publ. ESA SP* **2009**, *668 SP*, 3397–3404.

22. Richards, J. a. *Remote Sensing Digital Image Analysis: An Introduction*; **2009**; ISBN 3642020194.

23. Freeman, A.; Durden, S. L. A three-component scattering model for polarimetric SAR data. *IEEE Trans. Geosci. Remote Sens.* **1998**, *36*, 963–973, doi:10.1109/36.673687.

24. Paterson, J. S.; Brisco, B.; Argus, S.; Jones, G. *In Situ* Measurements of Micro-Scale Surface Roughness of Sea Ice. *Arctic* **1991**, *4*, 140–146.

25. Fors, A. S.; Brekke, C.; Gerland, S.; Doulgeris, A. P.; Beckers, J. F. Late Summer Arctic Sea Ice Surface Roughness Signatures in C-Band SAR Data. **2016**, *9*, 1199–1215.

26. Hallikainen, M.; Winebrenner, D. P. The physical basis for sea ice remote sensing. *Microw. Remote Sens. Sea Ice* **1992**, 29–46, doi:10.1029/GM068p0029.

27. Weeks, W. F. Sea ice: the potential of remote sensing. *Oceanus* **1981**, *24*, 39–48.

Chapter 2 Linking Regional Winter Sea Ice Thickness and Surface Roughness to Spring Melt Pond Fraction on Landfast Arctic Sea Ice

2.1 Abstract

The Arctic sea ice cover has decreased strongly in extent, thickness, volume and age in recent decades. The melt season presents a significant challenge for sea ice forecasting due to uncertainty associated with the role of surface melt ponds in ice decay at regional scales. This study quantifies the relationships of spring melt pond fraction (f_p) with both winter sea ice roughness and thickness, for landfast first-year sea ice (FYI) and multiyear sea ice (MYI). In 2015, airborne measurements of winter sea ice thickness and roughness, as well as high-resolution optical data of melt pond covered sea ice, were collected along two ~5.2 km long profiles over FYI- and MYI-dominated regions in the Canadian Arctic. Statistics of winter sea ice thickness and roughness were compared to spring f_p using three data aggregation approaches, termed *object* and *hybrid-object* (based on image segments), and regularly spaced *grid-cells*. The hybrid-based aggregation approach showed strongest associations because it considers the morphology of the ice as well as footprints of the sensors used to measure winter sea ice thickness and roughness. Using the hybrid-based data aggregation approach it was found that winter sea ice thickness and roughness are related to spring f_p. A stronger negative correlation was observed between FYI thickness and f_p (Spearman $r_s = -0.85$) compared to FYI roughness and f_p ($r_s = -0.52$). The association between MYI thickness and f_p was also negative ($r_s = -0.56$), whereas there was no association between MYI roughness and f_p. 47% of spring f_p variation for FYI and MYI can be explained by mean thickness. Thin sea ice is characterized by low surface roughness allowing for widespread ponding in the spring (high f_p) whereas thick sea ice has undergone dynamic thickening and roughening with topographic features constraining melt water into deeper channels (low f_p). This work provides an important contribution towards the parameterizations of f_p in seasonal and long-term prediction models by quantifying linkages between winter sea ice thickness and roughness, and spring f_p.

Keywords: Arctic; sea ice thickness; roughness; melt pond fraction; object-based image analysis (OBIA)

2.2 Introduction

Due to its sensitivity to fluctuations in climate, Arctic sea ice is often pointed to as a clear indicator of climate change. It has been well established that in recent decades the Arctic sea ice cover has been decreasing in extent, thickness and volume [1,2]. These changes are accompanied by a longer melt season and a transition from a mainly multiyear ice (MYI) regime to a first-year ice (FYI)-dominated system [3]. Currently, climate models are capturing the observed sea ice decline; however large model uncertainties associated with underrepresentation of internal variability and key physical processes remain [4]. Improved characterization of physical processes in forecast models will advance our understanding of how the sea ice cover is likely to evolve in the future. Key aspects of sea ice decay that are poorly represented in climate models are melt pond formation and evolution. Melt ponds are shallow, meter-scale features that form on sea ice during the spring/summer melting periods, decreasing the surface albedo and enhancing mass and energy exchanges between the atmosphere, sea ice cover and ocean [5]. The current understanding of melt evolution is based primarily on detailed *in situ* observations, and macro-scale satellite-based studies necessary to initialize the models are hindered by pervasive cloud cover during the spring and summer months.

It is important to understand and predict melt pond evolution at the macro-scale, because the shift in ice type at the pan-Arctic scale from MYI- to FYI-dominated has potentially profound consequences on the climate system, particularly from an energy balance perspective [6]. The much lower surface albedo of melt ponds (0.2–0.4) compared to the surrounding ice (0.5–0.7) increases energy transfer to the upper ocean layers [6,7]. Melt ponds on FYI transmit four times more incident light than snow free ice, which allows for and encourages large under-ice phytoplankton blooms [8]. Melt ponds have also been shown to enhance the delivery of legacy organochorine pesticides (OCPs) and current-use pesticides (CUPs) into the upper ocean layers [9]. This process is strongly favored for FYI, because it exhibits large expanses of melt ponds (larger surface area for “atmospheric scrubbing”) and higher brine concentrations, which allows for larger and more numerous drainage channels. Finally, spring f_p has been linked with subsequent September minimum sea ice extent suggesting a possible positive feedback mechanism where lower melt pond surface albedo promotes increased melting, thus further increasing melt pond fraction and enhancing energy absorption into the sea ice cover [10].

Melt pond formation and evolution vary considerably between FYI and MYI, with fine-scale observations pointing to MYI areal melt pond fraction (f_p) being dominated by surface roughness, whereas ponding is relatively unconstrained on FYI, and f_p is higher [11]. FYI and MYI f_p evolution can be broken down into 4 stages: (1) topographic control; (2) hydrostatic balance; (3) ice freeboard control; and (4) fall freeze-up or ice break-up [12]. Stage 1 begins with snow melt and melt pond formation and is characterized by positive hydraulic head and a rapid increase in f_p that concludes with a seasonal peak in f_p. The undulating topography of MYI restricts melt pond expansion and constrains melt water into deeper and narrower channels leading to peak f_p of approximately 0.4 compared to FYI, which can reach an f_p of greater than 0.7 [13]. During Stage 2, variations in f_p for both FYI and MYI are dominated by diurnal cycles in hydrostatic balance between melt water production and drainage. Melt ponds form interconnected networks that enhance lateral melt water flow to macroscopic flaws such as ice floe edges, cracks and seal holes (the latter in FYI only) [13]. Through preferential melting, melt ponds continue to deepen, lateral flow decreases, vertical channels begin to dominate drainage and a hydraulic head of zero marks the end of Stage 2. During Stage 3, the ice continues to thin and freeboard decreases. Finally, Stage 4 marks the complete melt out or break-up of FYI and beginning of the open water season. The ice that remains through Stage 4 until subsequent fall freeze-up becomes MYI [8].

A lack of observations over large spatial and temporal scales, as well as the uncertainty in available observations, are major challenges for understanding key sea ice properties such as ice thickness, roughness, as well as f_p and their macro-scale relationships. f_p observations are mainly obtained using medium- to low-resolution satellite optical imagery such as Terra/Aqua Moderate Resolution Imaging Spectroradiometer (MODIS), the ENVISAT Medium Resolution Imaging Spectrometer (MERIS) and the Landsat-7 Enhanced Thematic Mapper Plus (ETM+). Classification of MODIS data using a spectral unmixing algorithm has shown promise for estimating f_p for the entire Arctic [14]. Although these data allow for estimating f_p over large spatial scales, they lack in spatial resolution and are limited by pervasive cloud cover at high latitudes. Significant research has been dedicated to retrieval of f_p using passive microwave and SAR data, which operate independently of sunlight and cloud cover [15,16]. With the emergence of high-resolution remote sensing imagery, it has become possible to isolate objects of interest that are composed of multiple pixels. Object-based image analysis (OBIA) aims to isolate discrete features of interest from remotely sensed data using image segmentation techniques that date back to the 1970s [17]. Segmentation is the process of generating accurate, representative and spatially appropriate objects from an image. Once created, these objects can be integrated into statistical analyses and image classification. OBIA builds off more commonly used remote sensing techniques such as edge-detection, feature extraction and image classification to create vector representations of real-world geographic entities such as agricultural fields, river and ice floes [18]. These vectorized features are easily integrated into analyses by providing physically meaningful extents for data aggregation and further quantitative study. Unlike pixel-based image analysis, OBIA addresses the modifiable areal unit problem, which is a source of statistical bias associated with the shape and scale of data aggregation features. OBIA enables analysis at appropriate, and non-arbitrary spatial scales representative of physical boundaries such as extents of individual sea ice floes [19]. OBIA can also introduce a variety of contextual (e.g., land use type, ice type), texture (e.g., homogeneity, entropy, and dissimilarity) and shape (e.g., area) variables compared to pixel-based analysis, which only provides spectral information [18]. OBIA has been shown to improve iceberg detection using wide-swath SAR images in the Amundsen Sea [20].

It has been shown that spring melt pond fraction can be used to accurately forecast September minimum sea ice extent. This result is explained by the following positive feedback mechanism: increase in melt pond fraction reduces the surface albedo; a lower albedo leads to more melting; increased melting leads to a further increase in melt pond fraction [10]. In addition, it is generally understood that sea ice that is thin and has low surface roughness in the winter will have a high spring f_p and ice that has been dynamically thickened and roughened will have a low f_p [11] (Figure 2.1). This study aims to establish a link between winter conditions and spring f_p in order to evaluate to what extent the ice cover is pre-conditioned for spring melt. The goal of this paper is to quantify relationships between winter sea ice thickness, roughness, and spring f_p for an area comprising a mixture of landfast FYI and MYI in the Canadian Arctic Archipelago (CAA). Explicitly we first investigate the macro-scale relationships between winter sea ice thickness and roughness, and spring f_p; followed by an investigation of how these relationships differ between FYI and MYI.

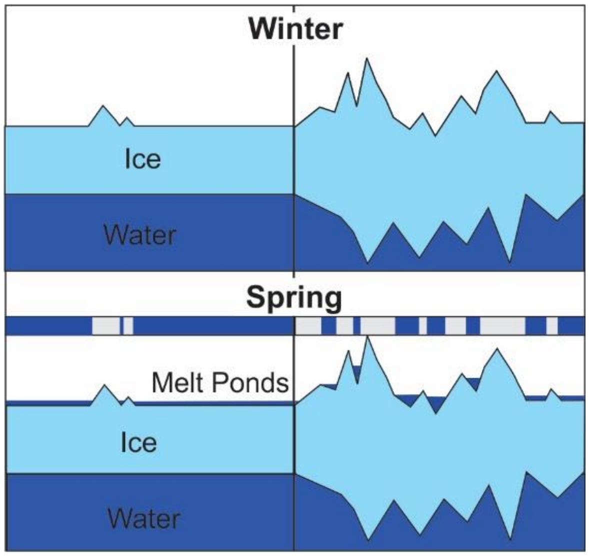

Figure 2.1 Schematic of our melt pond formation hypothesis derived primarily from *in situ* studies of sea ice evolution. Top panel shows a cross-section of pre-melt conditions of thin/smooth (left) and thick/rough (right) sea ice prior to melt. Bottom panel shows a cross-section during spring conditions. Left panel shows smooth/level ice dominated by extensive melt ponds. Right panel shows lower melt pond coverage due to high surface topography. Blue and grey bar in the center illustrates a bird's-eye view of melt pond extent.

2.3 Materials and Methods

2.3.1 Study Area

Airborne winter snow plus sea ice thickness and surface roughness transects and satellite GeoEye-1 optical and RADARSAT-2 (RS-2) SAR images were collected in Victoria Strait region of the CAA during April and June 2015 (Table 2.1; Figure 2.2). Victoria Strait is part of the Northwest Passage in the CAA, which typically contains a mixture of FYI and MYI. The sea ice in the CAA is not strongly affected by wind driven movement because the ice is landfast for six to eight months of the year [21]. Furthermore, wind driven movement of sea ice is restricted by the narrow channels that dominate the CAA [22]. During the melt season, MYI drifts into and subsequently through the CAA from the central Arctic during late summer and early fall and becomes locked in place by FYI that forms in the fall and early winter [23]. This makes for an ideal study area for understanding the evolution of sea ice from winter to summer conditions, without the need for tracking mobile ice.

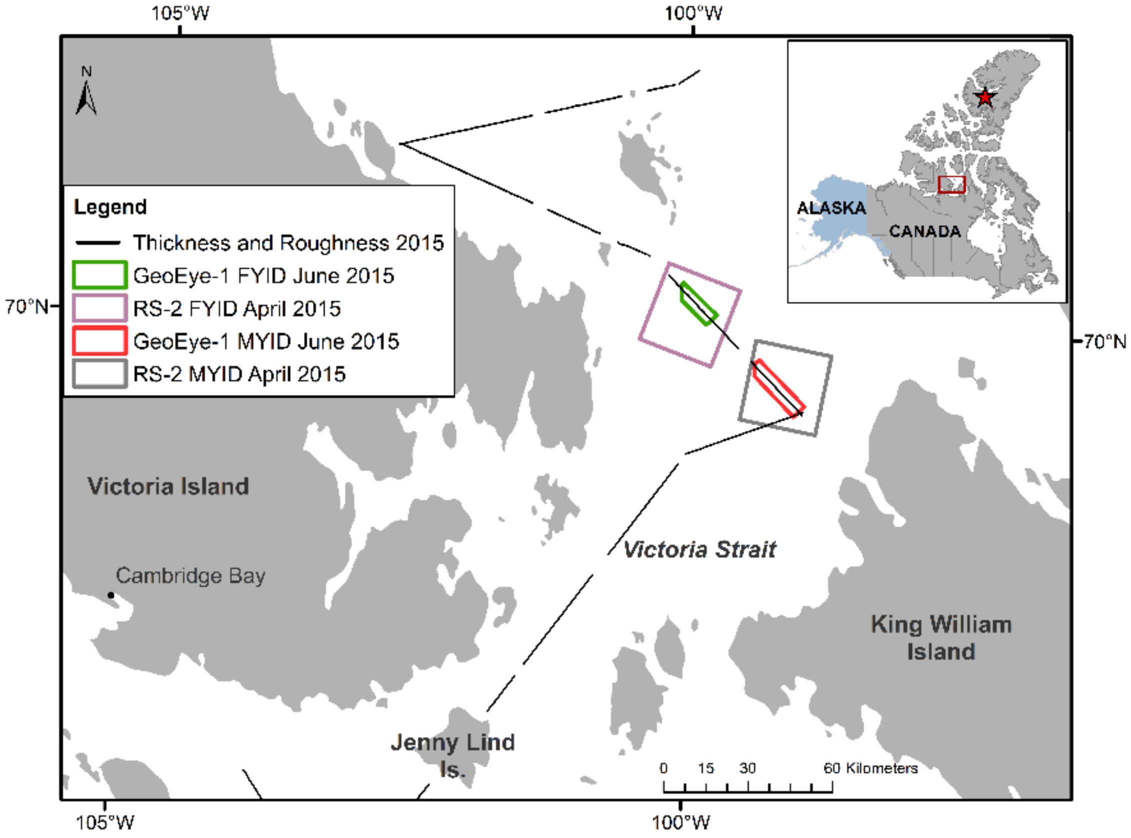

Figure 2.2 Map of study area located in the CAA depicting the locations of RADARSAT-2 (RS-2) image acquisitions shown in purple and gray for FYI-dominated (FYID) and MYI-dominated (MYID) areas respectively. Corresponding GeoEye-1 optical image coverages for FYID are shown in green and MYID zone are shown in red. The track of airborne winter snow plus sea ice thickness and surface roughness point measurements is shown in black. The location of *in situ* snow depth measurements is shown by a red star in the outset map.

Table 2.1 Description of the datasets.

Parameter	Instrument	Measurement Approach	Platform	Acquisition Dates	Description
Snow plus Ice Thickness	EM-bird	Electromagnetic induction and laser altimeter	Airborne	19 April 2015	Spatial resolution: 6.0 m Swath width: ~120 m Accuracy: 0.15 m
Ice Surface Roughness	Riegel Laser Measurement System Q120	2D laser scanner	Airborne	19 April 2015	Spatial resolution: 1.2 m Swath width: 105 m Accuracy: 0.025 m
Melt Pond Fraction (f_p)	GeoEye-1	Multispectral (VIS/NIR)	Satellite	25 June 2015 26 June 2015	Spatial resolution: Panchromatic (0.5 m), Multispectral (2.0 m) Spectral resolution: RGBNIR
Objects	RADARSAT-2	C-band frequency SAR	Satellite	23 April 2015 25 April 2015	23 April 2015 Pixel Spacing (azimuth × range): 5.1 × 4.7 m Incidence angle: 40.2–41.6° Polarization: Fine Quad 25 April 2015 Pixel spacing (azimuth × range): 4.9 × 4.7 m Incidence angle: 22.3–24.2° Polarization: Fine Quad

The FYI-dominated (FYID) zone (Figure 2.3, left) is characterized by thinner and smoother ice compared to the MYI-dominated (MYID) ice zone (Figure 2.3, right). The majority of the ice within the FYID zone is under 2.5 m thick, compared to the MYID zone, which is dominated by ice thicker than 2.5 m. Similarly, the FYID zone is smoother than the MYID, with areas of thicker ice corresponding to rougher ice in both areas.

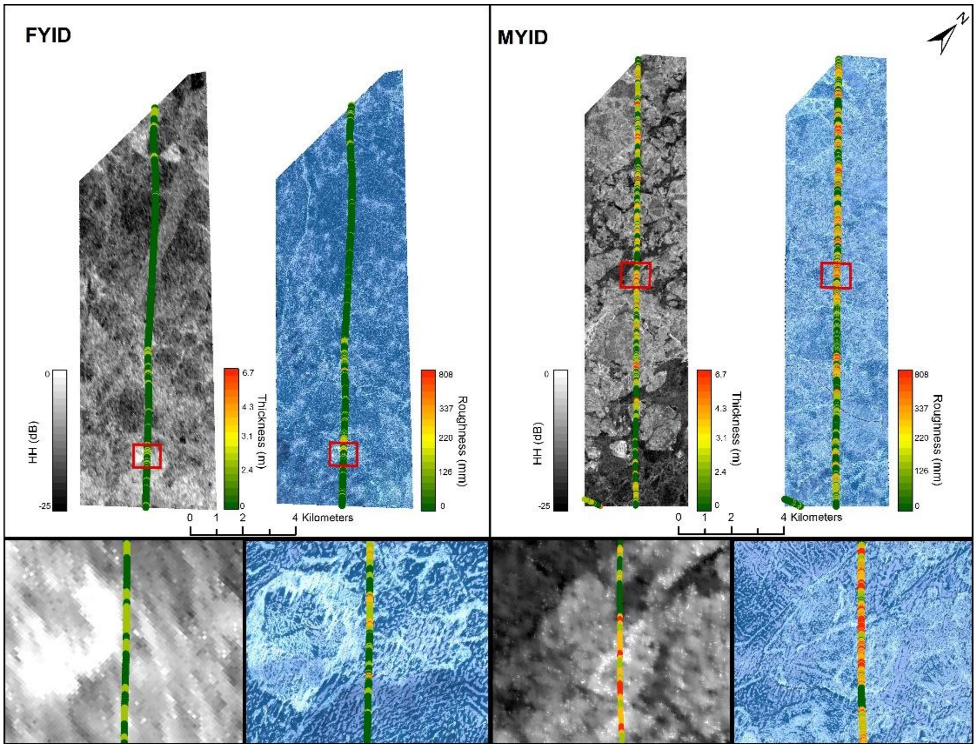

Figure 2.3 FYID (left) and MYID (right) ice zones. The first image in each panel is a winter RS-2 SAR image of the overlain by winter snow plus sea ice thickness measurements. The second image depicts the co-located spring GeoEye-1 optical scene of melt pond covered sea ice overlain by surface roughness measurements. Bottom panels show zoomed in data within the extents of the red polygons directly above each panel.

2.3.2 Data and Preprocessing

Airborne winter snow plus sea ice thickness and surface roughness data were acquired during a late winter survey flown on 19 April 2015 [24] (Table 2.1; Figure 2.2). The survey was conducted in late April in order to capture the late winter conditions indicative of maximum sea ice thickness and reduce the amount of surface variability associated with atmospheric processes such as surface erosion and wind-driven snow redistribution [24]. The snow plus ice thickness was obtained using an airborne electromagnetic (EM) thickness sounding instrument [25]. The EM instrument induces an EM-field in the conductive sea water under the resistive sea ice from which the height of the instrument above the ice/water interface can be derived [25]. A single-beam laser altimeter included in the EM instrument measures the height of the system above the top of the snow cover. The difference between those two measurements is the total thickness, i.e., snow plus ice thickness. It is not possible to distinguish between snow and ice thicknesses because both snow and ice are very resistive. Therefore snow plus ice thickness is hereafter referred to as ice thickness [24,25]. This strongly oversamples the ice because EM measurements have a footprint of approximately 3 to 4 times the instrument height above the ice. With typical instrument heights below 30 m this corresponds to a footprint of up to 120 m. The sampling rate was 10 scans per minute therefore thickness observations were obtained approximately every 6 m.

A Riegel Laser Measurements Systems (Riegel LMS) Q120 near infrared laser scanner was used to collect 2D swaths of relative surface elevation measurements. Each scan line was then approximated with a flat surface hyperbolic equation and surface roughness was calculated from each scan line as the standard deviation of the difference between measured and fitted surfaces [26]. The obtained surface roughness therefore corresponds to root-mean-square (RMS) roughness along the approximately 105 m wide swath perpendicular to the flight direction. The scanning rate was 50 lines per second, resulting in surface roughness measurements of approximately 1.2 m apart. Two high-resolution panchromatic (0.5 m) and multispectral (2.0 m) optical image bundles of spring melt pond covered FYID (23 × 5.3 km) and MYID (26.5 × 5.2 km) zones were acquired on June 25 and 26, 2015 from the GeoEye-1 sensor (Figure 2.3). In order to combine the high spatial resolution of the panchromatic imagery and high spectral resolution of the multispectral imagery, image pairs were fused together using a Gram-Schmidt (GS) pan-sharpening algorithm. The GS algorithm was chosen because it preserves the spectral and spatial integrity of the original imagery [27]. Pan-sharpened images were classified using a Maximum Likelihood (ML) supervised classification algorithm to yield a binary output: ice (0) and pond (1). Classification accuracies were calculated using confusion matrices built from a range of 50 to 96 samples representing homogeneous ice and melt pond areas. This approach yielded overall accuracies of >99% with kappa coefficients of >0.9. The classified images allowed for calculation of f_p for regions of interest in the scene using the following equation:

$$fp = \frac{\sum Pond\ Pixels}{Total\ Count} \tag{1}$$

where $\sum Pond\ Pixels$ represent the sum of pond pixels and *Total Count* is the total number of pixels within the region of interest such as an image object or entire scenes. A flow chart depicting the pre-processing chain and subsequent analyses is given in Figure 2.4.

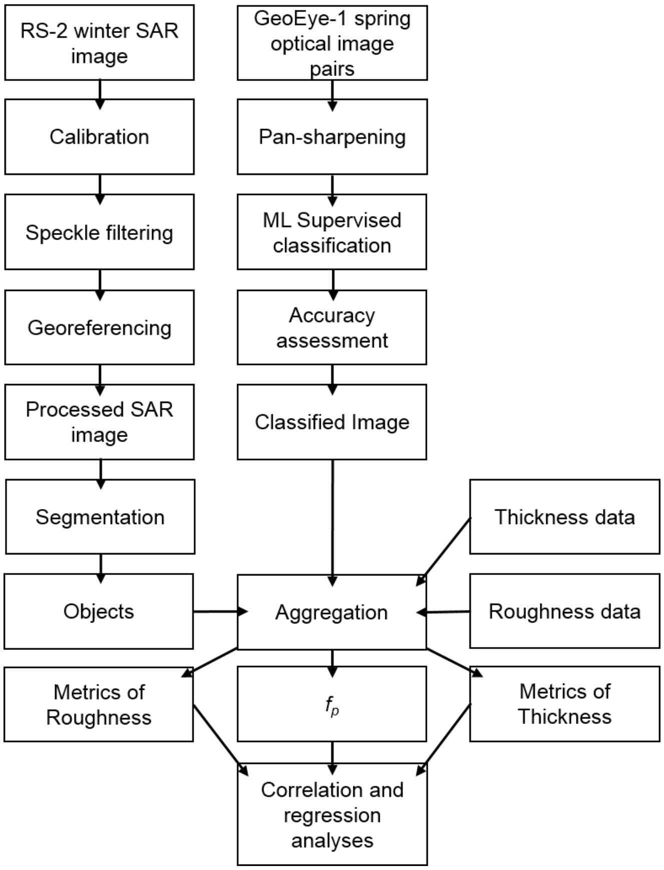

Figure 2.4 Methods flow chart of RS-2 and GeoEye-1 image processing, segmentation, data aggregation, and correlation and regression analyses. The calibrated, speckle filtered and georeferenced RS-2 SAR image was segmented into image objects, with the objects used for further OBIA data aggregation. The objects were also reduced in across-track width to 120 m to create hybrid objects.

2.3.3 Object Based, Hybrid and Grid-Cell Image Analysis

Two winter RS-2 Fine Quad-polarization (FQ) format SAR images of the FYID and MYID zones were acquired between 23 and 25 April 2015 were used for segmentation into image objects (Figure 2.4, left). The multiresolution segmentation approach implemented in the OBIA-driven software eCognition (Trimble) was used for segmentation. This approach has been proven to be effective for image segmentation related to cut block and tree crown delineation, classification of agricultural landscapes, ship detection and sea ice studies [28–32]. Using a bottom up region merging approach, objects are generated based on user defined spatial and spectral heterogeneity criteria, as well as a scale criterion used to control object size. Spatial heterogeneity is related to shape of the object, whereas spectral heterogeneity is variance of data within the object [33]. Emphasis was placed on deriving a segmentation that yielded image objects displaying within-object homogeneity and between-object heterogeneity and representing unique ice floes. To account for some uncertainty in boundary delineation, multiple object sets were created by varying the scale parameter in the segmentation algorithm. For the MYID zone, object features at the *fine*, *medium* and *coarse* scales were delineated. For the FYID zone, object features at *fine* and *medium* scales were created. Due to a lack of heterogeneity in the FYID zone, objects were not created at a coarse spatial scale. This was necessary for calculating global FYI and MYI statistics regardless of whether objects originated in FYID or MYID zones.

Three different approaches for aggregating and deriving statistics of ice thickness, roughness, and f_p data were used (Figure 2.5). The first approach, *object*, used original image objects that intersected the airborne track. The second approach, *hybrid*, used original image segmented objects intersecting the flight line but also accounted for the across-track footprint of the airborne laser scanner (~105 m). The *hybrid objects* were generated by reducing the extent of the original objects to an across-track width of 120 m. The two approaches yielded a total of 61, 50 and 41 objects representative of MYI floes from *fine*, *medium*, and *coarse* scale segmentation, respectively. Conversely, *fine* and *medium* scale segmentation of FYI yielded 53 and 33 objects, respectively. Finally, the third approach involved the overlay of *grid-cells* centered on the flight line. Two sets of grid-cell features were created for both FYID and MYID zones, one with across-track widths of 120 m and along-track lengths of 120 m, and one with across-track widths of 120 m and along-track lengths of 240 m. This yielded a total of 210 (120 × 120 m) and 103 (120 × 240 m) grid-cells features for the FYI zone, and 109 (120 × 120 m) and 56 (120 × 240 m) grid-cell features for the MYI zone. In order to avoid loss of data, grid-cells that were dominated by FYI and located in the MYID zone were analyzed as FYI, and vice versa.

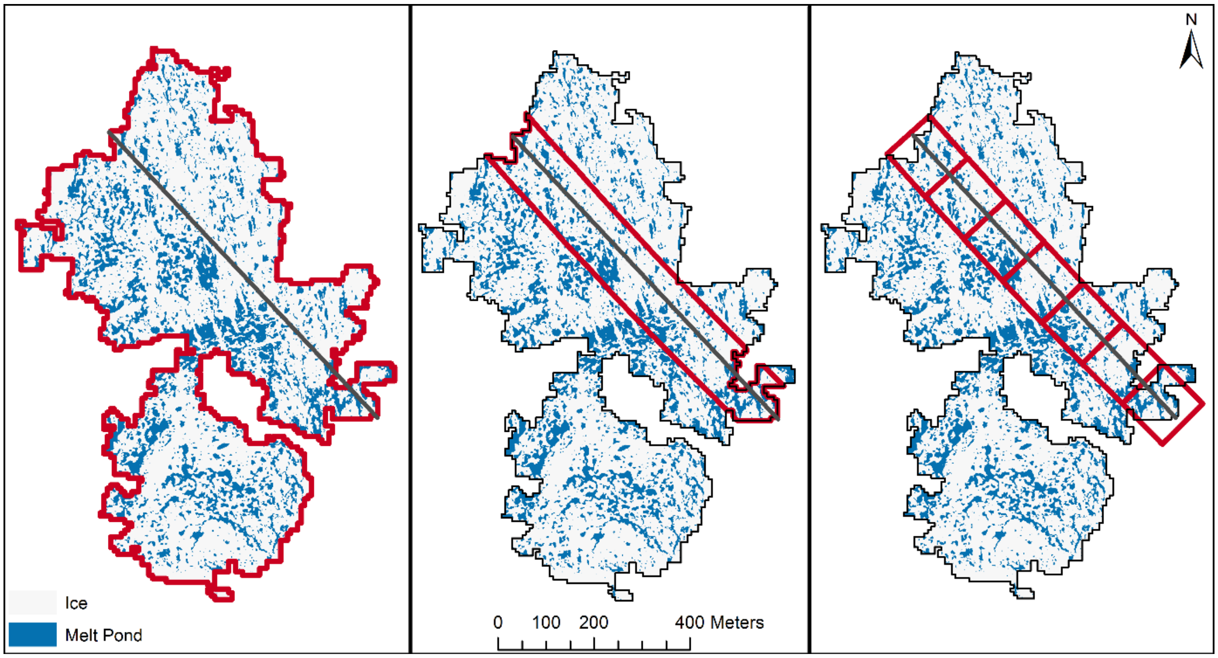

Figure 2.5 Example comparison of object (left), hybrid (middle) and grid-cell (right) data aggregation approaches. The left panel shows an example of a MYI object (outlined in red), which represents a homogeneous ice zone overlaid on the f_p product. The f_p product shows melt pond pixels in blue, and ice pixels in white. The gray line represents the track of thickness and roughness data, which intersects the object. Similarly, the middle panel shows a hybrid object (outlined in red) and the right panel shows 120 × 120 m grid-cells centered on the thickness/roughness track. The hybrid objects were created to account for the footprints of the thickness and roughness sensors.

The average areas (and ranges) of FYI object segments at *fine* and *medium* spatial scales were 0.50 km^2 (0.03–1.42 km^2) and 1.35 km^2 (0.25–5.08 km^2), respectively, whereas the average areas of MYI object segments at *fine*, *medium* and *coarse* scales were 0.29 km^2 (0.03–0.92 km^2), 0.44 km^2 (0.04–1.19 km^2) and 0.63 km^2 (0.04–1.97 km^2), respectively. Hybrid objects were generated by decreasing across-track extent of objects to 120 m. Thus, average areas of hybrid objects were smaller than the object segments, with mean FYI segment areas of 0.05 km^2 (0.002–0.16 km^2) and 0.08 km^2 (0.01–0.31 km^2) for *fine* and *medium* spatial scales, respectively. Average areas of MYI hybrid objects were 0.03 km^2 (0.003–0.10 km^2) at the *fine* scale, 0.04 km^2 (0.01–0.14 km^2) at the *medium* and 0.04 km^2 (0.01–0.14 km^2) at the *coarse* spatial scales. The areas of individual grid-cells remained consistent at 0.014 km^2 and 0.017 km^2 for 120 m and 240 m kernels, respectively.

The three data aggregation approaches at varying spatial scales enabled the examination of relationships between winter sea ice thickness, roughness and f_p, as well as the role of scale and aggregation approaches on those relationships. First, a 2000 point moving average was applied on the roughness data in an attempt to minimize the effects of snow roughness on the surface roughness measurements. 4000 points outside of both the FYID and MYID zones were used for the calculation of the moving average. Probability distributions of winter sea ice thickness, surface roughness, smoothed roughness, and spring f_p were plotted for FYI and MYI, with f_p values obtained using hybrid aggregation at the *medium* scale. For quantifying relationships, aggregated roughness and thickness metrics (minimum, maximum, mean, median and standard deviation (SD)) were each compared to f_p within each aggregation feature. Spearman correlation coefficients were collected to assess the strength of relationships between thickness and roughness, thickness and f_p, and roughness and f_p for FYI and MYI. Spearman correlation was chosen because it is a non-parametric measure of association between two variables. An ordinary least squares (OLS) regression analysis was performed with roughness and thickness as independent variables, and f_p as the dependent variable. For the OLS, a non-linear rational function was fitted to the thickness and f_p data because it is more representative of the expected variation in f_p. It is expected that f_p will behave asymptotically when approaching values of 0 and 1, which will not be captured by a linear function. A rational function is beneficial for modelling physical processes because it allows for better fit of data with a relatively complex distribution, while retaining computational and structural simplicity associated with linear regression. A linear function was fitted to the roughness and f_p data because of its representative fit and computational simplicity.

2.4 Results

2.4.1 Victoria Strait Thickness, Roughness and f_p Distributions in 2015

FYI was characterized by lower winter thickness and surface roughness, and higher spring f_p compared to MYI (Figure 2.6). FYI winter sea ice thickness ranged between 1.6 and 5.5 m, with mean and median thicknesses of 2.1 and 1.9 m, respectively. Conversely, MYI thickness ranged between 1.8 and 6.7 m, with mean and median values of 2.9 and 2.7 m, respectively. The surface roughness on FYI ranged between 0.02 and 0.81 m, with mean and median roughness values of 0.11 and 0.09 m, respectively. Conversely, MYI surface roughness measurements ranged between 0.02 and 0.65 m, with mean and median values of 0.19 and 0.17 m, respectively. Smoothed surface roughness (2000 point moving average) shows increased separability between FYI and MYI. FYI smoothed surface roughness values ranged between 0.08 m and 0.12 m with mean and median values of 0.09 m, whereas MYI smoothed surface roughness values between 0.12 m and 0.24 m were observed with mean and median values of 0.19 m. Finally, spring f_p values were between 0.19 and 0.71 for FYI, and 0.12 and 0.77 for MYI with mean values of 0.43 and 0.29 for FYI and MYI, respectively.

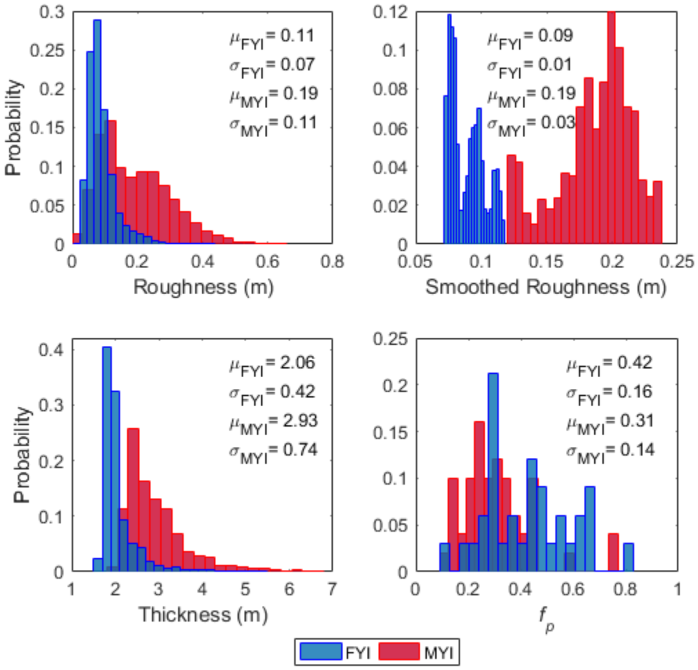

Figure 2.6 Winter sea ice surface roughness (top left), smoothed surface roughness (top right), winter sea ice thickness (bottom left) and spring f_p (bottom right) distributions. FYI is shown in blue and MYI in red. Mean (μ) and standard deviations (σ) are given by ice type. f_p distributions were calculated using hybrid-object aggregation at the medium scale.

2.4.2 Relationship between Thickness and f_p

FYI thickness exhibited statistically significant negative correlations ($p < 0.05$) with f_p for all analyzed scales and aggregation approaches (object, hybrid, grid-cell) (Table 2.2; Figure 2.7). Whereas all metrics of MYI thickness showed statistically significant negative correlations at *fine* scales (object and hybrid) and *120* m grid-cells. Overall, the hybrid-based aggregation approach yielded the strongest statistically significant negative correlations between winter sea ice thickness and f_p for both FYI and MYI, particularly for mean thickness and f_p. Furthermore, the distribution of mean thickness and corresponding f_p values showed less variability using the hybrid-based approach, compared to the object and grid-cell-based approaches at the *medium/240 m* spatial scales (Figure 2.7). This affirms that mean sea ice thickness is strongly related to f_p, particularly within the range of the EM-bird footprint, which is approximately 120 m, depending on the height of the instrument above the sea ice surface [25]. The dependence of f_p on mean thickness can be explained by the presence or absence of deformation features. Thin FYI that has not undergone dynamic forcing is very level/smooth and will experience widespread flooding and higher f_p. Conversely, FYI that has undergone ridging will constrain melt water into deeper surface depressions.

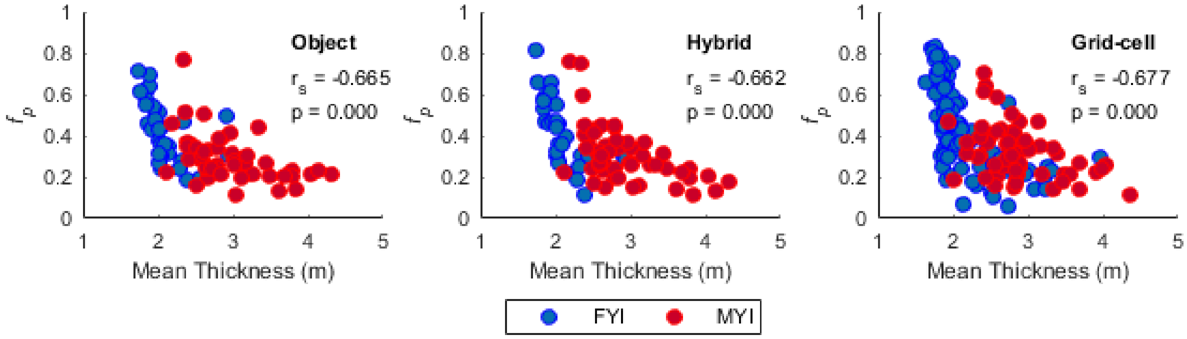

Figure 2.7 Scatter plots of f_p as a function of mean thickness at the medium scale using object (left), hybrid object (middle) and 240 m grid-cell (right) aggregation approaches. Spearman correlation coefficients (r_s) and corresponding p-values are shown for pooled FYI and MYI data.

Table 2.2 Spearman correlation coefficients (r_s) between metrics of winter sea ice thickness and spring f_p for FYI and MYI at fine, medium (med) and coarse spatial scales (object and hybrid) as well as 120 and 240 m grid-cells. Bolded values are statistically significant ($p < 0.05$).

		FYI		**MYI**				**FYI**		**MYI**				**FYI**		**MYI**	
		Fine	Med	Fine	Med	Coarse		Fine	Med	Fine	Med	Coarse		120 m	240 m	120 m	240 m
Min	Objects	**−0.66**	**−0.61**	**−0.37**	**−0.33**	−0.31	Hybrid	**−0.64**	**−0.67**	**−0.32**	−0.27	−0.31	Grid-cell	**−0.61**	**−0.65**	**−0.30**	−0.11
Max		**−0.51**	**−0.67**	**−0.45**	**−0.33**	−0.29		**−0.40**	**−0.73**	**−0.43**	**−0.42**	**−0.40**		**−0.72**	**−0.75**	**−0.46**	**−0.38**
Mean		**−0.72**	**−0.75**	**−0.59**	**−0.54**	**−0.56**		**−0.68**	**−0.85**	**−0.55**	**−0.56**	**−0.59**		**−0.71**	**−0.75**	**−0.47**	**−0.41**
Med		**−0.75**	**−0.71**	**−0.60**	**−0.56**	**−0.58**		**−0.74**	**−0.81**	**−0.59**	**−0.60**	**−0.64**		**−0.69**	**−0.75**	**−0.45**	**−0.44**
SD		**−0.38**	**−0.65**	**−0.36**	−0.25	−0.25		**−0.31**	**−0.72**	**−0.32**	**−0.32**	**−0.34**		**−0.60**	**−0.69**	**−0.47**	**−0.38**

The rational function OLS model used to determine the ability of winter FYI and MYI thickness to explain the variability in spring f_p is shown in Figure 2.8. Thickness and f_p data aggregated at the medium scale using the hybrid aggregation approach were used as inputs for the OLS model because they showed the strongest associations for FYI and MYI in the correlation analysis and exhibited lower variance than the object and grid-cell approaches. The model indicates that 47% of the variation in f_p can be explained using mean thickness according to Equation (2).

$$f_p = \frac{0.5478}{mean\ thickness - 0.8561} \tag{2}$$

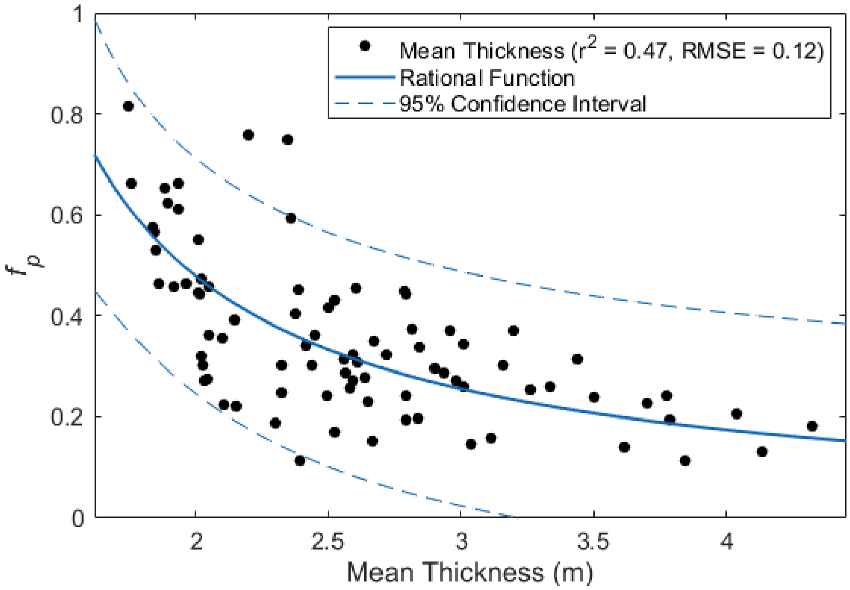

Figure 2.8 A rational function OLS model of f_p as a function of mean thickness. The data were aggregated using the hybrid-based approach at the medium scale. A rational function has been fitted to the data (solid blue line), with a 95% confidence interval (dashed blue line).

2.4.3 Relationship between Roughness and f_p

Surface roughness exhibited moderate negative correlations with f_p for FYI using all three aggregation approaches and at all analyzed spatial scales. Object and hybrid aggregation approaches produced stronger associations compared to the grid-cell method (Table 2.3; Figure 2.9). For FYI, the standard deviation of roughness showed the strongest negative association with f_p, particularly at the *medium* scale. This shows that variability in surface roughness is related to melt pond distribution at the analyzed scale, i.e., greater surface roughness variability leads to lower f_p. A high variability in surface roughness on FYI can be due to the presence of compression ridges and snow sastrugi in areas of otherwise smooth ice. Conversely, low variability in surface roughness on FYI is attributed to smooth, thermodynamically grown ice, which lacks deformation features and easily floods when melt ponds form. Interestingly, metrics of surface roughness did not show any statistically significant correlations with f_p for MYI, except for a weak positive relationship between minimum roughness and f_p at the *fine* spatial scale using object-based aggregation. It is important to note that MYI exhibits greater spatial variability in surface roughness than FYI (Figure 2.3). Quantifying surface roughness on MYI, compared to relatively smooth FYI, and relating it to f_p poses a unique challenge due to the lack of level ice in MYI-dominated areas. Level ice is necessary for the calculation of the local level-ice surface used in the calculation of surface roughness. The absence of level ice will lead to an overestimation of the local level-ice surface, which will lead to an overall overestimation of surface roughness from the 2D laser scanner [26]. Furthermore, areas of uniformly weathered MYI will have a low winter surface roughness, corresponding to a low spring f_p, whereas an area composed of both rough MYI and smooth ice, such as a re-frozen melt pond from a previous melt season, will be characterized by a high standard deviation of relative surface height (i.e., high winter roughness), which will correspond to a high spring f_p due to flooding on areas of smooth ice. Finally, the snow pack will likely be deeper on MYI than FYI because MYI begins accumulating snow earlier than FYI and surface depression in MYI act as catchments for wind-blown snow.

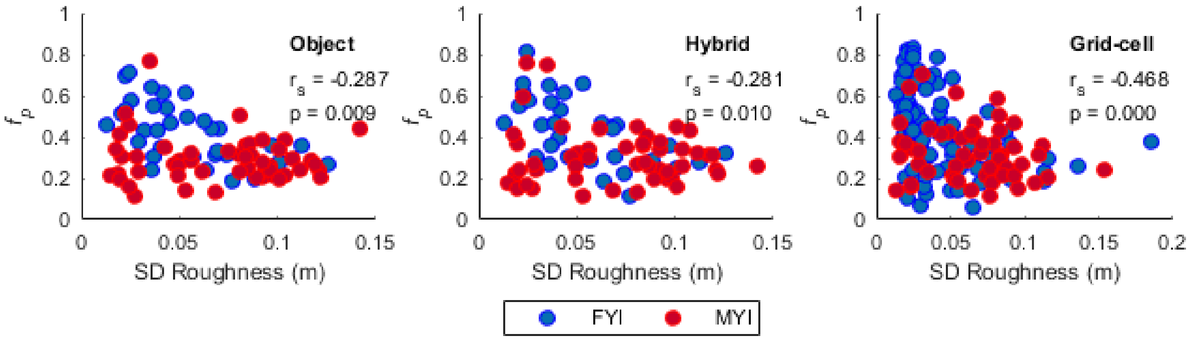

Figure 2.9 Scatter plots of f_p as a function of standard deviation of roughness at the medium scale using object (left), hybrid object (middle) and 240 m grid-cell (right) aggregation approaches. Spearman correlation coefficients (r_s) and corresponding p-values are shown for pooled FYI and MYI data.

Table 2.3 Spearman correlation coefficients (r_s) between metrics of winter sea ice roughness and spring f_p for FYI and MYI at fine, medium (med) and coarse spatial scales (object and hybrid) as well as 120 and 240 m grid-cells. Bolded values are statistically significant ($p < 0.05$).

		FYI		**MYI**				**FYI**		**MYI**				**FYI**		**MYI**	
		Fine	Med	Fine	Med	Coarse		Fine	Med	Fine	Med	Coarse		120 m	240 m	120 m	240 m
Min	Objects	**−0.34**	−0.32	**0.30**	0.21	0.16	Hybrid	**−0.35**	−0.31	0.25	0.27	0.19	Grid-cell	**−0.25**	**−0.26**	−0.05	−0.01
Max		**−0.29**	**−0.57**	0.01	0.05	0.07		−0.20	**−0.53**	0.02	0.04	0.01		**−0.40**	**−0.55**	−0.10	−0.12
Mean		**−0.32**	**−0.53**	0.02	0.03	−0.02		−0.25	**−0.52**	0.04	0.09	0.00		**−0.35**	**−0.42**	−0.09	−0.11
Med		−0.22	**−0.41**	−0.03	0.00	−0.07		−0.14	**−0.36**	0.03	0.06	−0.03		**−0.30**	**−0.37**	−0.07	−0.11
SD		**−0.35**	**−0.59**	−0.07	−0.03	−0.02		**−0.29**	**−0.63**	0.00	−0.01	−0.06		**−0.39**	**−0.54**	−0.10	−0.17

The linear OLS model used to assess the explanatory power of surface roughness for variations in spring f_p is shown in Figure 2.10. It was found that the SD of winter surface roughness explained 11% of the variability in spring f_p. However, surface roughness was a statistically significant variable, which suggests that it contains explanatory power for variability in f_p.

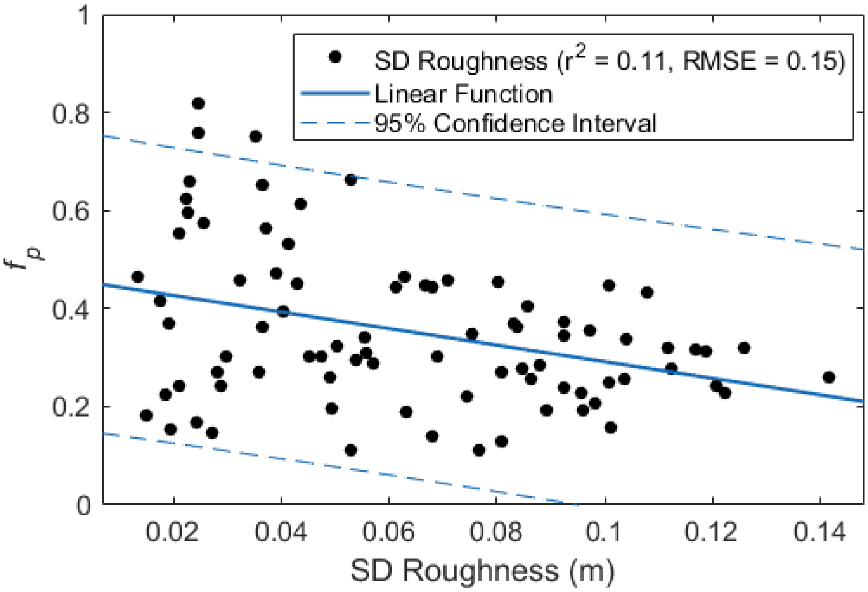

Figure 2.10 Linear OLS model of f_p as a function of standard deviation of roughness. The data was aggregated using the hybrid-based approach at the medium scale. A linear function has been fitted to the data (solid blue line), with a 95% confidence interval (dashed blue line).

2.4.4 Relationship between Smoothed Surface Roughness and f_p

Snow on sea ice will likely affect surface roughness estimates by masking the signal associated with sea ice surface roughness with snow redistribution features such as dunes and snow roughness features such as sastrugi, which are wavelike features that occur on the surface of hard snow that have been redistributed by wind action. A 2000 point (~2400 m) moving average was used to effectively average out footprint-scale variability likely associated with snow roughness and snow redistribution features. A significantly stronger correlation was found between metrics of FYI roughness and f_p, with highest associations observed at the medium spatial scale (Figure 2.11; Table 2.4). Moderate statistically significant correlations can be observed between metrics of MYI roughness and f_p, particularly using the object aggregation approach at the fine spatial scale. It is important to note that smoothing the surface roughness data allows for an increased separability between FYI and MYI (Figure 2.6, top right) compared to unsmoothed data (Figure 2.6, top left). This result suggests that small-scale uncertainties associated with surface roughness measurements are removed when investigating these relationships at regional scales appropriate for studies utilizing satellite observations. However, this approach warrants caution as it introduces increased spatial dependency or spatial autocorrelation between individual measurements.

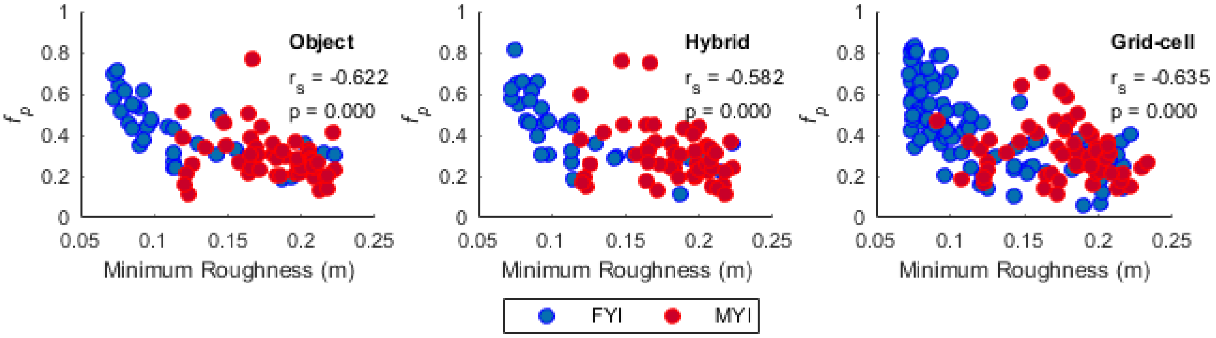

Figure 2.11 Scatter plots of f_p as a function of smoothed minimum surface roughness at the medium scale using object (left), hybrid object (middle) and 240 m grid-cell (right) aggregation approaches. Spearman correlation coefficients (r_s) and corresponding p-values are shown for pooled FYI and MYI data.

Table 2.4 Spearman correlation coefficients (r_s) between metrics of smoothed winter sea ice roughness and f_p for FYI and MYI at fine, medium (med) and coarse spatial scales. The data were aggregated using the hybrid object aggregation approach. Bolded values are statistically significant ($p < 0.05$).

		FYI		**MYI**				**FYI**		**MYI**				**FYI**		**MYI**	
		Fine	Med	Fine	Med	Coarse		Fine	Med	Fine	Med	Coarse		120 m	240 m	120 m	240 m
Min	Objects	**−0.81**	**−0.80**	**−0.31**	**−0.35**	**−0.34**	Hybrid	**−0.77**	**−0.84**	**−0.34**	**−0.29**	−0.25	Grid-cell	**−0.72**	**−0.77**	**−0.20**	−0.23
Max		**−0.79**	**−0.81**	**−0.27**	−0.26	−0.21		**−0.72**	**−0.80**	−0.24	−0.19	−0.09		**−0.72**	**−0.77**	−0.19	−0.22
Mean		**−0.80**	**−0.81**	**−0.29**	**−0.29**	−0.27		**−0.75**	**−0.83**	**−0.28**	−0.23	−0.17		**−0.72**	**−0.77**	−0.19	−0.22
Med		**−0.80**	**−0.81**	**−0.29**	**−0.29**	−0.26		**−0.75**	**−0.82**	**−0.26**	−0.22	−0.16		**−0.72**	**−0.77**	**−0.19**	−0.22
SD		−0.14	−0.34	0.06	0.24	0.28		−0.04	−0.23	0.17	0.19	0.26		**−0.45**	**−0.55**	0.08	0.01

2.4.5 Relationship between Thickness and Roughness

Areas of thick ice are coincident with areas of high surface roughness, particularly for FYID as illustrated in Figure 2.3. Quantitatively, maximum roughness and maximum thickness show a significant positive association for both FYI and MYI using the object aggregation approach (Table 2.5; Figure 2.12). FYI shows a stronger relationship ($r_s = 0.65$) than MYI ($r_s = 0.54$) at *medium* spatial scale. The grid-cell-based aggregation approach yields statistically significant correlations between all metrics of roughness and thickness for FYI, and no significant associations for MYI. The variance in FYI and MYI observations is lower using object-based aggregation, compared to *240 m* grid-cells (Figure 2.12). Finally, it can be seen that variance begins to increase for ice with thickness of greater than approximately 3.75 m. It is expected that thicker ice has undergone more dynamic thickening when compared to thin ice, which would increase both the thickness and the surface roughness. The EM instrument measures the bottom roughness of the ice, which would also be roughened during ridging and rafting. This would lead to an increase in the strength of association between ice thickness and surface roughness.

Table 2.5 Spearman correlation coefficients (r_s) between metrics of winter sea ice roughness and thickness for FYI and MYI at fine, medium (med) and coarse spatial scales (object) as well as 120 and 240 m grid-cells. Bolded values are statistically significant ($p < 0.05$).

		FYI		**MYI**				**FYI**		**MYI**	
		Fine	Med	Fine	Med	Coarse		120 m	240 m	120 m	240 m
Min	Objects	**0.39**	0.36	**0.07**	0.21	0.27	Grid-cell	**0.30**	**0.34**	0.01	0.23
Max		**0.56**	**0.65**	0.41	**0.54**	**0.57**		**0.44**	**0.53**	0.11	0.13
Mean		**0.36**	**0.49**	0.20	0.20	0.23		**0.41**	**0.44**	0.07	0.07
Med		0.18	**0.26**	0.12	0.06	0.03		**0.34**	**0.38**	0.04	0.13
SD		**0.52**	**0.68**	0.40	**0.47**	**0.47**		**0.35**	**0.45**	0.05	0.07

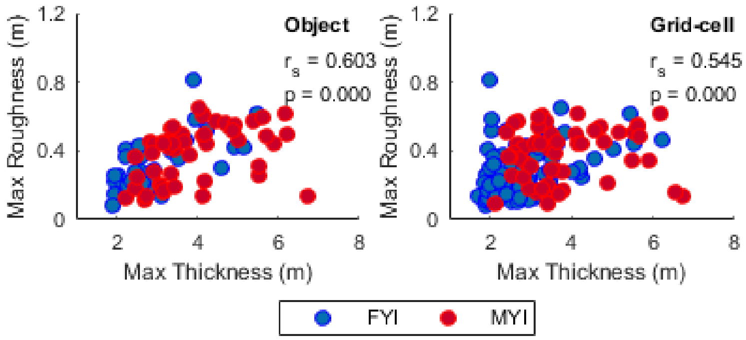

Figure 2.12 Scatter plots of maximum roughness as a function of maximum thickness at the medium scale using object (left) and 240 m grid-cell (right) aggregation approaches. Spearman correlation coefficients (r_s) and corresponding p-values are shown for pooled FYI and MYI data.

2.5 Discussion

Previous studies have shown that FYI is characterized by a higher spring f_p than MYI [7,11,13,34,35]. Our findings support these observations, with FYI exhibiting on average higher spring f_p of 0.43 compared to 0.29 for MYI. However, we show that certain regions of MYI become flooded, with spring f_p reaching up to 0.77. Winter sea ice thickness and surface roughness values and probability distributions are consistent with previous studies, showing FYI being thinner and smoother compared to MYI. Numerical models indicate that pre-melt surface roughness is strongly related to f_p, with f_p increasing more rapidly on a smoother ice than rougher ice [36]. Our results show that surface roughness is related to f_p for FYI, but we do not find a similar association for MYI. Previous work has suggested that thin and smooth ice would be favorable for high f_p during the melt season, and rough/thick ice would limit melt pond expansion and result in low f_p; however these relationships have not been quantified to date [11,37] . For logistical reasons the majority of previous melt pond evolution studies have been conducted on landfast FYI and drifting MYI. Our f_p observations show agreement with other landfast FYI studies and drifting FYI and MYI studies. Since our analyses are concerned with one snapshot of melt fraction, and not melt pond evolution through time, it is not necessary to account for ice mobility. However, when considering melt pond evolution, it is important to note that thermodynamic and dynamic processes of landfast ice differ from those of drifting ice. Landfast sea ice forms in areas of shallow bathymetry and is influenced by tides and nearshore currents [38]. Furthermore, it exhibits a fixed orientation with the respect to the sun and is influenced by dust and warm air from the nearby land [39].

Considering the role of different aggregation approaches for quantifying relationships, the benefit of OBIA is that it is rooted in real world features such as ice floes, thus providing physically meaningful extents for data aggregation and contextual information for the analyst. The hybrid approach aims to compromise between the extents of real world features and the footprint of the sensor, in cases where objects are being used to aggregate multi-sensor data. In this study, the extents of the objects were often much larger than the footprint of the thickness and roughness sensors, which means that the corresponding thickness and roughness measurements may not have been representative of certain regions of the object (Figure 2.5). The hybrid object approach yielded stronger associations between thickness and f_p for FYI and similar to slightly stronger relationships for MYI (Table 2.2). The stronger relationships between FYI thickness and f_p can be explained by spatial homogeneity of FYI ice floes in terms of thickness, roughness and the SAR backscatter used to delineate objects. Compared to MYI, FYI has a lower surface roughness, which allows it to have a low backscatter across large areas. By reducing the width of the object-based features into hybrid objects, analyses become more representative of the areas associated with the thickness and roughness measurements while retaining the across-track boundaries of individual ice floes.

We have been able to show that winter sea ice thickness and surface roughness are related to spring f_p on landfast sea ice in the CAA*;* however, it is possible that sensor limitations impacted the results. Laser altimeters do not penetrate through the snow cover to the snow/ice interface, therefore the sea ice thickness measurements obtained using the EM-bird are in actuality snow plus ice measurements. It is suggested that the accuracy of EM measurements over level ice is approximately ±0.15 m, whereas thickness of thick MYI ridges can be underestimated by as much as 24%. Areas of thick ice, such as ridges in an otherwise smooth FYI zone can be underestimated if they are proximal to areas of thin ice and occur with the footprint of the EM sensor. Unfortunately, it was not possible to obtain co-located *in situ* snow depth observations in our study area and due to the uncertainties associated with snow depth estimates in complex ice environments Operation IceBridge (OiB) and CryoVex data were not included in the analyses [40]. We were able to obtain *in situ* snow depth measurements, which were collected using a MagnaProbe near Eureka in the CAA between 8 and 15 April 2016 (Figure 2.2). 1792 and 1810 snow measurements were collected on FYI and MYI, respectively, with transects covering areas of approximately 0.4 km^2 each (~10 m spacing). Figure 2.13 shows that the mean snow depth on FYI is 16.6 cm compared to 42.5 cm on MYI. The variability in snow depth is also greater for MYI, with depths of up to 200 cm. In 2016, total October to May snowfall at an Environment Canada station in Cambridge Bay was approximately 45 cm compared to 65 cm at an Environment Canada station in Eureka. October to May *in situ* mean snow depths on landfast FYI measured 8.4 ± 4.2 cm (Cambridge Bay) and 17.6 ± 5.8 cm (Eureka) between 1960 and 2014 [41]. The nearest snow depth and weather station data available indicate that Victoria Strait will have less sea ice snow accumulation than Eureka. Further work or co-located snow depth and EM sea ice thickness measurements would be required to more fully assess the effect of snow depth on relationships with f_p.

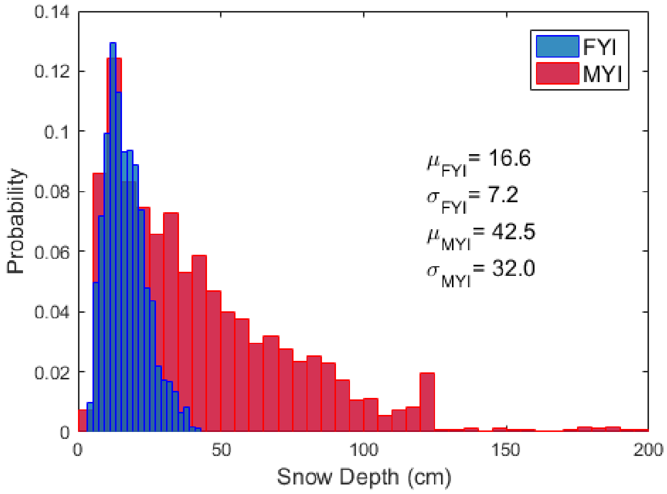

Figure 2.13 2016 snow depth distributions on FYI (blue) and MYI (red) near Eureka in the CAA. Mean (μ) and standard deviations (σ) are given by ice type. 1792 measurements snow depth measurements were collected on FYI and 1810 measurements on MYI.

The 2D laser scanner instrument operates in the near infrared part of the electromagnetic spectrum, which means that it does not penetrate through the snow cover and thus measures variations in snow topography. This could potentially lead to underestimation of surface roughness because the snow cover may have a dampening effect on the sea ice surface, particularly due to accumulation of snow in rough areas by wind redistribution. Snow sastrugi may also introduce erroneous surface roughness values that are not associated with the sea ice topography. Quantifying surface roughness in the natural environment remains a challenge, with the most widely used approach being the standard deviation of relative surface elevation;

however other statistical parameters such as skewness and kurtosis have been proposed [42]. Furthermore, roughness measurements are highly scale-dependent and large-scale variations in topography may introduce uniform and along flight line errors. Finally, it is often assumed that distribution of sea ice features such as ridges and leads is random. However, this assumption is often not valid because dominant orientations of features result from prevailing ocean and atmospheric currents. Thus, it is possible to under or over represent the distribution of extreme features, depending on the choice of flight direction [25].

Thermodynamic and dynamic processes are responsible for changes in sea ice thickness with FYI increasing above modal thickness as a result of ridging. Thus, surface roughness and ice thickness are expected to be closely related, particularly for thicker, more deformed FYI. This is supported by comparing the spatial distribution of high thickness and roughness values for FYI in the study area (Figure 2.3). Areas of high surface roughness (0.33–0.44 m) overlap with areas of thicker ice (2.7–3.1 m), as well as with areas of higher backscatter. A similar relationship can be seen for MYI. Quantitatively, we have shown that maximum thickness and maximum roughness have a stronger association for FYI ($r_s = 0.65$) than MYI ($r_s = 0.54$). With MYI being ice that survived one or more melt season, its surface roughness will be affected by melt, particularly by the presence of refrozen melt ponds from previous melt seasons. An area that includes a melt pond from a previous melt season and heavily deformed patch of ice may be associated with high surface roughness measurement. However, this high roughness value may correspond to a high f_p due to the presence of a relatively smooth patch of ice, which was previously occupied by a melt pond.

2.6 Conclusions

The primary goal of this study was to quantitatively link winter sea ice thickness and surface roughness to spring f_p in order to better understand how the ice evolves from winter to spring thermodynamic states and inform parameterizations of f_p in climate models. This was achieved by evaluating the utility of object-based image analysis, hybrid-object analysis, which takes into account the footprints of the thickness and roughness sensors, as well as the traditional grid-cell data aggregation approaches. It was found that winter sea ice thickness has a strong association with f_p for FYI ($r_s = -0.85$) and MYI ($r_s = -0.64$) using hybrid aggregation approach, as well as the object approach for FYI ($r_s = -0.75$) and MYI ($r_s = -0.60$). Weaker relationships were observed for MYI using the grid-cell approach ($r_s = -0.47$); however a similar relationship was detected for FYI ($r_s = -0.75$). This shows that winter sea ice thickness is related to spring f_p with thicker ice characterized by lower spring f_p and thin ice exhibiting a higher f_p during the melt season. These results provide a quantitative link between the two geophysical parameters and have important implications for understanding spring f_p evolution on Arctic sea ice. The stronger relationships observed using hybrid aggregation indicate that accounting for ice morphology and sensor footprints allows for more representative comparison between multisource datasets. A non-linear rational function OLS model shows that 47% of variability in combined FYI and MYI spring f_p can be explained by mean winter sea ice thickness using the hybrid-based aggregation approach indicating a potential for spring f_p prediction using winter sea ice thickness. FYI spring f_p is related to winter surface roughness, with a stronger relationship observed using the hybrid-based aggregation approach at the medium scale ($r_s = -0.63$). However, MYI f_p is not significantly correlated with surface roughness. Surface roughness can be defined for scales ranging from meters to kilometers, with footprint-scale uncertainties such as snow roughness and errors associated with sensor position during airborne measurement acquisition (yaw and pitch angles, and slant range distortion) exhibiting a stronger effect on the measurements than at larger spatial scales [26,40]. In order to minimize the influence of measurement uncertainty on surface roughness measurements we performed a moving average on the surface roughness data (~2400 m) and found stronger correlations between surface roughness and f_p for both FYI ($r_s = -0.84$) and MYI ($r_s = -0.34$). We propose that further work is conducted on assessing the effects of snow depth and snow redistribution features on sea ice surface roughness estimates.

Winter sea ice thickness and surface roughness are moderately correlated for FYI ($r_s = 0.65$) and MYI ($r_s = 0.54$) using the object aggregation approach. These relationships are lower in strength for FYI ($r_s = 0.53$) and are not present for MYI using the grid-cell data aggregation approach. This further supports the use of object-based aggregation for spatial statistical analyses.This study draws quantitative linkages between winter sea ice (snow plus ice) thickness and spring f_p at the macro scale, which can contribute to a body of work improving parametrizations of spring f_p in climate models. Further work includes contributing evaluations of the potential of winter sea ice thickness, in addition to sea ice roughness, as well as radar backscatter signatures to predict spring f_p using satellite sensors such as CryoSat-2, Sentinel-1 and others. It is important to be able to expand the analyses to larger spatial and temporal scales, which are necessary for initializing and validating regional climate models.

2.7 Acknowledgments

The research was conducted as part of the interdisciplinary Ice Covered Ecosystem-CAMbridge Bay Process Studies (ICE-CAMPS) project. Funding was provided by Marine Environmental Observation Prediction and Response Network (MEOPAR) and the National Sciences and Engineering Research Council of Canada (NSERC)—Discovery Grants Program. Additional support was provided by the Northern Scientific Training Program (NSTP).

2.8 Author Contributions

Sasha Nasonova prepared the datasets, conducted the quantitative analysis and drafted the manuscript. Randy Scharien conceived the study, processed and segmented the RADARSAT-2 imagery, provided expert interpretation of the data and results, and contributed extensive feedback on the manuscript. Christian Haas provided thickness and roughness data for the analysis as well expert interpretation and support. Stephen Howell conceived the study and provided the RADARSAT-2 and GeoEye-1 datasets.

2.9 References

1. Rigor, I. G.; Wallace, J. M. Variations in the age of Arctic sea-ice and summer sea-ice extent. *Geophys. Res. Lett.* **2004**, *31*, 2–5, doi:10.1029/2004GL019492.
2. Kwok, R.; Cunningham, G. F.; Wensnahan, M.; Rigor, I.; Zwally, H. J.; Yi, D. Thinning and volume loss of the Arctic Ocean sea ice cover: 2003–2008. *J. Geophys. Res.* **2009**, *114*, C07005, doi:10.1029/2009JC005312.
3. Meier, W. N. Actic sea ice in tranformation: A review of recent observed changes and impacts on biology. *Rev. Geophys.* **2015**, *53*, 1–33, doi:10.1002/2013RG000431.
4. Swart, N. C.; Fyfe, J. C.; Hawkins, E.; Kay, J. E.; Jahn, A. Influence of internal variability on Arctic sea-ice trends. *Nat. Clim. Chang.* **2015**, *5*, 86–89, doi:10.1038/nclimate2483.
5. Hanesiak, J. M.; Barber, D. G.; De Abreu, R.A.; Yackel, J. J. Local and regional albedo

observations of Arctic first-year sea ice during melt ponding. *J. Geophys. Res.* **2001**, *106*, 1005, doi:10.1029/1999JC000068.

6. Perovich, D. K.; Polashenski, C. Albedo evolution of seasonal Arctic sea ice. *Geophys. Res. Lett.* **2012**, *39*, 1–6, doi:10.1029/2012GL051432.
7. Perovich, D. K.; Grenfell, T. C.; Light, B.; Hobbs, P. V. Seasonal evolution of the albedo of multiyear Arctic sea ice. *J. Geophys. Res.* **2002**, *107*, 8044, doi:10.1029/2000JC000438.
8. Arrigo, K. R.; Perovich, D. K.; Pickart, R. S.; Brown, Z. W.; van Dijken, G. L.; Lowry, K. E.; Mills, M. M.; Palmer, M. A.; Balch, W. M.; Bahr, F.; Bates, N. R.; Benitez-Nelson, C.; Bowler, B.; Brownlee, E.; Ehn, J. K.; Frey, K.; Garley, R.; Laney, S. R.; Lubelczyk, L.; Mathis, J.; Matsuoka, A.; Mitchell, B. G.; Moore, G. W. K.; Ortega-Retuerta, E.; Pal, S.; Polashenski, C. M.; Reynolds, R. A.; Schieber, B.; Sosik, H. M.; Stephens, M.; Swift, J. H. Massive Phytoplankton Blooms Under Arctic Sea Ice. *Science.* **2012**, *336*, 1408–1408, doi:10.1126/science.1215065.
9. Pućko, M.; Stern, G. A.; Macdonald, R. W.; Jantunen, L. M.; Bidleman, T. F.; Wong, F.; Barber, D. G.; Rysgaard, S. The delivery of organic contaminants to the Arctic food web: Why sea ice matters. *Sci. Total Environ.* **2015**, *506–507*, 444–452, doi:10.1016/j.scitotenv.2014.11.040.
10. Schröder, D.; Feltham, D. L.; Flocco, D.; Tsamados, M. September Arctic sea-ice minimum predicted by spring melt-pond fraction. *Nat. Clim. Chang.* **2014**, *4*, 353–357, doi:10.1038/nclimate2203.
11. Eicken, H.; Grenfell, T. C.; Perovich, D. K.; Richeter-Menge, J. A.; Frey, K. Hydraulic controls of summer Arctic pack ice albedo. *J. Geophys. Res. C Ocean.* **2004**, *109*, 1–13, doi:10.1029/2003JC001989.
12. Eicken, H.; Krouse, H. R.; Kadko, D.; Perovich, D. K. Tracer studies of pathways and rates of meltwater transport through Arctic summer sea ice. **2002**, *107*, 1–20, doi:10.1029/2000JC000583.
13. Polashenski, C.; Perovich, D. K.; Courville, Z. The mechanisms of sea ice melt pond formation and evolution. *J. Geophys. Res.* **2012**, *117*, 1–23, doi:10.1029/2011JC007231.

14. Rösel, a.; Kaleschke, L.; Birnbaum, G. Melt ponds on Arctic sea ice determined from MODIS satellite data using an artificial neural network. *Cryosph.* **2012**, *6*, 431–446, doi:10.5194/tc-6-431-2012.

15. Scharien, R. K.; Hochheim, K.; Landy, J.; Barber, D. G. First-year sea ice melt pond fraction estimation from dual-polarisation C-band SAR – Part 2: Scaling *in situ* to Radarsat-2. *Cryosph.* **2014**, *8*, 2163–2176, doi:10.5194/tc-8-2163-2014.

16. Han, H.; Im, J.; Kim, M.; Sim, S.; Kim, J.; Kim, D. J.; Kang, S. H. Retrieval of melt ponds on arctic multiyear sea ice in summer from TerraSAR-X dual-polarization data using machine learning approaches: A case study in the Chukchi Sea with mid-incidence angle data. *Remote Sens.* **2016**, *8*, doi:10.3390/rs8010057.

17. Kettig, R. L.; Landgrebe, D. A. Classification of Multispectral Image Data by Extraction and Classification of Homogeneous Objects Classification of Multispectral Image Data by Extraction and Classification of Homogeneous Objects. *IEEE Trans. Geosci. Electron.* **1976**, *GE-14*, 19–26.

18. Blaschke, T. Object based image analysis for remote sensing. *ISPRS J. Photogramm. Remote Sens.* **2010**, *65*, 2–16, doi:10.1016/j.isprsjprs.2009.06.004.

19. Hay, G.; Marceau, D.; Dube, P.; Bouchard, A. A Multiscale Framework for Landscape Analysis : Object-specific analysis and upscaling. *Landscape* **2001**, *16*, 471–490.

20. Mazur, A. K.; Wåhlin, A. K.; Krężel, A. An object-based SAR image iceberg detection algorithm applied to the Amundsen Sea. *Remote Sens. Environ.* **2017**, *189*, 67–83, doi:10.1016/j.rse.2016.11.013.

21. Canadian Ice Serice. *Sea Ice Climatic Atlas: Northern Canadian Water 1981-2010*; Ottawa, 2007;

22. Melling, H. Sea ice of the northern Canadian Arctic Archipelago. *J. Geophys. Res. Ocean.* **2002**, *107*, 3181, doi:10.1029/2001JC001102.

23. Howell, S. E. L.; Wohlleben, T.; Dabboor, M.; Derksen, C.; Komarov, A.; Pizzolato, L. Recent changes in the exchange of sea ice between the Arctic Ocean and the Canadian Arctic Archipelago. *J. Geophys. Res. Ocean.* **2013**, *118*, 3595–3607, doi:10.1002/jgrc.20265.

24. Haas, C.; Howell, S. E. L. Ice thickness in the Northwest Passage. *Geophys. Res. Lett.* **2015**, 1–8, doi:10.1002/2015GL065704.

25. Haas, C.; Lobach, J.; Hendricks, S.; Rabenstein, L.; Pfaffling, A. Helicopter-borne measurements of sea ice thickness , using a small and lightweight , digital EM system. *J. Appl. Geophys.* **2009**, *67*, 234–241, doi:10.1016/j.jappgeo.2008.05.005.

26. Beckers, J. F.; Renner, A. H. H.; Spreen, G.; Gerland, S.; Haas, C. Sea-ice surface roughness estimates from airborne laser scanner and laser altimeter observations in Fram Strait and north of Svalbard. *Ann. Glaciol.* **2015**, *56*, 235–244, doi:10.3189/2015AoG69A717.

27. Sarp, G. Spectral and spatial quality analysis of pan-sharpening algorithms: A case study in Istanbul. *Eur. J. Remote Sens.* **2014**, *47*, 19–28, doi:10.5721/EuJRS20144702.

28. Flanders, D.; Hall-Beyer, M.; Pereverzoff, J. Preliminary evaluation of eCognition object-based software for cut block delineation and feature extraction. *Can. J. Remote Sens.* **2003**, *29*, 441–452, doi:10.5589/m03-006.

29. Bunting, P.; Lucas, R. The delineation of tree crowns in Australian mixed species forests using hyperspectral Compact Airborne Spectrographic Imager (CASI) data. *Remote Sens. Environ.* **2006**, *101*, 230–248, doi:10.1016/j.rse.2005.12.015.

30. Duro, D. C.; Franklin, S. E.; Dubé , M. G. A comparison of pixel-based and object-based image analysis with selected machine learning algorithms for the classification of agricultural landscapes using SPOT-5 HRG imagery. *Remote Sens. Environ.* **2012**, *118*, 259–272, doi:10.1016/j.rse.2011.11.020.

31. Robson, M.; Secker, J.; Vachon, P. W. Evaluation of eCognition for assisted target detection and recognition in SAR imagery. *Int. Geosci. Remote Sens. Symp.* **2006**, 145–148, doi:10.1109/IGARSS.2006.42.

32. Scharien, R. K.; Yackel, J. J.; Granskog, M. A.; Else, B. Coincident high resolution optical-SAR image analysis for surface albedo estimation of first-year sea ice during summer melt. *Remote Sens. Environ.* **2007**, *111*, 160–171, doi:10.1016/j.rse.2006.10.025.

33. Benz, U. C.; Hofmann, P.; Willhauck, G.; Lingenfelder, I.; Heynen, M. Multi-resolution, object-oriented fuzzy analysis of remote sensing data for GIS-ready information. *ISPRS J.*

Photogramm. Remote Sens. **2004**, *58*, 239–258, doi:10.1016/j.isprsjprs.2003.10.002.

34. Fetterer, F. M.; Untersteiner, N. Observations of melt ponds on Arctic sea ice. *J. Geophys. Res.* **2000**, *103*.

35. Webster, M. A.; Rigor, I. G.; Perovich, D. K.; Richeter-Menge, J. A.; Polashenski, C. M.; Light, B. Seasonal evolution of melt ponds on Arctic sea ice. *J. Geophys. Res.* **2015**, 1–15, doi:10.1002/2015JC011030.

36. Landy, J. C.; Ehn, J. K.; Barber, D. G. Albedo feedback enhanced by smoother Arctic sea ice. *Geophys. Res. Lett.* **2015**, *42*, 10714–10720, doi:10.1002/2015GL066712.

37. Perovich, D. K. *The optical properties of sea ice*; Arlington, Virginia, 1996;

38. Mahoney, A.; Eicken, H.; Gaylord, A. G.; Shapiro, L. Alaska landfast sea ice : Links with bathymetry and atmospheric circulation. *J. Geophys. Res.* **2007**, *112*, doi:10.1029/2006JC003559.

39. Grenfell, T. C.; Perovich, D. K. Seasonal and spatial evolution of albedo in a snow-ice-land-ocean environment. *J. Geophys. Res.* **2004**, *109*, doi:10.1029/2003JC001866.

40. King, J.; Howell, S. E. L.; Derksen, C.; Rutter, N.; Toose, P.; Beckers, J. F.; Haas, C.; Kurtz, N.; Richeter-Menge, J. A. Evaluation of Operation IceBridge quick-look snow depth estimates on sea ice. *Geophys. Res. Lett.* **2015**, *42*, 9302–9310, doi:10.1002/2015GL066389.

41. Howell, S. E. L.; Laliberté, F.; Kwok, R.; Derksen, C.; King, J. Landfast ice thickness in the Canadian Arctic Archipelago from Observations and Models. *Cryosph. Discuss.* **2016**, 1–39, doi:10.5194/tc-2016-71.

42. Bogsjö, K.; Podgórski, K.; Rychlik, I. Models for road surface roughness. *Veh. Syst. Dyn.* **2012**, *50*, 725–747, doi:10.1080/00423114.2011.637566.

Chapter 3 Optimal compact polarimetric parameters and texture features for discriminating major sea ice types during winter and advanced melt

C-band synthetic aperture radar (SAR) has been widely used for sea ice monitoring and operational activities. Dual-polarimetric SAR is the main data source for government, industry and scientific applications. The RADARSAT Constellation Mission (RCM), with its anticipated launch in 2018 will provide hybrid compact polarimetric (CP) data offering near-polarimetric capabilities at large image acquisition widths suitable for achieving operational and scientific objectives in the Arctic. Although, C-band SAR has been effective for sea ice monitoring, it has been difficult to implement during the spring and summer when the sea ice cover is dominated by melt ponds. The ability of simulated CP RCM parameters to distinguish between ice types during *winter* and *advanced melt* was assessed through Kolmogorov-Smirnov statistical separability analyses and Support Vector Machine supervised classifications. It was found that the steep incidence angle simulated RCM CP parameters provide improved ice type separability during the *advanced melt* period compared to shallow incidence angles. With respect to classification, an overall accuracy of 77.06% was found for a scene comprising first-year ice (FYI) and multiyear ice (MYI) types, and a higher overall accuracy of 85.91% was achieved by including grey level co-occurrence matrix (GLCM) parameters in the classification. A backscatter inversion between FYI and MYI allows for discrimination during *advanced melt*, and is attributed to (1) reduced penetration of C-band SAR during ponding which masks volume scattering from MYI, (2) high Bragg scattering from wind roughened melt ponds on FYI which are large, interconnected, and more dominant compared to MYI, (3) lower losses of backscatter intensity to specular reflection at steep incidence angles, thus allowing for retention of high intensity backscatter from wind roughened melt ponds on FYI.

Keywords: compact polarimetry; synthetic aperture radar; Arctic; sea ice; *advanced melt*

3.1 Introduction

Satellite synthetic aperture radar (SAR) is an active microwave remote sensing technique which allows for acquisition of high resolution images in all-weather conditions, independently of sunlight and cloud cover, with most systems attempting to maximize either spatial resolution, polarimetric information or swath width. Currently, the majority of sea ice observation and operational activities rely on single- (HH or VV) or dual-polarized (HH, HV or VV, VH) SAR imagery. Quad-polarized SAR provides all four combinations of backscatter and relative phase information (HH, HV, VH, VV) which is more representative of the underlying geophysics of sea ice [1]. Unfortunately, polarimetric capabilities and high spatial resolution of quad-polarized SAR sensors, such as RADARSAT-2, are possible only at the expense of aerial coverage, with image swath widths of less than 50 km. Compact polarimetric (CP) SAR offers a compromise between the fully polarimetric capabilities of quad-polarized systems and large image swath widths of standard single- and dual-polarized SARs. The main types of CP configurations are: π/4 mode, end-to-end circular and hybrid. CP systems in π/4 mode transmit a linearly polarized wave at π/4 radians with respect to H and V orientations, while coherently receiving the resulting H and V backscatter components [2]. This configuration is said to be comparable to quad-polarized SAR if reflection symmetry is assumed [2]. As a result, polarimetric decomposition analyses are most effective in scenes dominated by scatterers with horizontal or vertical orientations [3]. For Earth Observation (EO) applications, often, the objective is to ascertain the scattering mechanisms of the landscape in question and subsequently conduct image classification. Therefore, *a priori* assumption of target scatterer orientation is not appropriate [4]. End-to-end circular CP both transmits and receives coherent dual-polarized circular waves (right hand circular, and left hand circular). This type of architecture retains the relative phase of transmitted and received waves which makes it possible to derive Stokes parameters required for polarimetric decompositions. End-to-end circular CP systems produce good results but are difficult to implement and not usually considered for EO applications [4].

As a compromise between the π/4 mode and end-to-end circular CP systems, hybrid CP was developed [4,5]. The hybrid approach is to transmit a circularly polarized wave and receive orthogonal coherent linear polarizations (circular transmit, H and V receive). Hybrid CP is an attractive alternative to quad-polarized systems because it provides a 2 x 2 covariance matrix of the backscattering field which can be transformed into Stokes vectors [6]. Furthermore, the relative phase information of the received polarizations allows for the generation of polarimetric decompositions similar to those derived from quad-polarized data. It is important to note that the information content provided by quad-polarized SAR (4 x 4 covariance matrix) cannot be replaced by any CP system; however, within operational constraints, hybrid CP offers a viable alternative by providing comparable polarimetric information at large swath widths.

To support maritime surveillance, disaster management and ecosystem monitoring, the Canadian Space Agency (CSA) in partnership with MacDonald Dettwiler and Associates (MDA) will be launching the RADARSAT Constellation Mission (RCM). It will be equipped with C-band hybrid CP SAR aboard three satellites and is anticipated that launch will take place in 2018. For maritime applications it is expected that the Medium Resolution 50 m (MR50) mode will be the primary acquisition mode [7]. It will ensure data continuity with RADARSAT-2 ScanSAR currently used by the Canadian Ice Service (CIS), by providing a product with a 50 m resolution (20 m pixel size), a noise floor of -22 dB, with four looks and a 350 km image swath [8]. RCM will be capable of approximately 10 different image modes, from Low Resolution 100 m mode with an image swath width of 500 km, to Spotlight mode with a resolution of 3 m and a narrow swath width of 5 km. Quad-polarization data will also be available with a 9 m resolution and -24 dB noise floor [7].

In order to analyze the relationships between physical, thermodynamic and microwave scattering properties of the ocean-sea ice-atmosphere (OSA) system, the following unique thermodynamic regimes have been proposed*: freeze-up, winter, early melt, melt onset and advanced melt* [9]. *Freeze-up* occurs in the fall, when solar radiation decreases and sea ice begins to form on the ocean surface. Whereas, the *winter* period is characterized by the total absence of sunlight with a strong temperature gradient between the atmosphere and the ocean below. During this time, the sea ice surface is dominated by dry snow. Due to the lack of liquid water in the snow pack, C-band SAR is often able to penetrate through the snow and provide information on sea ice structural characteristics. However, on first-year sea ice (FYI), the snow cover may be sufficiently saline and inhibit the ability of C-band microwaves to penetrate to the sea ice [10]. Generally, FYI is dominated by surface scattering and exhibits lower intensity backscatter than multiyear sea ice (MYI), which shows a strong volume scattering signature from the low salinity and air bubble rich upper layer. Upon the return of solar insolation and above freezing temperatures to the Polar Regions, snow begins to increase in volumetric liquid content, thus decreasing penetration depth of C-band SAR [11]. During *early melt* a portion of the upper snow volume reaches or exceeds 0°C for a part of the day. *Melt onset* occurs when the snow pack reaches 2% liquid water content throughout the whole day, which masks the backscatter signature of the sea ice. *Advanced melt* occurs once melt ponds appear on the ice surface and is a highly dynamic and temporally variable period of sea ice evolution. Melt ponds rapidly decrease the albedo of the sea ice cover, percolate through the ice leading to desalination, enhance light and contaminant transfer to the upper ocean layers, and play an important role in energy exchanges across the OSA [12–14].

Relationships between sea ice physical properties and SAR backscatter have been investigated since the late 1980s and a good understanding of these relationships exist for the cold season [9]. Although significant progress has been made with regards to understanding sea ice backscatter evolution during the melt season, challenges associated with the presence of wet snow in the early stages of melt, and melt ponds during the *advance melt* period remain [15–17]. Wind interactions with melt pond surfaces, diurnal variations associated with expansions and drainage of melt ponds, as well as formations of ice lenses on pond surfaces inhibit our understanding of microwave scattering during *advanced melt*. The ability to distinguish between FYI and MYI during *advanced melt* is of interest to the scientific community because FYI is typically characterized by a higher melt pond fraction (aerial extent of melt ponds) than MYI, leading to a lower surface albedo [13,12,18–20]. Furthermore, it has been shown that melt pond fraction is a good predictor of minimum sea ice extent, and thus the inclusion of melt pond fraction in sea ice forecast models may substantially increase their skill [21,22]. From the operations perspective, MYI can be very hazardous to ships because it is typically significantly thicker and harder than FYI [23]. Since shipping activities in the Arctic occur mostly during the summer months, and MYI causes the most severe risk of damage to ships, it is important to be able to detect the locations of MYI floes and reduce marine navigation incidents [24].

To date, sea ice studies using simulated RCM parameters have focused on assessing ice type separability for a large number of scenes and for mainly pre-melt conditions. These studies show that it is possible to distinguish between ice and open water [25], as well as smooth FYI, rough FYI and open water [6]. Furthermore, discrimination between FYI and MYI, as well as open water and either FYI or MYI has been demonstrated during *advanced melt* [26], though further investigation particularly with respect to dominant scattering mechanisms is warranted. In anticipation of the upcoming launch of the RCM, this paper aims to: (1) determine the optimal RCM parameters for major ice type separability during *advanced melt*, and (2) assess the utility of texture features derived from RCM parameters for enhanced separability. Results from (1) and (2) will be assessed in the context of scattering mechanisms and the influence of environmental and systems parameters.

3.2 Study Area and Data

The study area is located in the Victoria Strait and M'Clintock Channel waterways of the southern Canadian Arctic Archipelago (CAA) near Cambridge Bay, Nunavut (Figure 3.1). These areas typically comprise a combination of FYI and MYI which can remain landfast for up to 8 months of the year [27]. Landfast ice regions allow for a unique environment for establishing relationships between *winter* and *advanced melt* sea ice conditions without accounting for drifting sea ice.

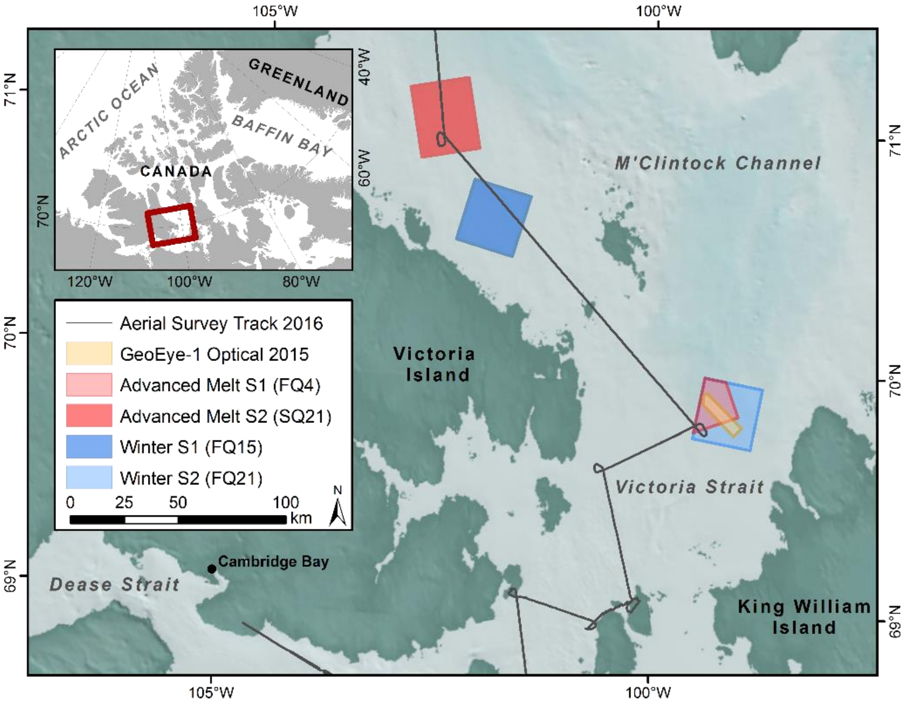

Figure 3.1 Map showing study area location in Victoria Strait and M’Clintock Channel near Cambridge Bay, NU, in the CAA. 2 *advanced melt* (Advanced Melt S1 and Advanced Melt S2) and 2 *winter* (Winter S1 and Winter S2) RADARSAT-2 scenes were acquired, as well as auxillary data including high resolution GeoEye-1 optical imagery of melt pond covered sea ice from 2015 and aerial photography of melt pond covered sea ice in 2016.

Detailed information on the four RADARSAT-2 scenes used in this study are shown in Table 3.1. Two *winter* images were collected in April 2015 at varied incidence angles. The first scene, Winter S1 was collected at mid-range (34.5-36.1°); the second, Winter S2, was collected at shallow range (40.2-41.6°). Two *advanced melt* scenes were acquired over melt pond covered sea ice in June 2015 (Advanced Melt S1) and June 2016 (Advanced Melt S2). These data were collected at steep (22.3-24.2°) and shallow (39.6-42.2°) incidence angles, respectively. Both Winter S1 and Winter S2 were collected in Fine Quad (FQ) mode and covered areas of 787.2 km^2 and 780.1 km^2. Advanced Melt S1 was collected in FQ mode and covered an area of 312.2 km^2, whereas Advanced Melt S2 was collected in Standard Quad (SQ) mode with a greater aerial coverage of 902.4 km^2. In order to establish links between *advanced melt* backscatter behavior and sea ice surface conditions, in a region not practically accessible during *advanced melt,* a high resolution GeoEye-1 image overlapping a portion of Advanced Melt S1 was obtained on June

25, 2015. An airborne aerial photography survey was flown over the region on June 21st, 2016, with the data overlapping a portion of Advanced Melt S2.

Table 3.1 Quad-polarimetric RADARSAT-2 scenes used in this study.

Scene	Date	Time (UTC)	Pass	Beam	Incidence Angle (°)	Area (km^2)
Winter S1	29-04-2015	13:33	Descending	FQ15	34.5-36.1	787.2
Winter S2	23-04-2015	13:08	Descending	FQ21	40.2-41.6	780.1
Advanced Melt S1	26-06-2015	23:35	Ascending	FQ4	22.3-24.2	312.2
Advanced Melt S2	23-06-2016	0:17	Ascending	SQ21	39.6-42.2	902.4

3.3 Methods

3.3.1 RCM Parameter Simulation

The RCM Compact Polarimetry Simulator Version 3.1 was used to simulate linear and CP parameters using quad-polarimetric RADARSAT-2 imagery as inputs [6]. A list of all the compact polarimetric parameters and associated equations are given in Appendix 4.1. The data were simulated in the MR50 mode because it is expected that this mode will be used for ice monitoring by the CIS [7,8]. MR50 will have a spatial resolution of 50 m resolution (range and azimuth), 4 looks, a noise equivalent sigma zero (NESZ) of -22 dB with a swath width of 350 km. The RCM simulator undergoes the following process to transform quad-polarimetric RADARSAT-2 data into linear and CP parameters. First, the RADARSAT-2 single look complex product is calibrated using Sigma Naught (σ^0) calibration and the calibrated product is stored as a 3 x 3 covariance matrix. Then, the 3 x 3 covariance matrix is downsampled to create a 2 x 2 covariance matrix with a spatial resolution of 50 m. From the 2 x 2 covariance matrix, linear configurations ($\sigma^0_{HH,}$ $\sigma^0_{HV,}$ σ^0_{VV}) and Stokes vectors (S_0, S_1, S_2, S_3) are generated and random noise is added to simulate the higher noise floor of the MR50 mode. A Sigma Lee speckle filter (7 x 7 window; 5 x 5 target window) is applied to Stokes components to estimate decomposition parameters; is also applied to the linear parameters for consistency. Finally, the parameters are georectified to the local WGS 1984/UTM projection with a 20 m pixel spacing [26]. Linear parameters will not available in MR50 mode.

3.3.2 Ice Type Separability and Classification

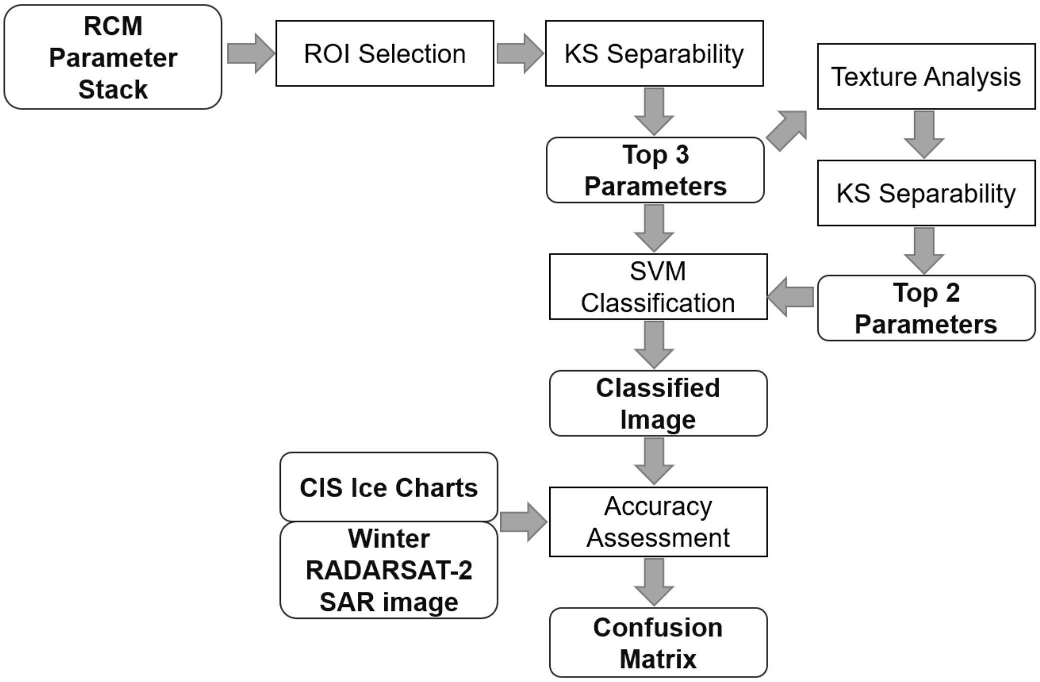

Figure 3.2 Flow chart showing statistical ice type separability and classification analyses of RADARSAT Constellation Mission (RCM) parameters.

Georectified RCM parameters were used in the subsequent analyses as outlined in Figure 3.2. First, regions of interest (ROI) corresponding to areas of homogeneous FYI, deformed FYI (DFYI) and MYI were isolated within each RCM parameter stack, using visual interpretation of collocated high resolution *winter* RADARSAT-2 imagery and ice chart data provided by the CIS. These subsets were used to conduct a two-sample Kolmogorov-Smirnov (KS) test in order to assess the statistical separability between ice type combinations (FYI/MYI, FYI/DFYI, MYI/DFYI). The KS test is a nonparametric hypothesis test which measures the maximum absolute distance between cumulative distribution functions of two populations. This type of test is valuable because it does not assume normality, nor is it affected by data transformations (such as conversions from power to dB), and it provides a measure of separability between 0 and 1. Three parameters that showed the highest separability between ice type combinations were chosen as inputs for a supervised Support Vector Machine (SVM) classification and subsequent texture analyses.

Grey level co-occurrence matrix (GLCM) derived texture features were chosen because they have been shown to be effective for enhancing ice type separability (Clausi, 2002; Liu et al., 2015). GLCM texture features are calculated by varying a number of parameters including window size, quantizer type (probabilistic or even distance), quantization levels (G), displacement (δ) and orientation (0, 45, 90 and 135°). A window size of 9 x 9 was selected, as well as a δ of 2, with a probabilistic quantizer and a G of 64. The probabilistic quantizer was chosen because it is less sensitive to outliers. The following ten GLCM texture features were calculated for each of the top three RCM CP parameters by ice type combination: Contrast, Dissimilarity, Homogeneity, Angular Second Moment, Energy, Maximum Probability, Entropy, GLCM Mean, GLCM Variance and GLCM Correlation (Table 3.2). The ability of GLCM texture features to improve ice type separability and subsequent classification was assessed using the KS test. For example, for Winter S2 which comprised of FYI and MYI, the top three RCM CP parameters with the highest KS distances were chosen. Then, each of the three parameters were used to calculate the ten GLCM texture features, for a total of thirty images. The KS test was used to calculate ice type separability for each of the thirty possible GLCM images and averaged for each of the ten GLCM texture features. The top two GLCM texture features with consistently improved ice type separability were used in the subsequent SVM classification.

Table 3.2 Descriptions of GLCM texture features.

Parameter	Abbreviation	Description
Contrast	CON	Contrast group, measure of variations in local intensity. Also known as Inertia.
Dissimilarity	DIS	Contrast group, a measure of smoothness.
Homogeneity	HOM	Contrast group, also known as Uniformity.
Angular Second Moment	ASM	Orderliness group, measure of homogeneity. Square-root of ASM.
Energy	ENE	Also known as Uniformity, detects disorder.
Maximum Probability	MAX	Orderliness group, a homogeneity statistic.
Entropy	ENT	Orderliness group, measure of complexity. Homogeneous scenes exhibit a low ENT, and inhomogeneous scenes a high ENT.
GLCM Mean	GLM	Statistics group, the probability that two pixels are neighbours.
GLCM Variance	GLV	Statistics Group. A high variance is associated with values that highly differ from the mean.
GLCM Correlation	GLC	Statistics group, a measure of linear dependence between neighbouring pixels.

SVM is an effective supervised classification method for noisy data as it is able to model complex non-linear boundaries between classes. The SVM algorithm is highly dependent on the kernel function chosen, with a variety of kernel function types available including: linear, polynomial, radial basis function and sigmoid. It has been shown that that the sigmoid and polynomial kernels do not provide significantly improved classification results and are more computationally intensive [30]. The penalty parameter, along with the type of kernel function chosen define the plane used to separate between classes. A high penalty parameter will require that as much of the training data as possible is divided by the plane. Based on Brisco et al. (2013) different penalty parameters were tested and it was observed that the variations in the penalty parameter had little to no influence on the classification accuracy, thus a moderate value of 100 was chosen [31]. Finally, a probability threshold of 0 was chosen because it leads to all pixels within a scene being assigned a class. An analysis on the effect of probability thresholds on classification accuracies merits further investigation, as SAR imagery often contains unusually high and low backscatter values. Furthermore, in operational applications it is necessary to establish the presence (target detection) of certain ice features such as MYI floes and highly deformed FYI, consequently it may not be necessary to classify every pixel in the scene.

Training datasets for the SVM classifications were compiled through visual interpretation of collocated *winter* RADARSAT-2 imagery and CIS ice chart data. Polygons were manually drawn around randomly generated points and used as ROIs to create a database consisting of locations of homogeneous ice type samples. Each scene was classified twice: (1) using 3 RCM parameters that showed the highest separability using the KS test and, (2) using 3 RCM parameters and their 2 corresponding GLCM texture parameters which showed the highest separability between ice types (nine in total). Confusion matrices were calculated to assess the classification accuracies by ice type, along with overall accuracies and Kappa coefficients. Like the training data, accuracy assessment ROIs representative of FYI, MYI and DFYI were acquired using the collocated *winter* RADARSAT-2 imagery and CIS ice charts**.** It is worth noting that the *winter* RADARSAT-2 imagery was of higher spatial resolution than the simulated MR50 mode RCM parameters, hence care was taken to extract areas of interest away from edges of ice floes and ridges. The number of polygons and pixels used to train the classifier are shown in Table 3.3.

Table 3.3 Training and validation data used for supervised SVM classifications of *winter* and *advanced melt* RCM scenes. The total number of pixels, and the number of polygons in brackets, is shown. There was no DFYI in Winter S2 and Advanced Melt S1.

	Training Samples			**Validation Samples**		
Image	FYI	DFYI	MYI	FYI	DFYI	MYI
Winter S1	2075 (30)	2409 (43)	2051 (51)	1555 (15)	2578 (27)	3174 (33)
Winter S2	2428 (37)	-	2512 (50)	1479 (22)	-	1553 (28)
Advanced Melt S1	2075 (20)	-	2277 (36)	2204 (21)	-	2856 (30)
Advanced Melt S2	2467 (25)	2571 (29)	2877 (13)	6649 (20)	3873 (35)	4686 (13)

To aid discussion on scattering mechanisms quad-polarimetric *winter* RADARSAT-2 imagery was used to generate Freeman-Durden polarimetric decompositions which model the covariance matrix as a combination of three scattering mechanisms: surface, volume and double-bounce. The Freeman-Durden decomposition parameters can be used to create a RGB composite with the red corresponding to double-bounce scattering, green associated with volume scattering and blue showing backscatter associated with surface scattering [32]. Freeman-Durden decompositions were obtained by applying a polarimetric Lee Sigma speckle filter with a sigma of 0.9, a 9 x 9 sliding window and a target window of 3 x 3, then calculating the Freeman-Durden polarimetric decomposition (5 x 5 window size).

3.4 Results and Discussion

3.4.1 Ice Type Separability

3.4.1.1 Winter

Table 3.4 shows KS distances which define separability between major types for Winter S1 (FQ15) and Winter S2 (FQ21) RCM parameters. KS distances represent separability between FYI and MYI (FYI/MYI), FYI and DFYI (FYI/DFYI) and, DFYI and MYI (DFYI/MYI) for Winter S1, whereas for Winter S2 KS distances were calculated for the FYI/MYI ice type combination only. Winter S1 generally exhibited higher discrimination ability for FYI/MYI than Winter S2. The top three Winter S1 parameters for FYI/MYI discrimination were σ^0_{RR}, H_i and S_0 with a KS separability of 0.99. For Winter S2, H_i, S_0 and σ^0_{VV} showed highest separability for FYI/MYI with 0.96, 0.96 and 0.94, respectively. The top three Winter S2 parameters for FYI/DFYI and MYI/DFYI discrimination were σ^0_{RR}, $CPSeaIce_{Depol}$ and $m\chi v$. Improved discrimination ability was observed for FYI/DFYI than for MYI/DFYI for all three parameters, with a KS separability of 0.97 and 0.78 for FYI/DFYI and MYI/DFYI using σ^0_{RR}. Similarly, CPSeaIce$_{Depol}$ and mχv showed a KS separability of 0.96 for FYI/DFYI, which decreased to 0.76 for mχv and 0.75 for CPSeaIce$_{Depol}$ for MYI/DFYI. The histograms of the three parameters with the highest discriminability of FYI and MYI are presented in Figure 3.3**.** As expected, FYI is characterized by lower backscatter than DFYI and MYI.

Generally, σ^0_{RR}, σ^0_{RL}, σ^0_{RH}, σ^0_{RV} and their linear counterparts σ^0_{HH}, σ^0_{HV} and σ^0_{VV} showed high separability for FYI/MYI and FYI/DFYI (Table 3.4). Though, a decrease in separability was observed for DFYI/MYI in Winter S1. Similarly, S_0, mχv and H_i performed well for discriminating between FYI and MYI as well as FYI and DFYI, with a decrease in separability for DFYI/MYI. All three parameters of the CPSeaIce composite showed high ice type discrimination ability. Conversely, $\sigma^0_{RV/RH}$, delta, 1-m, Conformity, ρRVRH and μ_c consistently exhibited low separability between ice types (KS <0.4). H_p, S_1 and α-s also showed low discrimination ability (KS <0.5). Finally, co- and cross-polarization ratios of linear backscatter parameters ($\sigma^0_{VV/HH}$, $\sigma^0_{HV/HH}$, $\sigma^0_{HV/VV}$) yielded poor separability between ice types for Winter S1 (KS < 0.4) and marginally higher separability for Winter S2 (Table 3.4). In general, these results are consistent with those found by Geldsetzer et al. (2015) [26]. Linear backscatter parameters will not available in MR50 and were not used in subsequent texture and classification analyses.

Table 3.4 Winter S1 and Winter S2 KS distances (0 to 1) for major ice type combinations. Bolded values correspond with statistically significant separability (p<0.01). Cell shading visually emphasizes discrimination ability of each RCM parameter, with high separability corresponding to light shading and low separability to dark shading. The top three most separable CP parameters which were used in the subsequent GLCM calculation are denoted with an asterisk (*).

	Winter S1			**Winter S2**
Parameter	FYI/MYI	FYI/DFYI	DFYI/MYI	FYI/MYI
σ^0_{RH}	**0.99**	**0.90**	**0.64**	**0.92**
σ^0_{RV}	**0.98**	**0.91**	**0.67**	**0.93**
σ^0_{RR}	**0.99***	**0.97***	**0.78***	**0.93**
σ^0_{RL}	**0.98**	**0.91**	**0.62**	**0.93**
$\sigma^0_{RV/RH}$	**0.12**	**0.11**	**0.06**	**0.15**
δ	**0.24**	**0.09**	**0.16**	**0.10**
1-m	**0.27**	**0.13**	**0.36**	**0.34**
Conformity	**0.38**	0.05	**0.38**	**0.31**
ρRVRH	**0.32**	**0.06**	**0.35**	**0.33**
μ_c	**0.38**	0.05	**0.38**	**0.31**
mχe	**0.79**	**0.60**	**0.40**	**0.42**
mχv	**0.98***	**0.96***	**0.76***	**0.91**
mχo	**0.88**	**0.83**	**0.36**	**0.84**
mδd	**0.65**	**0.37**	**0.33**	**0.27**
mδv	**0.98**	**0.96**	**0.76**	**0.91**
mδs	**0.89**	**0.85**	**0.38**	**0.85**
α_s	**0.39**	**0.18**	**0.24**	**0.11**
H_i	**0.99***	**0.94**	**0.73**	**0.96***
H_p	**0.42**	**0.09**	**0.34**	**0.26**
S_0	**0.99***	**0.94**	**0.73**	**0.96***
S_1	**0.42**	**0.39**	**0.17**	**0.31**
S_2	**0.55**	**0.40**	**0.28**	**0.41**
S_3	**0.81**	**0.79**	**0.30**	**0.81**
σ^0_{HH}	**0.99**	**0.89**	**0.65**	**0.93**
σ^0_{HV}	**0.97**	**0.88**	**0.65**	**0.78**
σ^0_{VV}	**0.98**	**0.93**	**0.68**	**0.94**
$\sigma^0_{VV/HH}$	**0.14**	**0.06**	**0.09**	**0.13**
$\sigma^0_{HV/HH}$	**0.24**	**0.32**	**0.09**	**0.54**
$\sigma^0_{HV/VV}$	**0.29**	**0.32**	**0.06**	**0.60**
$\text{CPSeaIce}_{\text{Delta}}$	**0.95**	**0.89**	**0.55**	**0.91**
$\text{CPSeaIce}_{\text{Depol}}$	**0.98**	**0.96***	**0.75***	**0.93***
$\text{CPSeaIce}_{\text{Rco}}$	**0.93**	**0.78**	**0.48**	**0.86**

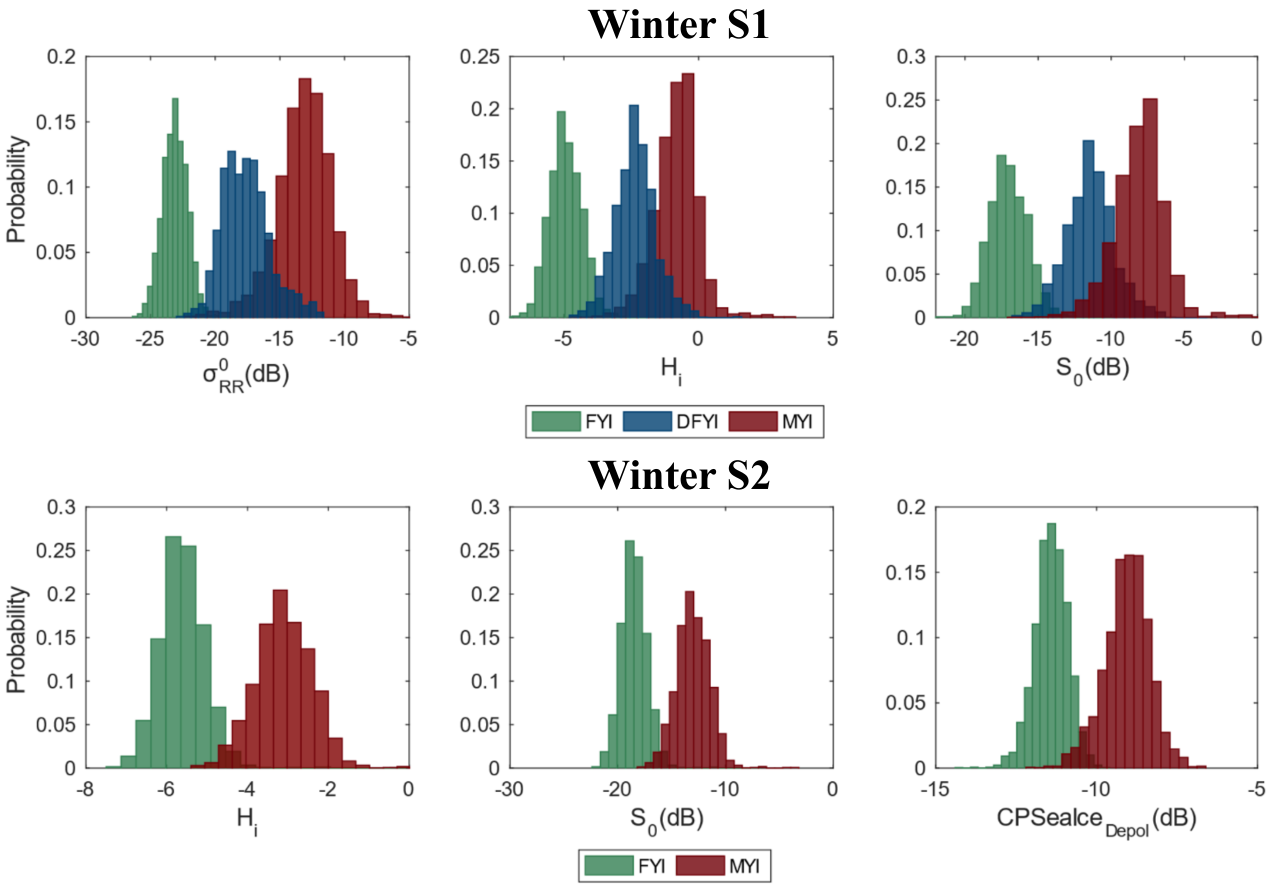

Figure 3.3 Histograms of CP parameters that exhibited the highest KS separability for Winter S1 (top) and Winter S2 (bottom). FYI distributions are shown in green, DFYI in blue and MYI in brown.

Table 3.5 shows average KS separability and the standard deviation of each GLCM feature calculated for the top three most separable CP parameters. Overall, FYI/MYI discriminability was higher for Winter S1 than Winter S2. Similarly to the KS analyses of RCM parameters, FYI/DFYI separability was generally higher than MYI/DFYI. MAX and GLC exhibited low discriminability. Generally, CON, DIS, HOM, ASM, ENE, ENT and GLC KS separability was not higher than separability using RCM parameters for FYI/MYI of Winter S2, and showed higher variability between the three source parameters (higher standard deviation) than Winter S1. However, for GLM and GLV GLCM features, the average separability between MYI and DFYI improved from 0.76 to 0.89. Overall, GLM and GLV showed consistently higher separability across both scenes for all ice type combinations.

Table 3.5 Winter S1 and Winter S2 average (and standard deviation) KS distances representing separability between sea ice types using RCM and GLCM texture features. RCM refers to the average separability of the top three CP parameters. Each GLCM value is the average separability of the feature, calculated for the top three parameters. All values are statistically significant ($p<0.01$).

	FYI/MYI		**FYI/DFYI**	**MYI/DFYI**
	Winter S1	Winter S2	Winter S1	Winter S1
RCM	0.99 (0.00)	0.95 (0.01)	0.96 (0.01)	0.76 (0.01)
CON	1.00 (0.00)	0.48 (0.42)	0.95 (0.05)	0.47 (0.26)
DIS	1.00 (0.00)	0.46 (0.45)	0.93 (0.09)	0.47 (0.27)
HOM	1.00 (0.01)	0.41 (0.50)	0.91 (0.10)	0.50 (0.35)
ASM	0.99 (0.01)	0.43 (0.48)	0.91 (0.07)	0.52 (0.31)
ENE	0.99 (0.01)	0.43 (0.48)	0.91 (0.07)	0.52 (0.31)
MAX	0.95 (0.08)	0.38 (0.50)	0.78 (0.14)	0.49 (0.27)
ENT	1.00 (0.00)	0.45 (0.46)	0.96 (0.03)	0.52 (0.35)
GLM	1.00 (0.00)	1.00 (0.00)	1.00 (0.00)	0.88 (0.01)
GLV	1.00 (0.00)	1.00 (0.01)	1.00 (0.00)	0.89 (0.01)
GLC	0.52 (0.37)	0.69 (0.33)	0.48 (0.43)	0.35 (0.18)

3.4.1.2 Advanced Melt

Table 3.6 shows KS statistics representing ice type separability for Advanced Melt S1 (FQ4) and Advanced Melt S2 (SQ21). Advanced Melt S1 KS statistics represent separability between FYI and MYI, whereas separability was calculated for FYI/MYI, FYI/DFYI and DFYI/MYI for Advanced Melt S2. Advanced Melt S1 yielded higher KS separability values than Advanced Melt S2, with optimal parameters for FYI/MYI discrimination being σ^0_{RR}, S_2 and $m\chi v$, with KS statistics of 0.59 for σ^0_{RR} and 0.50 for S_2 and $m\chi v$ (Figure 3.3). Conversely, the highest KS separability for Advanced Melt S2 was 0.35. As expected, separability between ice types decreases significantly from *winter* to *advanced melt*. However, Advanced Melt S1 shows promise for the use of steep incidence angle imagery to discriminate between FYI and MYI during the melt season.

Table 3.6 Advanced Melt S1 and Advanced Melt S2 KS distances (0 to 1) for major ice types. Bolded values are statistically significant ($p<0.01$). Cell shading visually emphasizes separability, with high separability values corresponding to light shading and low separability to dark shading. The top three most separable CP parameters which were used in the subsequent GLCM calculation are denoted with an asterisk (*).

	Advanced Melt S1	**Advanced Melt S2**		
Parameter	FYI/MYI	FYI/MYI	FYI/DFYI	DFYI/MYI
σ^0_{RH}	**0.32**	**0.35***	**0.18**	**0.29**
σ^0_{RV}	**0.42**	**0.29**	**0.16**	**0.22**
σ^0_{RR}	**0.59***	**0.18**	**0.21***	0.03
σ^0_{RL}	**0.33**	**0.34**	**0.16**	**0.33**
$\sigma^0_{RV/RH}$	**0.20**	0.03	**0.10**	**0.11**
δ	**0.47**	**0.17**	**0.11**	**0.09**
1-m	**0.08**	**0.22**	0.04	**0.25**
Conformity	**0.15**	**0.25**	0.05	**0.29**
ρRVRH	**0.08**	**0.22**	**0.06**	**0.26**
μ_c	**0.15**	**0.25**	**0.07**	**0.32**
mχe	**0.39**	0.04	**0.08**	**0.12**
mχv	**0.50***	**0.23**	**0.20**	**0.08**
mχo	**0.25**	**0.30**	**0.12**	**0.31**
mδd	**0.40**	**0.10**	0.04	**0.09**
mδv	**0.50**	**0.23**	**0.20***	**0.08**
mδs	**0.27**	**0.29**	**0.11**	**0.30**
α_s	**0.28**	**0.21**	**0.07**	**0.24**
H_i	**0.40**	**0.35***	**0.17**	**0.33***
H_p	**0.19**	**0.25**	**0.06**	**0.28**
S_0	**0.40**	**0.35***	**0.20**	**0.31**
S_1	**0.27**	**0.07**	**0.09**	**0.08**
S_2	**0.50***	**0.07**	**0.09**	**0.09**
S_3	**0.23**	**0.29**	**0.12**	**0.33***
σ^0_{HH}	**0.35**	**0.35**	**0.15**	**0.33**
σ^0_{HV}	**0.47**	**0.21**	**0.16**	**0.07**
σ^0_{VV}	**0.32**	**0.32**	**0.17**	**0.25**
$\sigma^0_{VV/HH}$	0.02	**0.09**	**0.17**	**0.09**
$\sigma^0_{HV/HH}$	0.03	**0.20**	**0.13**	**0.28**
$\sigma^0_{HV/VV}$	0.03	**0.22**	0.03	**0.22**
$\text{CPSeaIce}_{\text{Delta}}$	**0.30**	**0.34**	**0.15**	**0.33***
$\text{CPSeaIce}_{\text{Depol}}$	**0.49**	**0.34**	**0.25***	**0.24**
$\text{CPSeaIce}_{\text{Rco}}$	**0.35**	**0.24**	**0.10**	**0.17**

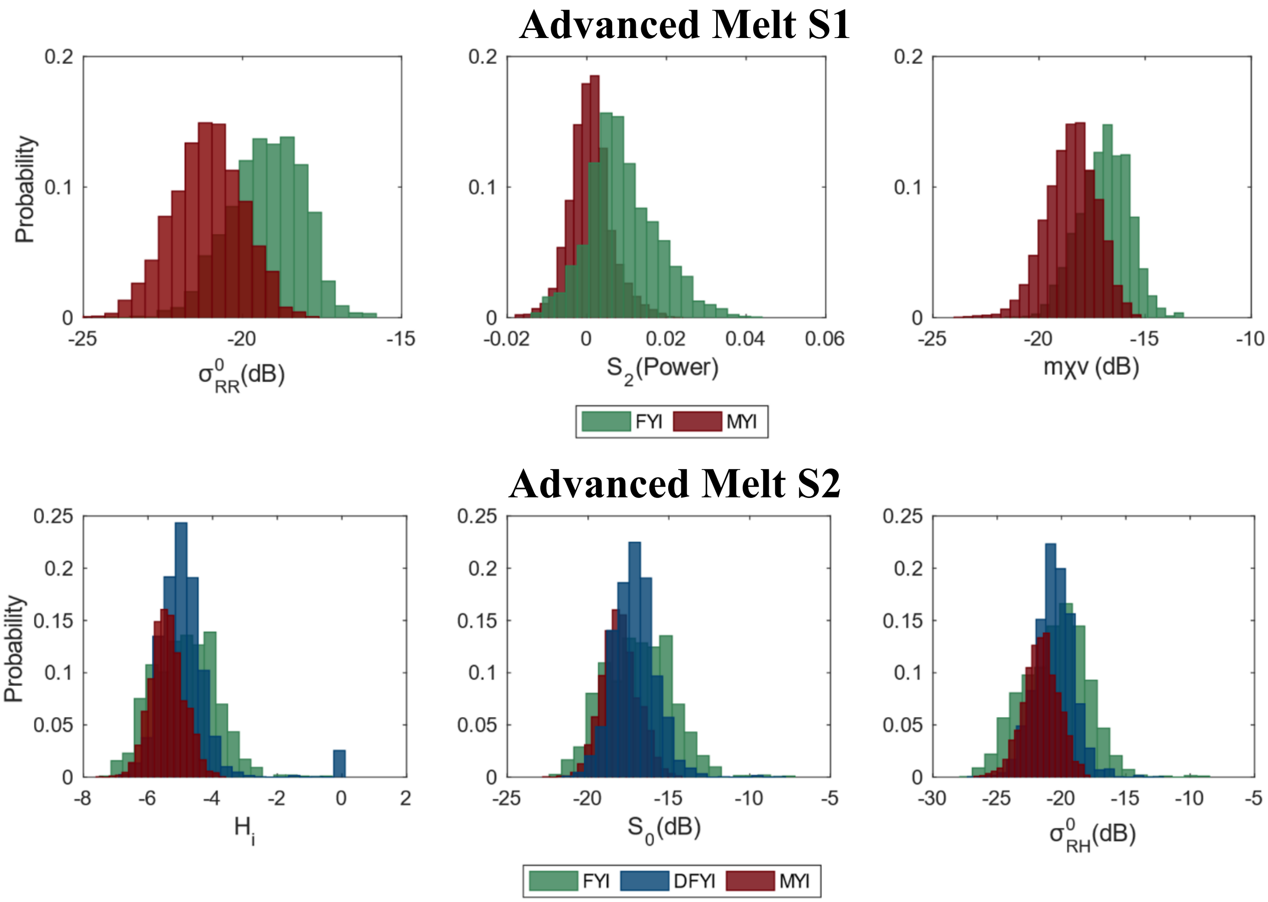

Figure 3.4 Histograms of CP and linear parameters that exhibited the highest KS separability for Advanced Melt S1 (top) and Advanced Melt S2 (bottom). FYI distributions are shown in green, DFYI in blue and MYI in brown.

Table 3.7 shows the average and standard deviation of KS distances for each GLCM feature calculated for the top three CP parameters with the highest KS statistics for each ice type combination. Advanced Melt S1 σ^0_{RR}, S_2 and mχv all had an average KS separability of 0.53; this is surpassed by GLM or GLV with a separability of 0.77. Similarly, average KS separability for FYI/MYI in Advanced Melt S2 was 0.35; this is also surpassed by GLM and GLV, with a separability of 0.55 and 0.56, respectively. For both scenes, only GLM and GLV achieved higher separability between FYI and MYI. For Advanced Melt S2, all GLCM parameters achieved higher ice type separability than RCM for FYI/DFYI, with the highest separability of 0.43 observed using ASM and ENE. Finally, MYI/DFYI average discriminability for RCM parameters was 0.33 which was surpassed by GLM and GLV reaching 0.69 and 0.70, respectively. Since GLM and GLV improved separability between ice types during *winter* and *advanced melt*, they were included in subsequent SVM image classification.

Table 3.7 Advanced Melt S1 and Advanced Melt S2 average (and standard deviation) KS distances representing separability between sea ice types using CP and GLCM texture features. RCM refers to the average separability of the top three CP parameters. Each GLCM value is the average separability of the feature, calculated for the top three parameters. All values are statistically significant (p<0.01).

	FYI/MYI		**FYI/DFYI**	**MYI/DFYI**
	Advanced Melt S1	Advanced Melt S2	Advanced Melt S2	Advanced Melt S2
RCM	0.53 (0.04)	0.35 (0.00)	0.22 (0.03)	0.33 (0.00)
CON	0.44 (0.12)	0.22 (0.15)	0.28 (0.09)	0.34 (0.19)
DIS	0.45 (0.14)	0.25 (0.09)	0.31 (0.15)	0.34 (0.16)
HOM	0.37 (0.25)	0.33 (0.12)	0.40 (0.17)	0.34 (0.10)
ASM	0.36 (0.22)	0.37 (0.11)	0.43 (0.13)	0.31 (0.05)
ENE	0.36 (0.22)	0.37 (0.11)	0.43 (0.13)	0.31 (0.05)
MAX	0.35 (0.06)	0.38 (0.09)	0.42 (0.07)	0.19 (0.02)
ENT	0.33 (0.27)	0.33 (0.12)	0.41 (0.16)	0.34 (0.06)
GLM	0.77 (0.05)	0.55 (0.01)	0.35 (0.04)	0.68 (0.02)
GLV	0.77 (0.05)	0.56 (0.01)	0.36 (0.04)	0.69 (0.02)
GLC	0.29 (0.02)	0.34 (0.15)	0.26 (0.16)	0.24 (0.05)

3.4.2 Ice Type Classification

3.4.2.1 Winter

Winter S1 exhibited an overall classification accuracy of 81.21%, and a Kappa coefficient of 0.71. By ice type, FYI showed the highest overall accuracy of 95.11%, followed by DFYI with 82.08% and MYI with 73.69%. With inclusion of GLM and GLV texture parameters, overall classification accuracy increased to 90.53%, with a Kappa coefficient of 0.85. Winter S2 had an overall classification accuracy of 96.93% (Kappa = 0.94), which increased to 99.37 (Kappa = 0.99) with inclusion of GLM and GLV. The majority of the increase in accuracy occurred for MYI, with the accuracy increasing from 96.07% to 100.00%. FYI overall accuracy increased from 97.84% to 98.72% (Table 3.8).

Table 3.8 Winter classification accuracies by ice type, average overall accuracies and Kappa coefficients. Each scene was classified using CP parameters alone and using CP parameters with corresponding GLCM Mean and GLCM Variance texture features as input variables.

		Accuracy by Ice Type (%)				
Scene	Input Parameters	FYI	DFYI	MYI	Overall Accuracy (%)	Kappa Coefficient
Winter S1	CP Only (σ^0_{RR}, H_i, S_0)	95.11	82.08	73.69	81.21	0.71
	CP & GLCM	99.68	86.77	89.1	90.53	0.85
Winter S2	CP Only ($CPSeaIce_{Depol}$, H_i, S_0)	97.84	-	96.07	96.93	0.94
	CP & GLCM	98.72	-	100	99.37	0.99

Figure 3.5 shows the dominant stage of development (ice type) of the study area (Figure 3.5a), Freeman-Durden decomposition of the RADARSAT-2 imagery used to simulate the RCM parameters (Figure 3.5b), σ^0_{RH} backscatter of the simulated RCM data (Figure 3.5c), and the results of the supervised SVM classification of Winter S1 with CP parameters alone as input variables (Figure 3.5d), as well as both CP parameters and GLM and GLV texture parameters (Figure 3.5e). According to the CIS ice chart data, the area covered by Winter S1 is dominated by MYI and thick FYI. In Figure 3.5b the Freeman-Durden decomposition characterizes areas of smooth FYI as dark blue which correspond to surface scattering as the dominant scattering mechanism. DFYI is characterized by a combination of surface and volume scattering with the former likely dominant; the rougher surfaces resulting in a lighter blue colour. MYI is characterized by a more equal combination of surface and volume scattering, resulting in a cyan colour.

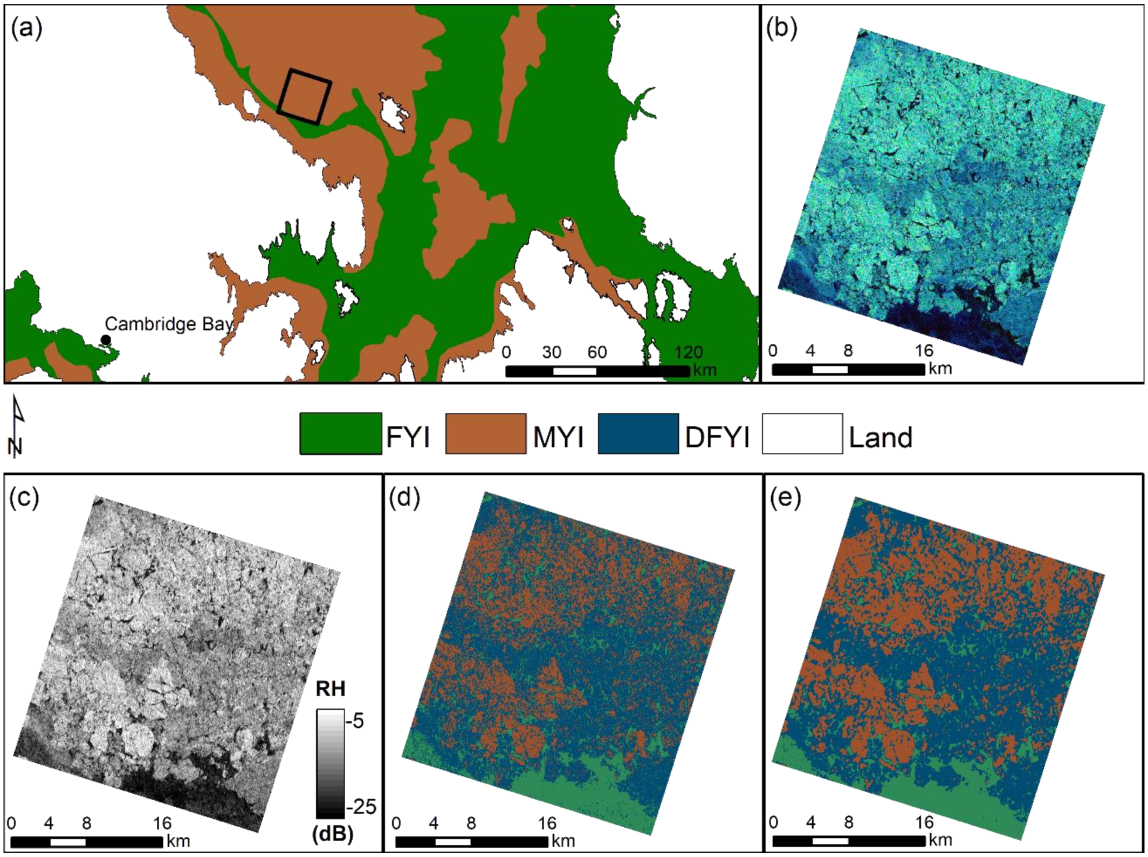

Figure 3.5 Winter S1 (FQ15) classification results. (a) CIS ice chart depicting dominant sea ice stage of development (no distinction is made between FYI and DFYI in charts). The black polygon shows the location of Winter S1 RADARSAT-2 image acquisition (b) Freeman-Durden decomposition RGB composite of the RADARSAT-2 image used to simulate the CP parameters. Red corresponds to dominant double bounce scattering, green to volume scattering and, blue to surface scattering. (c) RCM RH backscatter. (d) SVM classification output using 3 most separable CP parameters as input variables. (e) Classified image using CP parameters as well as GLM and GLV texture parameters as input variables.

The input parameters for the classification in Figure 3.5d were σ^0_{RR}, H_i and S_0. They are shown along with the Freeman-Durden decomposition in Figure 3.6. All three parameters showed high separability between the three ice types, with marginal overlap in signatures between MYI and DFYI. Considering σ^0_{RR} (Figure 3.6b), FYI ranges from -28 dB to approximately -20 dB, DFYI ranges between -22 dB and -12 dB, and MYI ranges from approximately -18 dB to -5 dB (Figure 3.3). For sea ice applications σ^0_{RR} is said to be high during high volume scattering situations, leading to depolarization of the incident wave, with this type of behaviour occurring on MYI more than FYI. Shannon Entropy is composed of the intensity (H_i) and polarimetric (or phase) components and is a measure of target disorder and depends on the total power and the target surface roughness. H_i (Figure 3.6c) exhibits a smaller contrast between MYI and DFYI than σ^0_{RR}, but retains high visual separability between both FYI and both DFYI and MYI. H_i is highly dependent on surface roughness, thus the reduced separability for DFYI and MYI evident in Figure 3.6c and by the high overlap of histograms in Figure 3.3 can be explained by the fact that both MYI and DFYI are characterized by high surface roughness.

S_0 (Figure 3.6d) represents total power and is thus sensitive to all scattering mechanisms. DFYI and MYI are expected to have higher total intensity of backscatter as a result of increased volume and surface scattering, compared to FYI. Due to exposure to melting conditions, MYI undergoes desalination processes which lowers its bulk salinity and leaves air bubbles in place of brine. Thus MYI is characterized by increased penetration for C-band frequency and enhanced volume scattering from the desalinated upper layer. In contrast, FYI has a much higher bulk salinity which reduces the penetration depth and, leads to relatively little volume scattering. MYI has the highest S_0 (0 to -5 dB), followed by DFYI (-5 to -17 dB) and FYI (-12 to -22 dB) (Figure 3.3). Similarly, Figure 3.6d shows bright areas associated with MYI, followed by lower intensity areas of DFYI, and dark areas dominated by FYI.

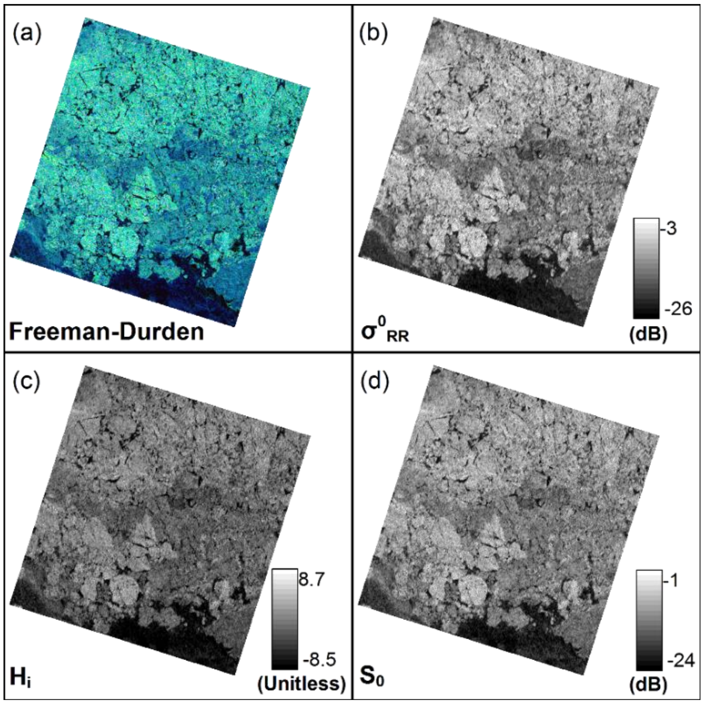

Figure 3.6 Winter S1 (FQ15) Freeman-Durden decomposition of the RADARSAT-2 scene used to simulate the RCM parameters is shown in (a). Classification input variables are σ^0_{RR}, shown in (b), H_i, shown in (c) and S_0, shown in (d).

From the by ice type classification accuracy results, it can be seen that the decrease in classification accuracy is dominated by confusion between DFYI and MYI, with FYI displaying very high classification accuracy using either CP parameters (~96%), or CP and GLCM texture features (100%). GLV and GLM are both “statistics group” parameters and rely on statistical relationships between neighbouring pixels, thus increasing homogeneity in homogeneous areas, and increasing heterogeneity in heterogeneous areas such as edges of ice floes. It is likely that the calculation of GLV and GLM within a relatively large window size of 9 by 9 also leads to an overall generalization of the scene as well as further reduction of speckle which contribute to improved classification accuracies and visual representation of the ice. With the inclusion of texture (Figure 3.5e), areas of FYI, DFYI and MYI appear much more uniform. Overall, the confusion between classes is reduced with the addition of GLCM texture parameters.

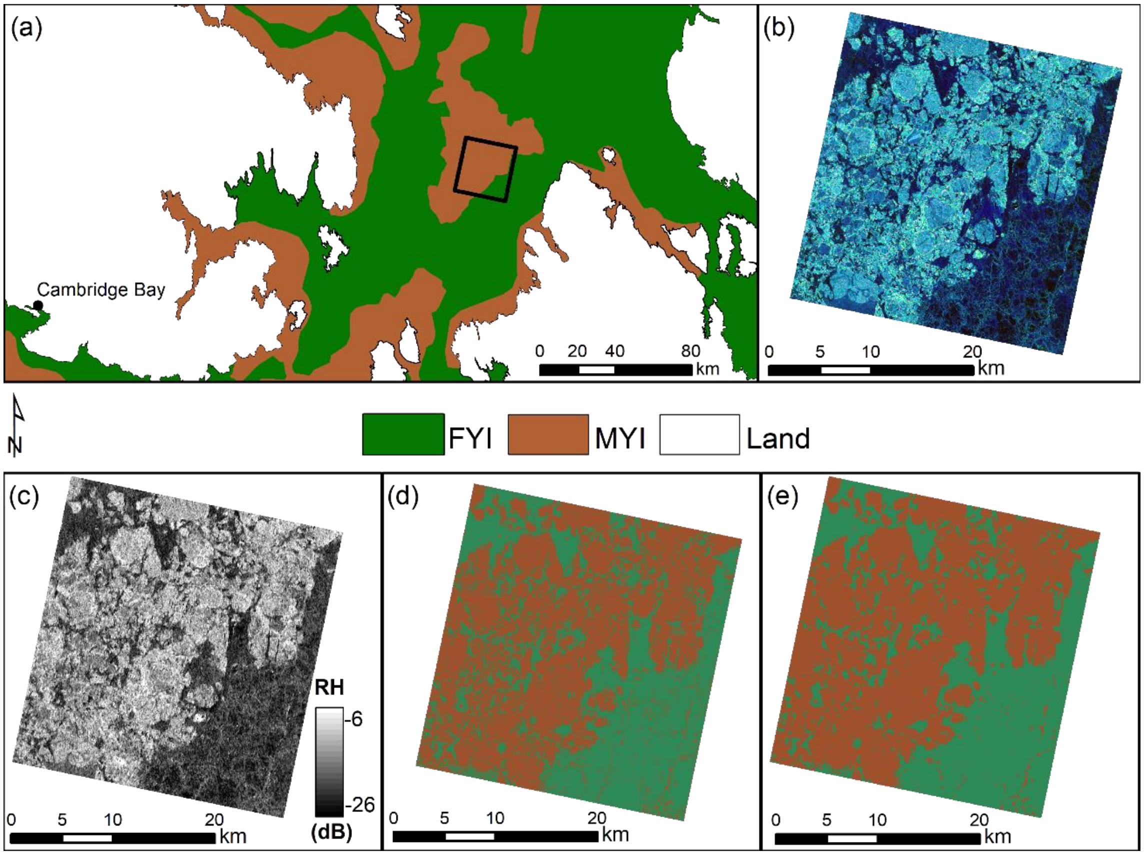

Figure 3.7 Winter S2 (FQ21) classification results. (a) CIS ice chart depicting dominant sea ice stage of development. The black polygon is showing the location of Winter S1 RADARSAT-2 acquisition (b) Freeman-Durden decomposition RGB composite of quad-pol RADARSAT-2 image used to simulate the RCM parameters. Red corresponds to dominant double bounce scattering, green to volume scattering and, blue to surface scattering. (c) RCM RH backscatter. (d) SVM classification output using 3 most separable RCM parameters as input variables. (e) Classified image using RCM parameters with highest ice type separability and GLCM Mean and GLCM Variance texture parameters as input variables.

At the time of the Winter S2 (FQ21) RADARSAT-2 acquisition, the area of interest primarily consisted of MYI and thick FYI (Figure 3.7a). This can be seen in higher detail on the RGB composite of the Freeman-Durden decomposition of the RADARSAT-2 image used to simulate the RCM parameters (Figure 3.7b). The scene only contains surface scattering FYI, which appears dark blue in Figure 3.7b, and MYI, which appears as cyan due to a combination of volume and surface scattering. Edges of MYI floes appear to be light green and magenta in colour which is linked with high volume and double bounce scattering, respectively. The edges of ice floes will have a higher component of double bounce scattering because these areas are dominated by compression and thus high geometric roughness.

The input parameters for the classification were H_i, S_0 and $CPSeaIce_{Depol}$ and visual separability between FYI and MYI is high for all three channels (Figure 3.8). H_i is highly dependent on surface roughness and total power and therefore exhibits high separability between smooth FYI and MYI. Similarly, S_0 which is representative of total power also allows for good differentiation between FYI and MYI but not as strong as H_i (Figure 3.8b and c). Finally, $CPSeaIce_{Depol}$ shows good visual separability between FYI and MYI as it is sensitive to both surface and volume scattering.

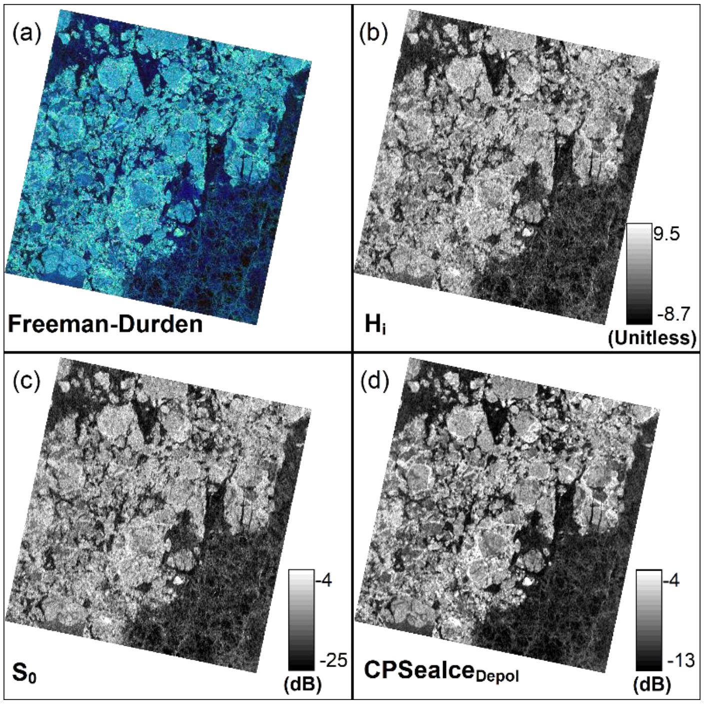

Figure 3.8 Winter S2 Freeman-Durden decomposition of the RADARSAT-2 scene used to simulate the RCM parameters is shown in (a). Classification input variables are H_i shown in (b), S_0 shown in (c) and, $CPSeaIce_{Depol}$ shown in (d).

Similar to Winter S1, Winter S2 classification accuracies improved with the addition of texture features (Table 3.8). The addition of GLM and GLV increased FYI classification accuracy from 96.93% to 99.37%. MYI accuracy increased from 96.07% to 100%. The reduction of speckle-like misclassified pixels on FYI and MYI is even more pronounced in Winter S2 than Winter S1 (Figure 3.7e). The majority of the MYI floes are not contaminated by small amounts of “FYI pixels” without loss of detail in small areas of FYI. However, some ridges of FYI in the southeast corner of the scene are being misclassified as MYI.

3.4.2.2 Advanced Melt

Advanced Melt S1 (FQ4) had an overall classification accuracy of 77.06% with a Kappa coefficient of 0.52 using only CP parameters as input variables. With the inclusion of GLM and GLV, overall classification accuracy of 85.91% was observed, an increase of 8.85%. The Kappa coefficient increased by 26.76%, to 0.71. The overall accuracies and Kappa coefficients of Advanced Melt S2 (SQ21) were lower. However, overall classification accuracy using CP and GLCM parameters was higher at 61.17% (Kappa = 0.41), compared to CP parameters alone of 48.54% (Kappa = 0.21). By ice type, Advanced Melt S1 had higher overall classification accuracies for MYI than FYI. MYI overall classification accuracies were 86.31% and 94.22% using CP parameters only, and CP plus GLCM, respectively. The inclusion of GLM and GLV significantly improved overall classification accuracy of FYI from 65.06% to 75.14%. Using CP parameters as input variables, Advanced Melt S2 had classification accuracies of 30.29%, 48.29% and 63.98% for FYI, DFYI and MYI, respectively. With the inclusion of GLM and GLV, classification accuracies increased to 67.75%, 63.33% for FYI and DFYI, respectively. However, a decrease was observed for MYI to 52.65% (Table 3.9).

Table 3.9 Classification accuracies by ice type, average overall accuracies and Kappa coefficients. Each scene was classified using CP parameters alone and using CP parameters with corresponding GLCM Mean and GLCM Variance texture features as input variables.

		Accuracy by Ice Type (%)				
Scene	Input Parameters	FYI	DFYI	MYI	Overall Accuracy (%)	Kappa Coefficient
Advanced Melt S1	CP Only (σ^0_{RR}, S_2, mχv)	65.06	-	86.31	77.06	0.52
	CP & GLCM	75.14	-	94.22	85.91	0.71
Advanced Melt S2	CP Only (H_i, S_0, σ^0_{RH})	30.29	48.29	63.98	48.54	0.21
	CP & GLCM	67.75	63.33	52.65	61.17	0.41

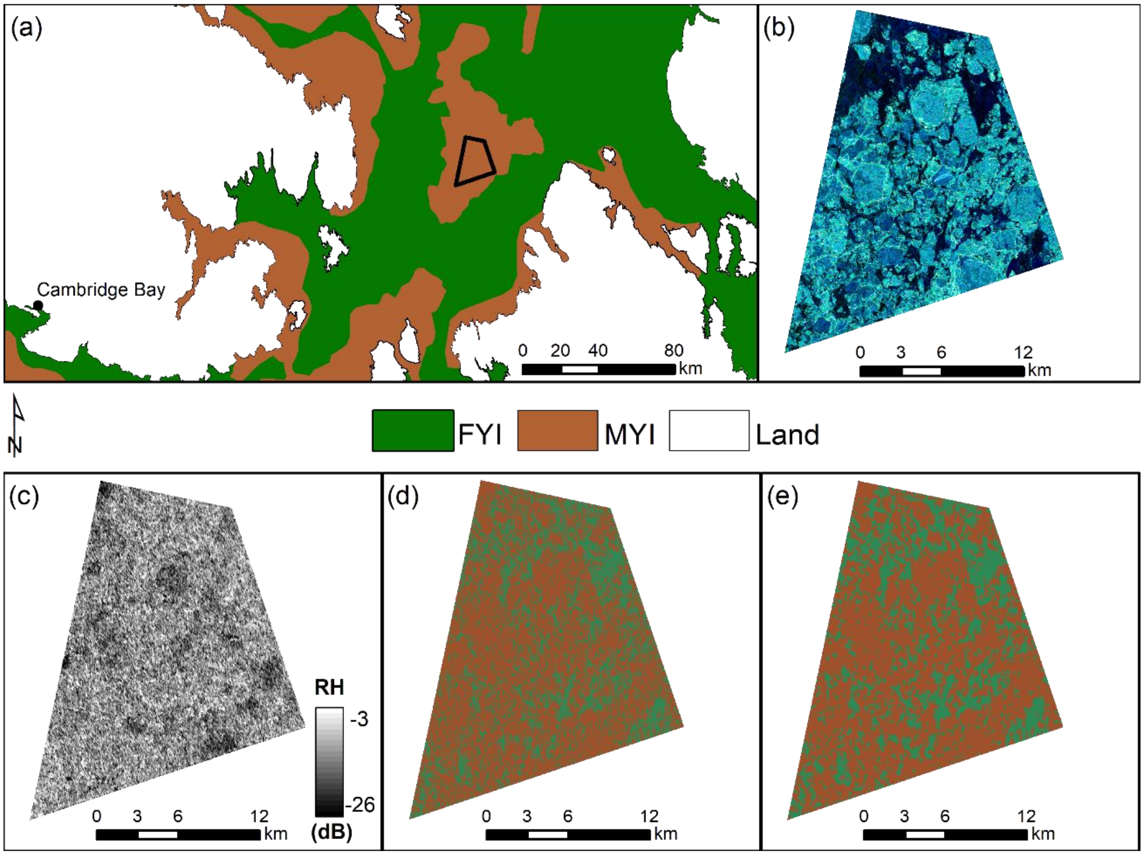

Figure 3.9 Advanced Melt S1 (FQ4) classification results. (a) CIS ice chart depicting dominant sea ice stage of development. The black polygon shows the location of Advanced Melt S1 acquisition (b) Freeman-Durden decomposition RGB composite of quad-pol RADARSAT-2 image used to simulate the RCM parameters. Red corresponds to dominant double bounce scattering, green to volume scattering and, blue to surface scattering. (c) RCM RH backscatter. (d) SVM classification output using 3 most separable RCM parameters as input variables. (e) Classified image using RCM parameters with highest ice type separability and GLCM Mean and GLCM Variance texture parameters as input variables.

Figure 3.9 shows the CIS ice chart data, collocated *winter* RADARSAT-2 imagery, Advanced Melt S1 σ^0_{RH} backscatter, and two classification outputs corresponding to CP parameters and CP and GLCM texture parameters. The dominant stages of sea ice development in the area are MYI and thick FYI.

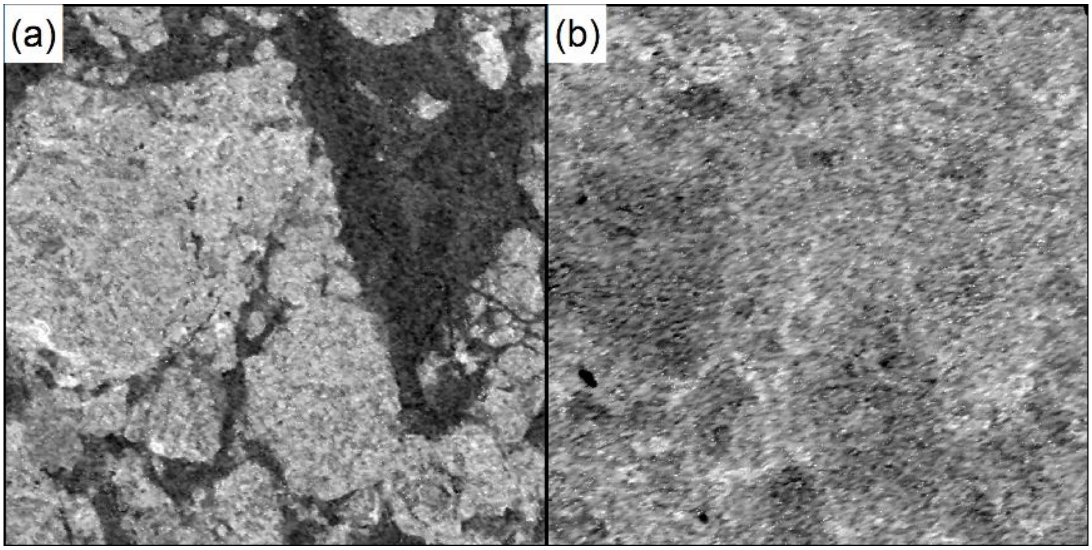

Figure 3.10 6 by 6 km panels of σ^0_{HH} depicting signature reversal in original Advanced Melt S1 RADARSAT-2 imagery. A mixture of FYI and MYI in the winter is shown in (a) and subsequent advanced melt conditions in (b).

During the melt season, the ice cover transitions from a combination of dry snow and bare ice to highly spatially and temporally variable matrix of melting snow, ice and melt ponds. During the *advanced melt* period the ice is mainly covered with bare or draining ice and melt ponds, with FYI typically exhibiting higher melt pond coverage than MYI. The penetration depth of C-band SAR is highly dependent on volumetric moisture content and is expected to be approximately 10 cm for wet snow, and less than 7 mm for liquid water [11,33]. A reversal in intensity of backscatter signatures in HH have been recorded for FYI and MYI in C-band and L-band frequencies during the melt season [33,34]. The phenomenon is attributed to the brine wetted snow grains of FYI leading to an increase in volume scattering, and the liquid content of the MYI snow pack masking the strong volume scattering signature of the MYI. The signature reversal in FYI and MYI, between *winter* and *advanced melt*, is observed in the HH channel of the original RADARSAT-2 imagery (Figure 3.10) and simulated CP parameters (Figure 3.11).

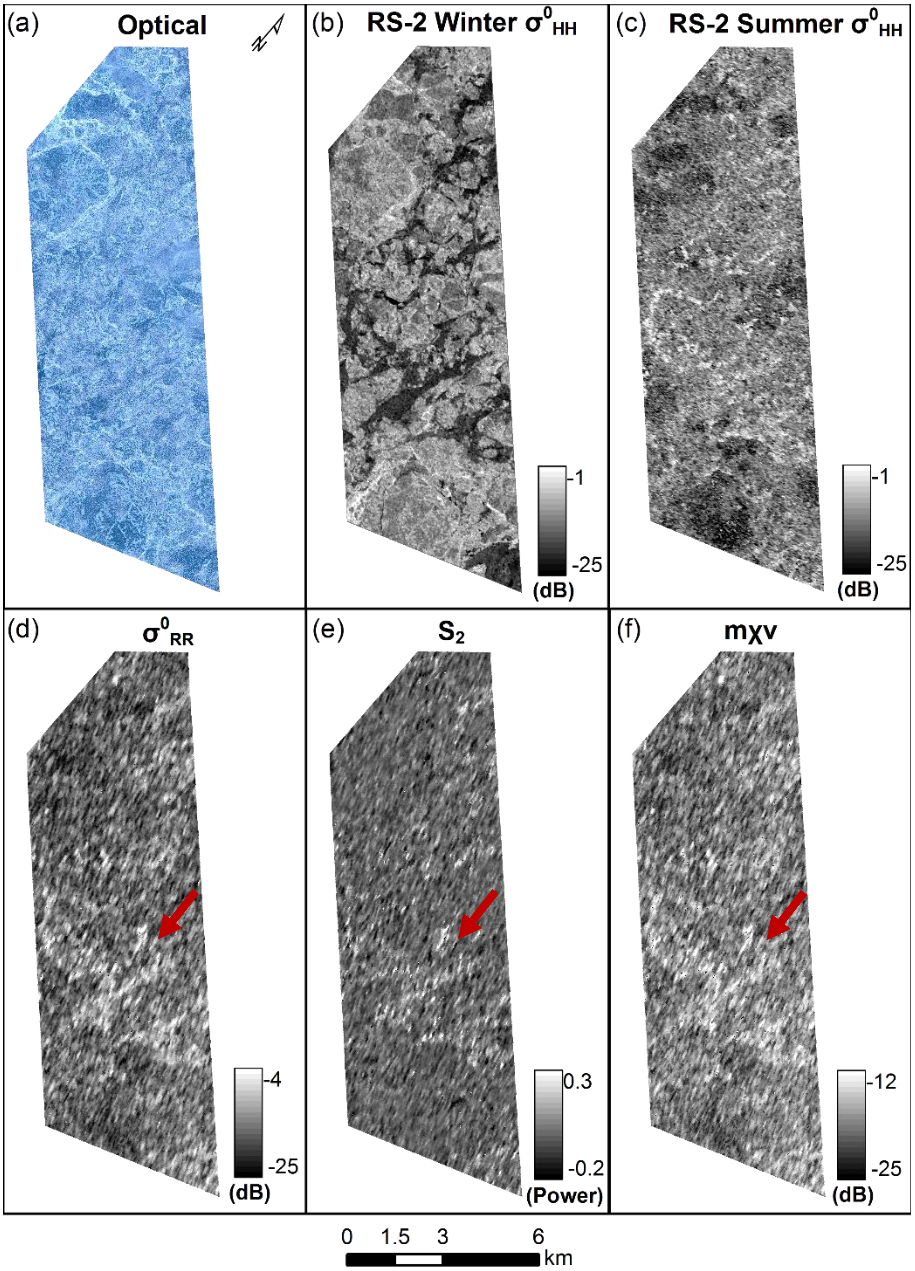

Figure 3.11 Advanced Melt S1 (FQ4) co-located panels coincident with the high resolution GeoEye-1 optical image. (a) GeoEye-1 optical imagery acquired on June 25, 2015, (b) Collocated winter RADARSAT-2 image, σ^0_{HH}, (c) σ^0_{HH} of the Advanced Melt S1 RADARSAT-2 image used to simulate the RCM parameters, (d) σ^0_{RR}, (e) S_2 and, (f) $m\chi v$. The red arrows point to high intensity areas associated with FYI.

Based on the available observations, we suggest the following explanation for the observed signature reversal in Advanced Melt S1. Figure 3.11a shows the GeoEye-1 high resolution optical image which was acquired on June 25, 2015, one day prior to the acquisition of the RADARSAT-2 image (Figure 3.11c) used to simulate the RCM parameters (Figures 3.11d – f). In the GeoEye-1 image it can be seen that the ice cover is dominated by melt ponds, with FYI experiencing higher melt pond coverage than MYI. At this stage of melt it is likely that the bright areas seen in the GeoEye-1 image correspond to bare ice, rather than melting snow. Using *in situ* scatterometer and wind speed measurements, Scharien et al. (2014) established relationships between wind speed and C-band backscatter at varying incidence angles (25°, 35°, 45° and 55°) on FYI melt ponds [35]. They found that backscatter intensity at a 25° incidence angle increases from approximately -30 dB, up to over -5 dB at wind speeds of approximately 2 m/s and higher. A similar, but weaker dependencies were observed at incidence angles of 35°, 45° and 55°[35]. Considering that FYI is characterized by a higher melt pond coverage than MYI, wind roughened melt ponds will enhance the backscatter from those areas, and allow for separability of FYI and MYI at a steep incidence angle. Furthermore, melt ponds on smooth FYI tend to be larger in area and form interconnected networks, compared to MYI which tends to have smaller, more isolated melt ponds due to greater ice topography [35,36]. This connectivity will lead to an increase in the fetch and wave growth of the melt ponds on FYI. Due to the lack of interconnected channels between melt ponds necessary for wave growth, and the effective masking of volume scattering from air bubble rich upper layer by melt ponds on MYI, MYI backscatter appears low. Finally, as observed in the *winter* period, the backscatter of SAR imagery acquired at a steep incidence angle exhibits a lower diffuse or specular component, thus is better able to capture the increase in backscatter intensity associated with wind roughened melt ponds on FYI.

σ^0_{RR}, S_2 and mχv exhibit higher intensity over FYI than MYI (Figure 3.11, Figure 3.4). It is expected that σ^0_{RR} and mχv will be higher in areas dominated by volume scattering, where the multiple bounces lead to depolarization of the incident wave. However, wind roughened melt ponds are expected to conform to Bragg scattering at wind speeds under 8.0 m/s [35], thus it is possible that the CP parameters which are sensitive to volume scattering are also sensitive to Bragg scattering.

Advanced Melt S2 (SQ21) is located in an area comprising MYI and thick DFYI (Figure 3.12). The northwest portion of the scene is covered by a large MYI floe which is approximately

~10 km in width, and 20 km in length. The northeast portion of the scene is dominated by smaller MYI floes and areas of DFYI. Finally the southern part of Advanced Melt S2 is predominately smooth FYI with long ridges.

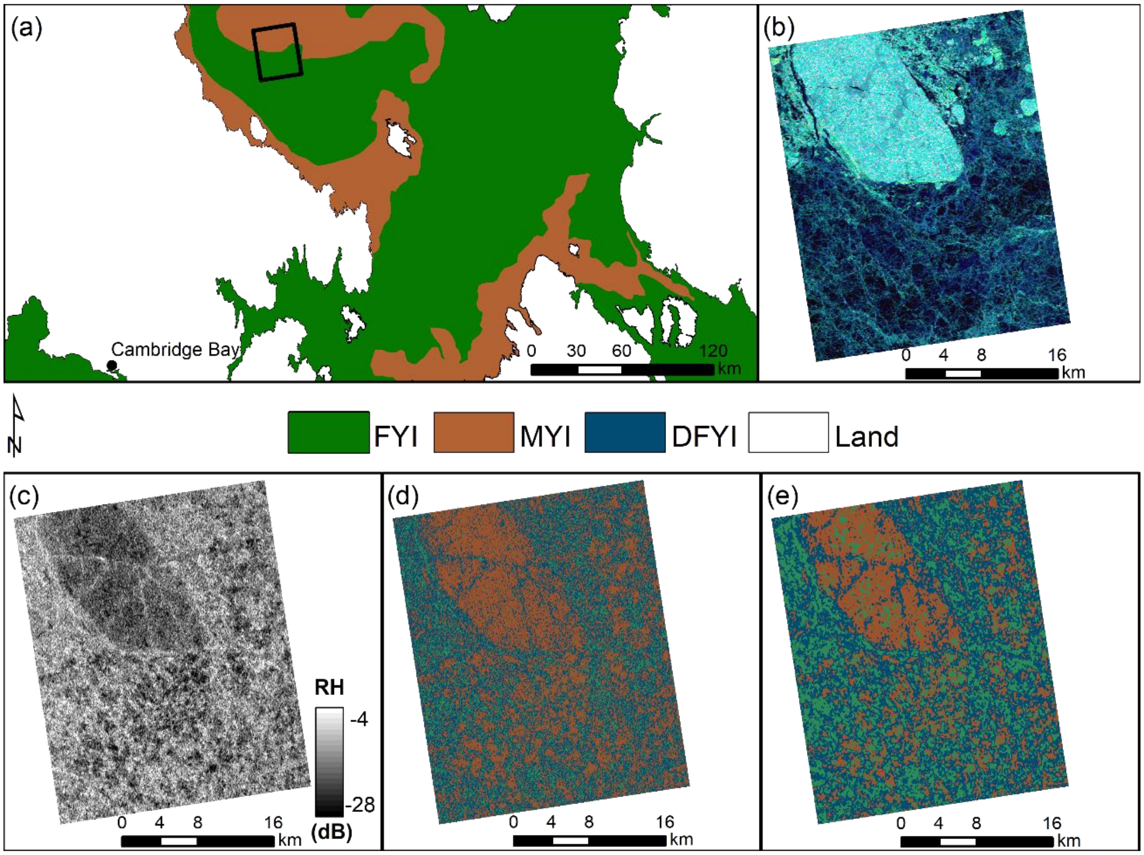

Figure 3.12 Advanced Melt S2 (SQ21) classification results. (a) CIS ice chart depicting dominant sea ice stage of development. The black polygons shows the location of Advanced Melt S2 acquisition (b) Freeman-Durden decomposition RGB composite of quad-pol RADARSAT-2 image used to simulate the RCM parameters. Red corresponds to dominant double bounce scattering, green to volume scattering and, blue to surface scattering. (c) RCM RH backscatter. (d) SVM classification output using 3 most separable RCM parameters as input variables. (e) Classified image using RCM parameters with highest ice type separability and GLCM Mean and GLCM Variance texture parameters as input variables.

At the time of image acquisition, Advanced Melt S2 exhibited a backscatter signature merging between ice types (Figure 3.4). A nearly complete overlap in backscatter intensities are observed for H_i, S_0 and σ^0_{RH}. Figure 3.13 shows a loss of visual separation between FYI and MYI, with FYI ridges and MYI retaining high σ^0_{RH}, and smooth FYI increasing in backscatter intensity. It can be seen that a lot of confusion exists between MYI and both FYI and DFYI, however, the large MYI floe was classified correctly (Figure 3.12d).

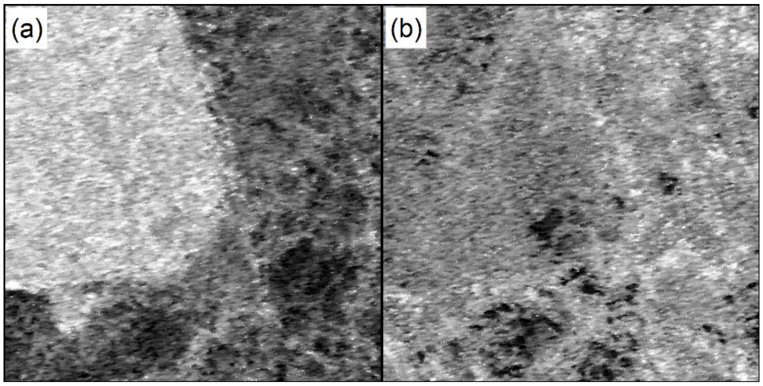

Figure 3.13 6 by 6 km σ^0_{HH} (dB) panels depicting signature merging in original Advanced Melt S2 RADARSAT-2 imagery. A mixture of FYI and MYI in the winter is shown in (a) and subsequent advanced melt conditions in (b).

Figure 3.14 shows that in all three RCM parameters the cracks in the large MYI floe are associated with high values, whereas the ice cover has low values. Figure 3.15 shows that the surface of the large MYI floe is dominated by bare ice areas and relatively small, discreet melt ponds (Figure 3.15a and b) compared to areas of FYI which have larger, more interconnected melt ponds among a matrix of DFYI (Figure 3.15b and c). The cracks in the MYI floe were classified as DFYI (Figure 3.12) and it can be seen in the aerial imagery that they are filled with water (Figure 3.15b). Similar to Advanced Melt S1, the bright areas in the aerial imagery are not likely to be associated with melting snow at this stage in the melt season because wide spread ponding is evident on both FYI (Figure 3.15a and b) and MYI (Figure 3.15c and d).

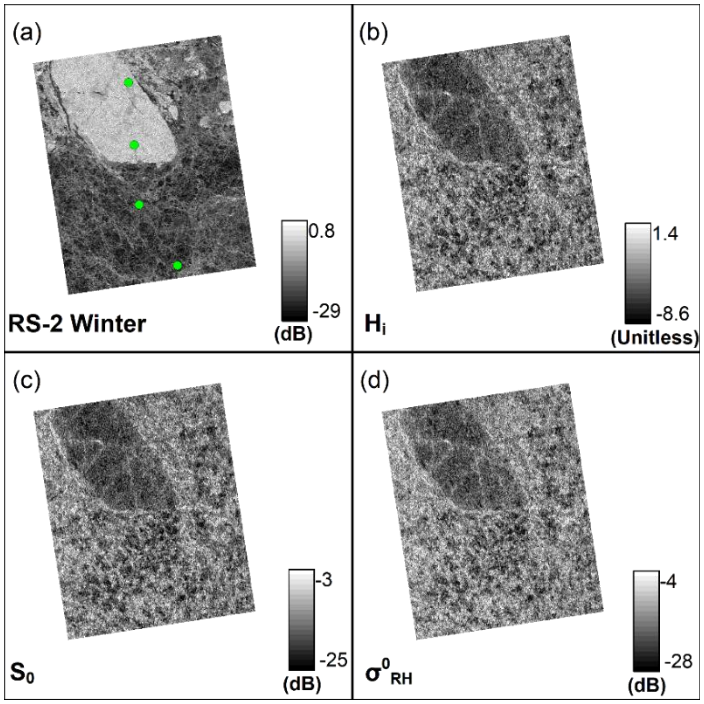

Figure 3.14 σ^0_{HH} backscatter of a collocated RADARSAT-2 winter scene is shown in (a) Advanced Melt S2 RCM classification input variables were H_i (shown in b), S_0 (shown in c) and $CPSeaIce_{Depol}$ (shown in d). The dots in (a) correspond to Figure 3.15, with the northernmost point corresponding to the photo in Figure 3.15a, progressing to the southernmost point, with the corresponding photo in Figure 3.15d.

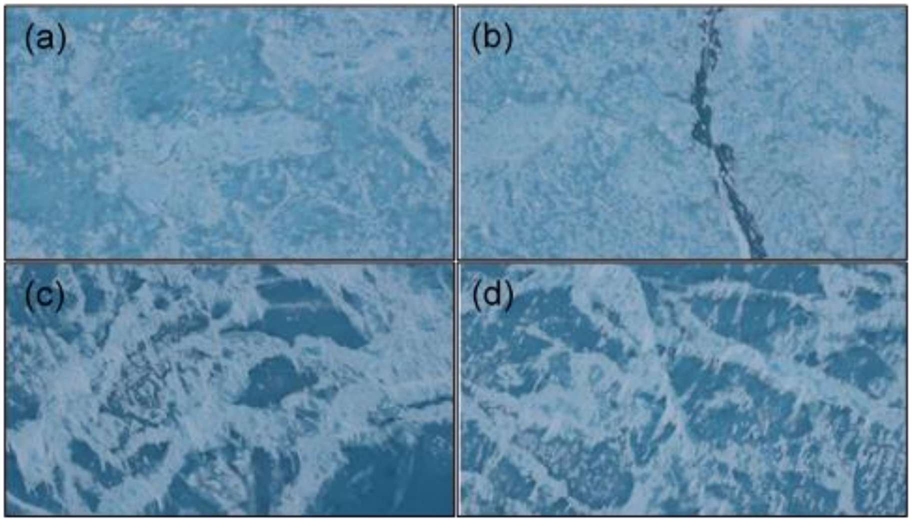

Figure 3.15 Imagery from aerial photography survey acquired over the area covered by Advanced Melt S2. The survey was conducted on June 21st, 2016, two days prior to the acquisition of Advanced Melt S2. The locations of the photos coincide with the point locations in Figure 3.15a, with the photo in panel (a) corresponding to the northernmost point in Figure 3.15a, and progressing to (d) corresponding to the southernmost point.

In general, the addition of GLM and GLV as input variables for supervised SVM classification improved classification accuracies for both *winter* and *advanced melt* scenes over a wide range of incidence angles (Figure 3.16). Most importantly, Advanced Melt S1 which was acquired at a steep incidence angle ranging between 22.3 and 24.2° showed a high classification accuracy of 86% using a combination of RCM and GLCM parameters.

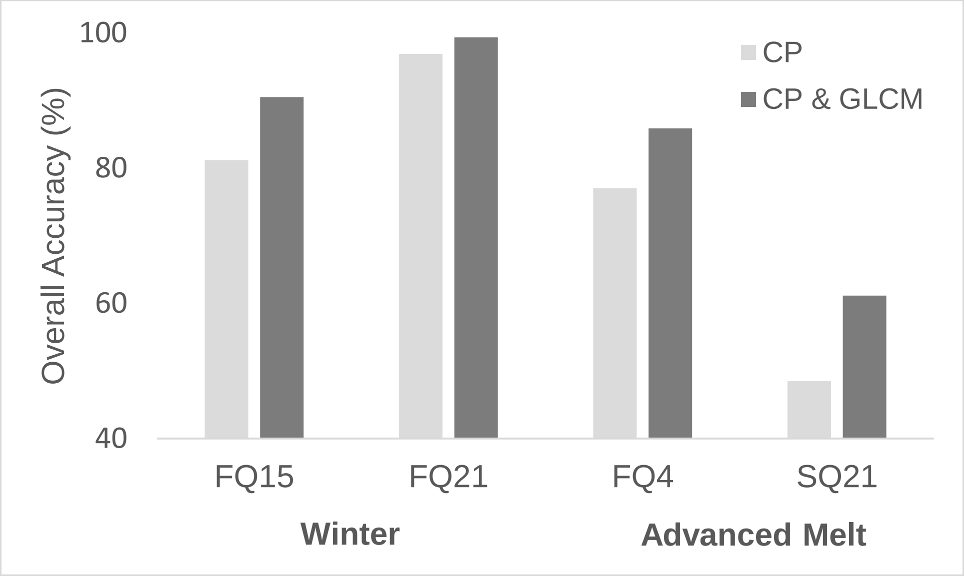

Figure 3.16 Comparison of overall classification accuracies by incidence angle and season. FQ15 and FQ21 correspond to Winter S1 and Winter S2, respectively. Similarly, FQ4 and SQ21 correspond to Advanced Melt S1 and Advanced Melt S2, respectively.

3.5 Conclusions

This study assessed the utility of simulated CP parameters associated with the upcoming RCM mission for ice type discrimination during the *winter* and *advanced melt* periods. Similar to previous studies conducted during the *winter* period, we found that σ^0_{RR}, H_i, S_0 and $CPSeaIce_{Depol}$ exhibit high separability between FYI, MYI and DFYI [25,26]. The results of supervised SVM classifications indicate that classification accuracies increase with the inclusion of statistics group GLCM texture parameters (GLM and GLV) by enhancing between class separability and reducing the presence of clusters of FYI pixels in a MYI zone and vice versa. Winter S1, which consisted of FYI, MYI and DFYI had an overall classification accuracy of 81.21% (Kappa = 0.71) using RCM parameters. The overall classification accuracy increased to 90.53% (Kappa = 0.85) with addition of GLM and GLV GLCM texture features. The majority of the confusion between classes was due to similarities in backscatter signatures between DFYI and MYI. Winter S2, composed of FYI and MYI, exhibited a higher overall classification accuracy of 96.93% (Kappa = 0.94) compared to Winter S1. The classification accuracy further improved to 99.37% (Kappa = 0.99) once GLCM texture features GLM and GLV were included as input variables.

It was found that σ^0_{RR}, S_2, and mχv CP parameters from Advanced Melt S1, acquired at a steep incidence angle, showed good ice type separability between FYI and MYI during *advanced melt*. An overall accuracy of 77.06% (Kappa = 0.52) was observed. A higher overall accuracy of 85.91% (Kappa = 0.71) was achieved by including GLM and GLV GLCM texture features. Shallow incidence angle Advanced Melt S2 showed reduced separability between major ice types and lower classification accuracies of 48.54% (Kappa = 0.21) using RCM parameters alone; classification accuracy improved marginally to 61.17% (Kappa = 0.41) with the inclusion of GLCM parameters.

The backscatter intensity inversion between FYI and MYI allows for discrimination of FYI and MYI during advanced melt. The sensitivity of steep incidence angle C-band SAR to wind roughened melt ponds even at low wind speeds leads to greater Bragg scattering on FYI. Whereas, the presence of melt ponds on MYI reduces C-band SAR penetration depth to less than 7 mm, thus masking volume scattering from melt pond covered areas of MYI. This intensity inversion allows for discrimination between FYI and MYI during the *advanced melt* period.

RCM is due for launch in late 2018 and will be a primary data source for the CIS. For operational ice charting applications we recommend the use of $\sigma^0_{RR,}$ H_i, S_0 and $\text{CPSeaIce}_{\text{Depol}}$ CP parameters during *winter*, and σ^0_{RR}, S_2, and mχv during *advanced melt*. Furthermore, we recommend the integration of statistical group GLCM texture parameters (GLM and GLV) for improved ice type separability, particularly during *advanced melt*. GLCM texture features can be easily integrated into workflows because they are scene specific, provide additional information on spatial relationships between pixels, and are not computationally intensive.

3.6 Acknowledgements

The research was conducted as part of the interdisciplinary Ice Covered Ecosystem - CAMbridge Bay Process Studies (ICE-CAMPS) project. Funding was provided by Marine Environmental Observation Prediction and Response Network (MEOPAR) and the National Sciences and

Engineering Research Council of Canada (NSERC)—Discovery Grants Program. Additional support was provided by the Northern Scientific Training Program (NSTP). RADARSAT-2 data and products © MacDonald, Dettwiler and Associated Ltd. All Rights Reserved. RADARSAT is an official mark of the Canadian Space Agency. RADARSAT-2 imagery are available for a fee from the National Earth Observation Data Framework Catalog (https://neodf.nrcan.gc.ca)

3.7 Appendix

Appendix 4.1 Simulated RCM compact polarimetric parameters, associated equations and units (Adapted from Geldsetzer et al, 2015)

CP Parameter	Description	Equation	Units
$\sigma^0_{\mathrm{RH}}, \sigma^0_{\mathrm{RV}}, \sigma^0_{\mathrm{RR}}, \sigma^0_{\mathrm{RL}}$	Sigma naught backscatter at varied polarizations	Right circular transmit, horizontal, vertical, right or left receive.	Power
$\sigma^0_{\mathrm{RV/RH}}$	Circular co-polarization ratio	$\sigma^0_{\mathrm{RV/RH}} = \frac{\sigma^0_{\mathrm{RV}}}{\sigma^0_{\mathrm{RH}}}$	Power
δ	Relative phase angle	$\delta = \tan^{-1}\left(\frac{S_3}{S_2}\right)$	Radians
1-m	Degree of depolarization	where $m = \frac{\sqrt{S_1^2+S_2^2+S_3^2}}{S_0}$	Unit-less
Conformity	Conformity coefficient	See Truong-Loi et al, 2009 for derivation.	Unit-less
ρRVRH	Correlation coefficient of RV and RH (amplitude)	See Dabboor et al, 2014 for detailed description.	Unit-less
$\sigma^0_{\mathrm{RR/RL}}$	Circular polarization ratio	$\sigma^0_{\mathrm{RR/RL}} = \frac{S_0 - S_3}{S_0 + S_3}$	Power
mχe	Even bounce scattering component of m-chi decomposition (Raney, Cahill, Patterson, & Bussey, 2012)	$m\chi e = \sqrt{\frac{m(1+\sin 2\chi)}{2}}$ Where, $\sin 2\chi = \frac{-SV_3}{mSV_0}$.	Power
mχv	Volume scattering component of m-chi decomposition	$m\chi v = \sqrt{S_0(1-m)}$	Power
mχo	Odd bounce scattering component of m-chi decomposition	$m\chi o = \sqrt{\frac{mS_0(1-\sin 2\chi)}{2}}$	Power
mδd	Double bounce scattering component of m-delta decomposition	$m\delta d = \sqrt{mS_0\frac{1-\sin\delta}{2}}$ Where, $\delta = \tan^{-1}\left(\frac{S_3}{S_2}\right)$.	Power
mδv	Volume scattering component of m-delta decomposition	$m\delta v = \sqrt{S_0(1-m)}$	Power
mδs	Surface scattering component of m-delta decomposition	$m\delta s = \sqrt{mS_0\frac{1+\sin\delta}{2}}$	Power
α_s	Alpha s parameter [38]	$\alpha_s = 0.5\tan^{-1}\left(\frac{\sqrt{S_1^2+S_2^2}}{\pm S_3}\right)$	Radians
H_i	Intensity component of Shannon Entropy	$H_i = 2\log\left(\frac{\pi e \mathrm{Tr}(T_2)}{2}\right)$ Where, T_2 is the 2x2 compact polarimetric coherency matrix and, Tr is the matrix trace.	Unit-less
H_p	Polarimetric component of Shannon Entropy	$H_i = \log\left(\frac{4\lvert T_2\rvert}{\mathrm{Tr}(T_2)^2}\right)$	Unit-less
S_0, S_1, S_2, S_3	Stokes vectors (can also be expressed as S_1, S_2, S_3, S_4)		Power
$\mathrm{CPSeaIce}_{\mathrm{Depol}}$	Component of CPSeaIce Composite (Geldsetzer et al, 2015)	$\mathrm{CPSeaIce}_{\mathrm{Depol}} = \sigma^0_{\mathrm{RL}}(1-m)$	Power
$\mathrm{CPSeaIce}_{\mathrm{Delta}}$	See above.	$\mathrm{CPSeaIce}_{\mathrm{Delta}} = \sigma^0_{\mathrm{RL}}\sin\left(\frac{\delta+\pi}{4}\right)$	Power
$\mathrm{CPSeaIce}_{\mathrm{Rco}}$	See above.	$\mathrm{CPSeaIce}_{\mathrm{Rco}} = \frac{1}{2}\sigma^0_{\mathrm{RL}}\sigma^0_{\mathrm{RV/RH}}$	Power

3.8 References

1. Moen, M. A. N.; Doulgeris, A. P.; Anfinsen, S. N.; Renner, A. H. H.; Hughes, N.; Gerland, S.; Eltoft, T. Comparison of feature based segmentation of full polarimetric SAR satellite sea ice images with manually drawn ice charts. *Cryosphere* **2013**, *7*, 1693–1705, doi:10.5194/tc-7-1693-2013.

2. Souyris, J. C.; Mingot, S. Polarimetry based on one transmitting and two receiving polarizations: the pi/4 mode. *IEEE Int. Geosci. Remote Sens. Symp. 24th Can. Symp. Remote Sens.* **2002**, *1*, 629–631.

3. Souyris, J. C.; Imbo, P.; Fjørtoft, R.; Mingot, S.; Lee, J. Sen Compact polarimetry based on symmetry properties of geophysical media: The π/4 mode. *IEEE Trans. Geosci. Remote Sens.* **2005**, *43*, 634–645, doi:10.1109/TGRS.2004.842486.

4. Raney, R. K. Hybrid-polarity SAR architecture. *IEEE Trans. Geosci. Remote Sens.* **2007**, *45*, 3397–3404.

5. Raney, R. K. Dual-polarized SAR and stokes parameters. *IEEE Geosci. Remote Sens. Lett.* **2006**, *3*, 317–319, doi:10.1109/LGRS.2006.871746.

6. Charbonneau, F.; Brisco, B.; Raney, R. K.; McNairn, H.; Liu, C.; Vachon, P. W.; Shang, J.; DeAbreu, R.; Champagne, C.; Merzouki, A.; Geldsetzer, T. Compact polarimetry overview and applications assessment. *Can. J. Remote Sens.* **2010**, *36*, S298–S315, doi:10.5589/m10-062.

7. Thompson, A. A. Overview of the RADARSAT Constellation Mission. *Can. J. Remote Sens.* **2015**, *41*, 401–407.

8. Arkett, M.; Braithwaite, L.; Pestieau, P.; Carrieres, T.; Pogson, L.; Fabi, C.; Geldsetzer, T. Preparation by the Canadian Ice Service for the Operational Use of the RADARSAT Constellation Mission in Their Ice and Oil Spill Monitoring Programs. *Can. J. Remote Sens.* **2015**, *41*, 380–389, doi:10.1080/07038992.2015.1104631.

9. Livingstone, C. E.; Gray, A. L.; Singh, K. P.; Onstott, R. G.; Arsenault, L. D. Microwave Sea-Ice Signatures Near the Onset of Melt. *IEEE Trans. Geosci. Remote Sens.* **1987**, *GE-25*, 174–187, doi:10.1109/TGRS.1987.289816.

10. Nandan, V.; Geldsetzer, T.; Islam, T.; Yackel, J. J.; Gill, J. P. S.; Fuller, M. C.; Gunn, G.; Duguay, C. Ku-, X- and C-band measured and modeled microwave backscatter from a highly saline snow cover on first-year sea ice. *Remote Sens. Environ.* **2016**, *187*, 62–75, doi:10.1016/j.rse.2016.10.004.

11. Richards, J. *Remote Sensing with Imaging Radar*. **2009**. ISBN 9783642020193.

12. Perovich, D. K.; Grenfell, T. C.; Light, B.; Hobbs, P. V. Seasonal evolution of the albedo of multiyear Arctic sea ice. *J. Geophys. Res.* **2002**, *107*, 8044, doi:10.1029/2000JC000438.

13. Perovich, D. K.; Polashenski, C. Albedo evolution of seasonal Arctic sea ice. *Geophys. Res. Lett.* **2012**, *39*, 1–6, doi:10.1029/2012GL051432.

14. Pućko, M.; Stern, G. A.; Macdonald, R. W.; Jantunen, L. M.; Bidleman, T. F.; Wong, F.; Barber, D. G.; Rysgaard, S. The delivery of organic contaminants to the Arctic food web: Why sea ice matters. *Sci. Total Environ.* **2015**, *506–507*, 444–452, doi:10.1016/j.scitotenv.2014.11.040.

15. Yackel, J. J.; Barber, D. G.; Hanesiak, J. M. Melt ponds on sea ice in the Canadian Archipelago: 2. On the use of RADARSAT-1 synthetic aperture radar for geophysical inversion. *J. Geophys. Res.* **2000**, *105*, 22061–22070, doi:10.1029/2000JC900075.

16. Barber, D. G.; Yackel, J. J. The physical, radiative and microwave scattering characteristics of melt ponds on Arctic landfast sea ice. *Int. J. Remote Sens.* **1999**, *20*, 2069–2090, doi:10.1080/014311699212353.

17. Scharien, R. K.; Yackel, J. J.; Barber, D. G.; Asplin, M.; Gupta, M.; Isleifson, D. Geophysical controls on C band polarimetric backscatter from melt pond covered Arctic first-year sea ice: Assessment using high-resolution scatterometry. *J. Geophys. Res.* **2012**, *117*, doi:10.1029/2011JC007353.

18. Fetterer, F. M.; Untersteiner, N. Observations of melt ponds on Arctic sea ice. *J. Geophys. Res.* **1998**, *103*, 24821–24835.

19. Hanesiak, J. M.; Barber, D. G.; De Abreu, R. a.; Yackel, J. J. Local and regional albedo observations of arctic first-year sea ice during melt ponding. *J. Geophys. Res.* **2001**, *106*,

1005–1016, doi:10.1029/1999JC000068.

20. Webster, M. A.; Rigor, I. G.; Perovich, D. K.; Richeter-Menge, J. A.; Polashenski, C. M.; Light, B. Seasonal evolution of melt ponds on Arctic sea ice. *J. Geophys. Res.* **2015**, *120*, 1–15, doi:10.1002/2015JC011030.

21. Liu, J.; Song, M.; Horton, R. M.; Hu, Y. Revisiting the potential of melt pond fraction as a predictor for the seasonal Arctic sea ice extent minimum. *Environ. Res. Lett.* **2015**, *10*, 1–6, doi:10.1088/1748-9326/10/5/054017.

22. Schröder, D.; Feltham, D. L.; Flocco, D.; Tsamados, M. September Arctic sea-ice minimum predicted by spring melt-pond fraction. *Nat. Clim. Chang.* **2014**, *4*, 353–357, doi:10.1038/nclimate2203.

23. Timco, G. W.; Weeks, W. F. A review of the engineering properties of sea ice. *Cold Reg. Sci. Technol.* **2010**, *60*, 107–129, doi:10.1016/j.coldregions.2009.10.003.

24. Arctic Council Arctic Marine Shipping Assessment 2009 Report. *Arctic* **2009**, 39–55.

25. Dabboor, M.; Geldsetzer, T. Towards sea ice classification using simulated RADARSAT Constellation Mission compact polarimetric SAR imagery. *Remote Sens. Environ.* **2014**, *140*, 189–195, doi:10.1016/j.rse.2013.08.035.

26. Geldsetzer, T.; Arkett, M.; Zagon, T.; Charbonneau, F.; Yackel, J. J.; Scharien, R. K. All-Season Compact-Polarimetry C-band SAR Observations of Sea Ice. *Can. J. Remote Sens.* **2015**, *41*, 485–504, doi:10.1080/07038992.2015.1120661.

27. Canadian Ice Service. *Sea Ice Climatic Atlas: Northern Canadian Water 1981-2010*; Ottawa, **2011**.

28. Clausi, D. A. An analysis of co-occurrence texture statistics as a function of grey level quantization. *Can. J. Remote Sens.* **2002**, *28*, 45–62, doi:10.5589/m02-004.

29. Liu, H.; Guo, H.; Zhang, L. SVM-Based Sea Ice Classification Using Textural Features and Concentration From RADARSAT-2 Dual-Pol ScanSAR Data. *IEEE J. Sel. Top. Appl. Earth Obs. Remote Sens.* **2015**, *8*, 1601–1613, doi:10.1109/JSTARS.2014.2365215.

30. Lardeux, C.; Frison, P. L.; Tison, C.; Souyris, J. C.; Stoll, B.; Fruneau, B.; Rudant, J. P.

Support vector machine for multifrequency SAR polarimetric data classification. *IEEE Trans. Geosci. Remote Sens.* **2009**, *47*, 4143–4152, doi:10.1109/TGRS.2009.2023908.

31. Brisco, B.; Li, K.; Tedford, B.; Charbonneau, F.; Yun, S.; Murnaghan, K. Compact polarimetry assessment for rice and wetland mapping. *Int. J. Remote Sens.* **2013**, *34*, 1949–1964, doi:10.1080/01431161.2012.730156.

32. Freeman, A.; Durden, S. L. A three-component scattering model for polarimetric SAR data. *IEEE Trans. Geosci. Remote Sens.* **1998**, *36*, 963–973, doi:10.1109/36.673687.

33. Casey, J. A.; Howell, S. E. L.; Tivy, A.; Haas, C. Separability of sea ice types from wide swath C- and L-band synthetic aperture radar imagery acquired during the melt season. *Remote Sens. Environ.* **2016**, *174*, 314–328, doi:10.1016/j.rse.2015.12.021.

34. Barber, D. G.; Yackel, J. J.; Hanesiak, J. M. Sea Ice , RADARSAT-1 and Arctic Climate Processes : A Review and Update. *Can. J. Remote Sens.* **2001**, *27*, 51–61, doi:10.1080/07038992.2001.10854919.

35. Scharien, R. K.; Hochheim, K.; Landy, J.; Barber, D. G. First-year sea ice melt pond fraction estimation from dual-polarisation C-band SAR – Part 2: Scaling in situ to Radarsat-2. *Cryosph.* **2014**, *8*, 2163–2176, doi:10.5194/tc-8-2163-2014.

36. Eicken, H.; Krouse, H. R.; Kadko, D.; Perovich, D. K. Tracer studies of pathways and rates of meltwater transport through Arctic summer sea ice. **2002**, *107*, 1–20, doi:10.1029/2000JC000583.

37. Raney, R. K.; Cahill, J. T. S.; Patterson, G. W.; Bussey, D. B. J. The m-chi decomposition of hybrid dual-polarimetric radar data with application to lunar craters. *J. Geophys. Res.* **2012**, *117*, doi:10.1109/IGARSS.2012.6352465.

38. Cloude, S. R.; Goodenough, D. G.; Chen, H. Compact decomposition theory. *IEEE Geosci. Remote Sens. Lett.* **2012**, *9*, 28–32, doi:10.1109/LGRS.2011.2158983.

Chapter 4 Summary and Conclusions

There exist gaps in understanding and parameterizing Arctic sea ice and related processes during the melt season, due to the complex and highly variable melt conditions combined with a lack of reliable observations during this time. The Arctic sea ice cover is undergoing rapid decline, with most of loss in extent observed in September, corresponding to the minimum sea ice extent [1,2]. Representation of geophysical parameters such as melt pond fraction in climate models remains poor, and in order to inform mitigation and adaption strategies associated with climate change, it is necessary to accurately forecast sea ice conditions on short and long-term scales [3,4].

The research presented in this thesis is motivated by improving melt pond fraction parametrization in sea ice forecast models and isolating major ice types using SAR during the melt season. The Arctic is a vast region which has been undergoing rapid climate change driven changes that will likely have an effect on the climate of mid-latitudes [5]. Furthermore, the decline in sea ice will likely lead to an increase in human activity, putting pressure on government agencies to provide accurate and timely information on the location of ice hazards such as MYI. This final chapter summarizes key findings, outlines potential for future research and acknowledges co-author contributions to the manuscripts.

4.1 Summary of Key Findings

Chapter 2 focused on testing the following hypothesis: melt pond fraction can be predicted from winter sea ice thickness and surface roughness. The hypothesis was tested by quantitatively linking winter sea ice thickness and surface roughness to spring melt pond fraction on landfast Arctic sea ice. High resolution point measurements acquired using an EM induction instrument (thickness) and a 2D laser scanner (surface roughness) during winter, were compared to high resolution GeoEye-1 optical imagery of melt pond covered sea ice during *advanced melt*. The results support our hypothesis and demonstrate that winter sea ice thickness has a strong negative association with FYI f_p ($r_s = -0.85$) and MYI f_p ($r_s = -0.56$). Surface roughness is correlated with f_p for FYI ($r_s = -0.52$) but not MYI. These quantitative relationships lend support to previously qualitative work on linking sea ice surface roughness and f_p. Importantly, the hybrid aggregation approach shows consistently improved correlations which suggests that aggregation features that take into account both the morphology of the ice and the footprints of the sensors used to collect the measurements are ideal. The application of a moving average to the surface roughness data improved associations with f_p for both FYI and MYI. This can be explained by the reduction of uncertainties at the measurement scale, likely associated with snow roughness and redistribution features, however *in situ* measurements are necessary for confirmation.

In Chapter 3 the following hypothesis was tested: compact polarimetric SAR enables discrimination of major sea ice types during advanced melting conditions. Using simulated RCM parameters and GLCM texture features from two winter and two advanced melt scenes were used to assess ice type separability during winter and *advanced melt*. A two-sample Kolmogorov-Smirnov statistical test was used to quantify separability, and RCM parameters with the highest separability were used to generate GLCM texture features for subsequent SVM image classification. Through classification of two *winter* scenes it is demonstrated that RCM parameters provide good discriminability between major ice types during winter conditions, with overall classification accuracies of 81.21% and 96.93%. The classification of the advanced melt scene acquired at a steep incidence angle showed good overall classification accuracy of 77.06%, compared to the advanced melt scene collected at a shallow incidence angle (48.54%). The addition of GLCM texture features to the classifications lead to improvement in overall classification accuracies for both winter and advanced melt scenes by increasing between class separability and reducing clusters of misclassified FYI and MYI pixels. Most importantly, with the addition of GLCM texture features, classification accuracy of the steep incidence angle advanced melt scene improvement by 8.85%, with the Kappa coefficient increasing from 0.52 to 0.71. The ability to discriminate between FYI and MYI can be explained by the sensitivity of steep incidence angle C-band SAR to wind roughened melt ponds on FYI which manifests as high Bragg scattering. During the *advanced melt* period, FYI is dominated by large expanses of interconnected melt ponds, whereas, melt ponds on MYI are less interconnected and are constrained within the deeper channels of the ice. The results of the SVM supervised classifications and available observations support our hypothesis. The results of this work contribute new knowledge on the ability of RCM parameters to distinguish between major ice types during the *advanced melt* period, and corroborated the results from previous studies demonstrating the utility of RCM parameters for winter ice type separability.

4.2 Opportunities for Future Work

The characterization sea ice surface roughness at both the micro- and macro-scales and their respective influences on SAR backscatter, remains an active area of research. Generally, it is thought that micro-scale surface roughness, on the scale of the wavelength of the SAR system, is the principal scale governing backscatter. However, sea ice surfaces often exceed the micro-scale criteria, thus macro-scale roughness has a strong effect on backscatter as well. Macro-scale surface roughness is an important geophysical parameter that affects melt pond distribution. Using terrestrial LiDAR it has been shown that topographic relief of snow dunes prior to the onset of melt determine the locations of initial melt pond formation. Whereas, macro-scale surface roughness controls the aerial extent of melt ponds [6]. The results of Chapter 2 showed that surface roughness as measured by a 2D laser scanner does not exhibit an association with MYI f_p. However, the application of a large moving average (~2400 m) on the roughness data significantly improved correlations with both FYI and MYI f_p. Although, smoothing of data warrants caution due to the risk of introduction of spatial autocorrelation, this result is of interest for remote sensing and large scale climate modelling applications. From a signal processing perspective, it is possible that the smoothing of the surface roughness data reduced footprint scale uncertainties associated with snow roughness, with the signal of topographic sea ice roughness remaining [7]. Collocated measurements of snow and sea ice roughness would be useful for determining the effect of the snow roughness component on the total surface roughness. Furthermore, more work is required for defining roughness at varied horizontal and vertical length scales, perhaps through the use of Lidar. *In situ* LiDAR measurements could be used to better understand the errors associated with estimates of surface roughness from airborne and satellite laser altimeter or laser scanner instruments. Improved understanding and quantification of roughness, particularly at the macro-scale, would also benefit the SAR community.

The EM sensor which was used to measure sea ice thickness, does not penetrate through the snow cover, thus it measures snow plus ice thickness [8]. In the literature, it is assumed that snow depth in the Victoria Strait region is under 30 cm, however this assumption is derived from a single location near Cambridge Bay, where snow depth measurements are collected on FYI [9]. From an *in situ* snow depth dataset near Eureka, Nunavut, it can be seen that MYI snow depth can exceed one metre. A collocated dataset of EM sea ice thickness, *in situ* snow depth and 2D laser scanner would allow for the isolation of sea ice thickness and comparison with spring f_p. In general, little information exists on snow depth distribution in the CAA, and work is required to for understanding snow depth variability for major ice types. Chapter 2 was concerned with a snapshot of melt pond distribution on a particular day in a relatively small geographic area. Expanding the analyses to larger spatial and temporal scales relevant for climate models is necessary. Open source high resolution optical data from Sentinel-2, for estimations of f_p, as well as sea ice thickness estimates from spaceborne CryoSat-2, and airborne IceBridge missions can be used to advance the work.

The research presented in Chapter 3 contributes to the body of work on ice type separability using C-band CP SAR during the *advanced melt* period. However, further investigation is required for understanding C-band SAR sensitivity to variable surface conditions within the *advanced melt* period. Access to validation data acquired at the time of SAR image acquisition, such as high resolution optical imagery, wind speed, wind direction and temperature, is often limited but necessary for improving our understanding of SAR scattering mechanisms. To increase the scope of this project, a time series of Sentinel-1 imagery can be used to observe the backscatter intensity inversion between FYI and MYI, in a variety of Arctic locations. When not obscured by cloud cover, freely available Sentinel-2 and operation IceBridge optical data can be used to aid interpretation of scattering mechanisms. A conformation of the observed utility of steep incidence angle simulated RCM parameters for ice type discrimination using a larger dataset is also required. A comprehensive assessment of optimal GLCM texture parameters for major ice type separability during various thermodynamic stages of sea ice evolution at varied incidence angles is necessary. Finally, the effects of GLCM parameters such as window size, quantizer type and quantization levels on ice type separability should also be investigated.

4.3 Author Contributions

The research conducted as part of this thesis was a collaborative effort with co-authors contributing data, ideas and editorial comments. Randy Scharien conceived both studies, provided the object aggregation features used in Chapter 2, provided expert interpretation and contributed extensive feedback on all parts of the thesis and resulting manuscripts. Christian Haas provided sea ice thickness and surface roughness data, as well assisted with interpretation Chapter 2 results. Stephen Howell, provided RADARSAT-2 and GeoEye-1 data, and contributed editorial comments for both Chapter 2 and Chapter 3. Finally, Torsten Geldsetzer provided the simulated RCM parameters along with guidance on interpretation of results and editorial comments for Chapter 3.

4.4 References

1. Stroeve, J. C.; Kattsov, V.; Barrett, A. P.; Serreze, M.; Pavlova, T.; Holland, M. M.; Meier, W. N. Trends in Arctic sea ice extent from CMIP5, CMIP3 and observations. *Geophys. Res. Lett.* **2012**, *39*, 1–7, doi:10.1029/2012GL052676.

2. Serezze, M.; Holland, M. M.; Stroeve, J. C. Perspectives on the Arctic's Shrinking Sea-Ice Cover. *Science.* **2007**, *315*, 1533–1536, doi:10.1016/S0169-1317(03)00213-8.

3. Schröder, D.; Feltham, D. L.; Flocco, D.; Tsamados, M. September Arctic sea-ice minimum predicted by spring melt-pond fraction. *Nat. Clim. Chang.* **2014**, *4*, 353–357, doi:10.1038/nclimate2203.

4. Swart, N. C.; Fyfe, J. C.; Hawkins, E.; Kay, J. E.; Jahn, A. Influence of internal variability on Arctic sea-ice trends. *Nat. Clim. Chang.* **2015**, *5*, 86–89, doi:10.1038/nclimate2483.

5. Jennifer, F.; Vavrus, S. Evidence linking Arctic amplification to extreme weather in mid-latitudes. *Geophys. Res. Lett.* **2012**, *39*, doi:10.1002/grl.50880.

6. Polashenski, C.; Perovich, D. K.; Courville, Z. The mechanisms of sea ice melt pond formation and evolution. *J. Geophys. Res.* **2012**, *117*, 1–23, doi:10.1029/2011JC007231.

7. King, J.; Howell, S. E. L.; Derksen, C.; Rutter, N.; Toose, P.; Beckers, J. F.; Haas, C.; Kurtz, N.; Richeter-Menge, J. A. Evaluation of Operation IceBridge quick-look snow depth estimates on sea ice. *Geophys. Res. Lett.* **2015**, *42*, 9302–9310,

doi:10.1002/2015GL066389.

8. Haas, C.; Lobach, J.; Hendricks, S.; Rabenstein, L.; Pfaffling, A. Helicopter-borne measurements of sea ice thickness, using a small and lightweigh, digital EM system. *J. Appl. Geophys.* **2009**, *67*, 234–241, doi:10.1016/j.jappgeo.2008.05.005.

9. Howell, S. E. L.; Laliberté, F.; Kwok, R.; Derksen, C.; King, J. Landfast ice thickness in the Canadian Arctic Archipelago from Observations and Models. *Cryosph. Discuss.* **2016**, 1–39, doi:10.5194/tc-2016-71.